Leipzig University
Faculty of Physics and Earth Sciences
Institute for Meteorology

Leibniz Institute for Tropospheric Research

Characterization of the annual cycle of aerosol and clouds over Mindelo (Cabo Verde) by means of continuous multiwavelength lidar observations

Master thesis

submitted by:

Henriette Gebauer
matriculation number: 3755867

Supervisors:
Prof. Dr. Andreas Macke
Dr. habil. Matthias Tesche

Contact person:
Dr. Holger Baars

Date of submission: 12 July 2024

Contents

List of Figures

List of Tables

Chapter 1

Introduction

Atmospheric aerosol is important in atmospheric research as aerosol particles affect the Earth's climate in a crucial way due to their radiative effects and their interaction with clouds. Aerosol particles can scatter, absorb or reflect solar and terrestrial radiation (direct radiative effect; McCormick & Ludwig, 1967; Liu et al., 2014), influence the large-scale motions by heating due to the absorption of radiation (semi-direct radiative effect; Liu et al., 2014) or modify the cloud formation as cloud condensation nuclei (CCN) or ice nucleating particles (INP, indirect radiative effect; Liu et al., 2014).

In this context, mineral dust plays a key role as it is the most abundant component of atmospheric aerosol and dust particles are known to be effective INPs (Choobari et al., 2014). While the radiative effects are well known for pure aerosol types, describing the radiative effects of aerosol mixtures is challenging and still needs great efforts in research (Tegen et al., 1997; Satheesh & Krishna Moorthy, 2005).

For this purpose, a proper aerosol classification is fundamental. Therefore, the aerosol lidar is the most appropriate instrument to perform vertically-resolved measurements of aerosol. Using multiple wavelengths as well as the Raman and polarization techniques as it is valid for the Polly^{XT} devices (Althausen et al., 2009; Engelmann et al., 2016), offers best capabilities for the characterization of the optical properties of aerosol particles. Furthermore, with POLIPHON (Tesche et al., 2009; Ansmann et al., 2019) and DeLiAn (Floutsi et al., 2023), well established methods and data bases for the separation and classification of different aerosol types are available. Several automatized typing algorithms like the lidar target classification (Baars et al., 2017), the Neural network Aerosol Typing Algorithm based on Lidar data (NATALI; Nicolae et al., 2018) and the European Aerosol Research Lidar Network (EARLINET) Mahalanobis distance-based typing algorithm (EMD; Papagiannopoulos et al., 2018) contribute to a better understanding of the global occurrence of aerosol types. To cover a wide spatial range with observations, several Polly^{XT} lidars are operated in the network of automated Raman-polarization lidars (Polly^{NET}; Baars et al., 2016) monitoring the atmosphere all around the world. Due to the importance of mineral dust and the Saharan desert as the largest dust source worldwide, measurement sites in that region are of particular interest.

Therefore, the Cabo Verde islands, located around 640 km west of the coast of West Africa, have established themselves as an appropriate location to study Saharan dust as well as mixtures with other aerosol types, e.g., marine aerosol and biomass burning aerosol at the beginning of their transport towards South and Central America (Tesche et al., 2011a,b; Tesche, 2011). Even volcanic sulfate could be observed over Cabo Verde in September 2021, originating from the eruption of Cumbre Vieja at La Palma, Canary Islands, Spain (Gebauer et al., 2024). Although it is already known from previous campaigns like the Saharan Mineral dust experiment 2 (SAMUM–2; Ansmann et al., 2011a; Tesche et al., 2011a,b) that significant differences in

the aerosol conditions over Cabo Verde occur between boreal summer and winter, the European seasons (DJF, MAM, JJA and SON) do not represent the seasons at Cabo Verde in a satisfying way. As learnt from SAMUM–2, the seasons at Cabo Verde are better characterized by a dust season (mainly pure Saharan dust) and a mixing season (often mixtures of Saharan dust with biomass burning aerosol). Thus, one main focus of this thesis is to define more precisely the concrete time frame which covers the dust season and the mixing season. Furthermore, this thesis aims to characterize the aerosol occurrence over Cabo Verde in terms of geometrical extension and optical properties for these two main seasons. Please note that in the following, the terms northern hemispheric seasons refer to the European seasons while the terms dust season and mixing season denote the main seasons relevant for Cabo Verde.

For the characterization of the seasons at Cabo Verde in terms of aerosol conditions, aerosol lidar measurements were analyzed. More than 10 years after SAMUM–2, the multiwavelength-Raman-polarization lidar system Polly^{XT} was installed at Mindelo, Cabo Verde, in June 2021 within the framework of the Joint Aeolus-Tropical Atlantic campaign (JATAC; Fehr et al., 2023; Marinou et al., 2023) and has been permanently operated since then. Thus, it is the first time that the complete annual cycle of aerosol over Cabo Verde was observed by continuous aerosol lidar measurements and analyzed based on automatically retrieved vertical profiles of aerosol optical properties using the Polly^{NET} processing chain (Baars et al., 2016; Yin & Baars, 2021). For this thesis, a two-year data set of lidar measurements was considered, covering the period from July 2021 to August 2023. For this period, one lidar profile per week was selected to be included in the analysis of the aerosol conditions present on the nights from Friday to Saturday, which coincides with the direct overpass of the Aeolus satellite over Mindelo (Fri around 19:30 UTC, i.e. 18:30 LT). Concentrating on these nights offers the opportunity to use the obtained data set for the ongoing calibration and validation of the Aeolus satellite.

The frequent occurrence of clouds, especially at altitudes of less than 2 km, has turned out to be a crucial issue for the measurement site at Mindelo. Thus, in this thesis, a central focus was furthermore put on the improvement of the cloud screening implemented in the Polly^{NET} processing chain. In addition, a general overview of the presence of clouds at Mindelo is given.

This thesis is structured as follows: In Chap. 2, the basic information about atmospheric aerosol and the lidar technique used for aerosol detection and classification is summarized with a special focus on the aerosol types occurring at Mindelo, i.e., mineral dust, marine aerosol, biomass burning aerosol and volcanic aerosol. In addition, an overview of previous campaigns studying Saharan dust and aerosol mixtures in the region of Cabo Verde is given. In Chap. 3, the methods used in this study are introduced and a short overview of the JATAC campaign is given, because Polly^{XT} was deployed at Mindelo in the framework of this campaign. In the same chapter, several case studies are used to illustrate the methods applied in this thesis. Afterwards, the results are presented in Chap. 4, including lidar-based statistics concerning the cloud occurrence over Mindelo, a case study analysis of aerosol lidar measurements contrasting a typical case from the dust regime with a measurement obtained during the mixing regime and, finally, a general analysis of the annual cycle of aerosol over Mindelo out of which a concretization of the seasons at Mindelo is derived. At the end, conclusions and an outlook are given in Chap. 5.

Chapter 2

Literature review

2.1 Importance and general climate effects of different aerosol types

2.1.1 Introduction into aerosol microphysical and optical properties

Aerosol particles are solid or liquid particles embedded in the atmosphere and originate from natural or anthropogenic sources. Atmospheric aerosol occurs globally but its composition exhibits a large regional and temporal variation (Tegen et al., 1997). According to John (2011) and the Whitby model (Whitby, 1978), aerosol particles can be categorized in three different size modes – the nuclei mode, the accumulation mode and the coarse mode. Generally, the particle diameter d ranges from a few nanometers to 100 µm. In particular, the nuclei mode includes particles with diameters from 0.005–0.1 µm. The accumulation mode is comprised of particles with diameters between 0.1 and 2 µm. The nuclei and the accumulation mode are combined to a fine mode, which denotes particles with $d < 2$ µm. The remaining size orders, i.e., $d > 2$ µm, are summarized as the coarse mode. Besides the different size ranges of which the size modes consist, they differ concerning the formation processes of the aerosol particles.

In addition to particle size, aerosol particles can be described by fundamental aerosol optical properties, which are the aerosol optical depth (AOD), the Ångström exponent and the single scattering albedo (SSA) (Liu et al., 2014). The AOD is the vertically integrated extinction, which is the sum of scattering and absorption. The Ångström exponent describes the wavelength dependence of the AOD, indicating the particle size (a detailed description is to be found in Sect. 2.3.1). The SSA is the ratio of the scattering to the extinction properties and quantifies which process is dominating—scattering or absorption. It is 1.0 for non-absorbing and zero for completely absorbing aerosol particles (Satheesh & Krishna Moorthy, 2005).

Aerosol particles play an important role in meteorological and global climate processes, as they modulate the Earth's radiative budget due to their direct and indirect radiative effects. The direct radiative effect arises from scattering and absorption of solar and terrestrial radiation, which causes cooling or warming, respectively (McCormick & Ludwig, 1967; Liu et al., 2014). In total, the global aerosol leads to cooling (Liu et al., 2014), but the radiative effect is different for different aerosol types and depends on the SSA of the respective particles (Satheesh & Krishna Moorthy, 2005). Furthermore, the semi-direct effect describes the effect of heating due to absorbing aerosol, which drives large-scale motion and reduces the liquid water. Both processes have an impact on the properties of clouds and their radiative effects (Liu et al., 2014). Instead, the indirect radiative effect (Liu et al., 2014) is characterized by aerosol particles acting as CCN or INP. Thus, they affect cloud formation and the properties of the developing cloud, which, in turn, has direct radiative effects. Two kinds of processes have to be taken into account.

The first indirect effect (Twomy effect) implies that the availability of more CCN (compared to a smaller number of CCN at the same amount of precipitable water) lead to the formation of more and smaller droplets, which increases the cloud albedo. The second indirect effect means a longer cloud lifetime due to the smaller droplets. Not all aerosol particles can serve as CCN (or INP) as they have to exceed a critical size (radius $> 1\,\mu m$) and need to be hygroscopic (Satheesh & Krishna Moorthy, 2005). The following sections summarize the direct radiative effects and the importance as CCN and INP of selected aerosol types, which play a role in the Cabo Verde region as introduced in Chap. 1.

2.1.2 Mineral dust

Mineral dust is globally of particular importance as it is the most abundant atmospheric aerosol component with regard to dry mass and accounts for more than half of the total aerosol burden (Choobari et al., 2014). Mineral dust causes higher AOD values than anthropogenic pollution. It appears more frequently and in larger and more persistent plumes (Prospero et al., 2002). Besides its impact on the climate, mineral dust particles are crucial for marine biological processes, whereby they influence the carbon cycle, as well as for paleoclimate studies (Prospero et al., 2002). Due to their non-spherical shape, they present specific challenges for climate models (Di Biagio et al., 2020).

The global properties of mineral dust and its direct radiative effect are still a matter of debate. The absorption of longwave radiation, which causes a warming effect during night and in the lower atmosphere, and the backscattering and absorption of shortwave radiation have already been known for a while. The dependence of these radiative effects on the particle size distribution and the consideration of giant dust particles are both relatively new topics and they led to changes in the established consensus. Novel findings have shown that for small dust particles, the scattering of shortwave radiation and, thus, the cooling effect dominates. Large particles absorbing both longwave and shortwave radiation are more absorptive than smaller particles and cause a warming effect. However, the net cooling or warming effect is around zero (Choobari et al., 2014; Di Biagio et al., 2020). Considering the size distribution, the regional dependence of the direct radiative effect has to be taken into account as there are regional differences in the size distribution of mineral dust Di Biagio et al. (2020). This regional perspective includes the dependence on the surface albedo. Dust plumes occurring over surface types with a high albedo, e.g., land surfaces, deserts or clouds have a warming effect as more radiation is reflected by the ground and, in turn, absorbed by the dust particles. In contrast, a cooling effect is observed over the ocean (Choobari et al., 2014).

Concerning the indirect radiative effect, mineral dust particles are important as they serve as efficient INPs and can increase the mean effective particle size in cirrus clouds. Depending on the size, some dust particles can even act as CCN. Small fresh dust particles are much more hygroscopic than large ones, but aged dust is also hygroscopic (Choobari et al., 2014). A further effect on clouds can be seen in the preferred absorption of radiation by dust particles which may strengthen the formation of convective clouds leading to an increase in precipitation (Choobari et al., 2014).

2.1.3 Biomass burning aerosol (smoke)

Biomass burning aerosol or smoke can originate from natural or anthropogenic fires. Their exact chemical composition depends on the fuel and the burning process (Janhäll et al., 2010). Typical components of biomass burning aerosol are nitrate, ammonium, sulfur, organic components and black carbon (Adler et al., 2011). 40 % of the global black carbon originates from biomass burning aerosol (Adler et al., 2011). The size distribution typically observed for this aerosol type

is dominated by the accumulation mode with a mode diameter of 100–150 nm (Janhäll et al., 2010) and, thus, represents the smallest section of the fine mode (Alonso-Blanco et al., 2014). However, a coarse mode and sometimes a nucleation mode can be observed as well (Janhäll et al., 2010). The latter occurs often close to the emission source and has only little influence on the aerosol optical properties and the CCN activity (Janhäll et al., 2010). Depending on the size mode of the particles, their chemical composition varies. Coarse mode particles usually contain dust, ash and carbon aggregates, while particles in the accumulation mode are mainly composed by organic matter and a low amount of soot and inorganic components (Janhäll et al., 2010). Due to aging of the smoke particles, the aerosol optical and chemical properties change. Thus, the absorption properties decrease, while the particle size and organic mass concentration increase (Adler et al., 2011).

Biomass burning aerosol absorbs shortwave radiation to a large extent and absorbs longwave radiation completely (Satheesh & Krishna Moorthy, 2005). In contrast, there is only very little scattering for these particles (Kaufman & Fraser, 1997). Thus, smoke has a strong warming effect (Alonso-Blanco et al., 2014). In addition, smoke particles are effective CCN (Kaufman & Fraser, 1997). Besides its climatological effects, biomass burning aerosol is significantly important for human health as the particles, which often bear toxic and carcinogenic substances, are very small and, thus, can efficiently infiltrate into the alveolus (Adler et al., 2011). This aspect is particularly important as wildfires can cause pollution events with PM_{10} concentrations up to $90\,\mu g\,m^{-3}$ even in rural areas (Alonso-Blanco et al., 2014). For comparison, the European daily mean threshold for the PM_{10} concentration is $50\,\mu g\,m^{-3}$, which should not be exceeded on more than 35 days per year (Alonso-Blanco et al., 2014).

2.1.4 Marine aerosol

Marine aerosol is an important aerosol type, too, as it has the highest natural aerosol production rate (Satheesh & Krishna Moorthy, 2005). Marine aerosol comprises sea salt particles and oceanic sulfur aerosols. The latter are fine particles, which are produced over the ocean and grow to sizes with radii larger than 0.1 µm (Satheesh & Krishna Moorthy, 2005). The direct radiative effect of marine aerosol is characterized by no absorption of shortwave radiation and only little absorption of longwave radiation. Thus, the radiative effect is overall negative. The radiative forcing as well as the aerosol mass concentration and the chemical composition also depend on the wind speed. An increase in the wind speed leads to an increase in the SSA, which decreases the forcing at the surface, and to an increase in the AOD, which increases the forcing at the surface (Satheesh & Krishna Moorthy, 2005). Both effects compensate each other. At the top of the atmosphere, an increase in both, the SSA and the AOD, results in an increase of the negative radiative forcing (Satheesh & Krishna Moorthy, 2005). However, the radiative forcing at the top of the atmosphere can also decrease and even become positive, when the cloud cover increases (Satheesh & Krishna Moorthy, 2005). Concerning the indirect radiative effect, it is worth to mention that marine aerosol particles are hygroscopic and, thus, act as CCN (Satheesh & Krishna Moorthy, 2005).

2.1.5 Volcanic ash and sulfate

Volcanic aerosol, which includes ash particles as well as sulfate, has large impact on the climate especially in the stratosphere (Robock, 2000). Volcanic ash belongs to the coarse mode (Ansmann et al., 2011b) and is, thus, likely to fall out close to the emission source (Sassen et al., 2007) but, depending on the size distribution and the meteorological conditions, can be transported over distances of more than 100 km as well (Langmann, 2013). Volcanic ash shows scattering and a stronger absorption compared to mineral dust and mostly leads to a reduction of the

surface albedo, of course depending on the color and chemical composition of the ash particles (Langmann, 2013). Volcanic ash particles are also good INPs (Seifert et al., 2011).

In contrast to ash, volcanic sulfate particles belong to the fine mode (Ansmann et al., 2011b). They are either formed from sulfur dioxide (SO_2) (Robock, 2000; Martin et al., 2014; Pattantyus et al., 2018), which has a short lifetime of 1–3 days in the troposphere (Navas-Guzmán et al., 2013), or can be emitted directly during volcanic eruptions (Martin et al., 2014). Compared to SO_2, the sulfate aerosol has a longer lifetime of 1–3 weeks in the troposphere (Pappalardo et al., 2004) and even several years in the stratosphere (Jäger, 2005; Deshler, 2008). In the shortwave range, its SSA is up to unity, which means pure or at least strong backscattering. Thus, the planetary albedo increases and the incoming radiation decreases causing a cooling effect at the surface (Tegen et al., 1997; Robock, 2000; Satheesh & Krishna Moorthy, 2005). The scattering efficiency increases even more with higher relative humidity and hygroscopic growth of the sulfate particles (Miffre et al., 2012). Concerning longwave radiation, they are partly absorbing and favor stratospheric heating (Robock, 2000). As they also act as CCN, they may suppress the formation of ice particles (Tegen et al., 1997; Satheesh & Krishna Moorthy, 2005; Ansmann et al., 2011b).

2.1.6 Aerosol mixtures

As seen in the previous sections, the different aerosol types show quite different behaviors concerning their direct and indirect radiative effects and their interaction with clouds. Therefore, it is all the more important to investigate the combination of different aerosol types as the absorption and scattering properties of aerosol in mixtures are different compared with pure aerosol types (Tegen et al., 1997; Satheesh & Krishna Moorthy, 2005). Different compositions of different aerosol types lead to changes in the size distribution, i.e., coagulation increases the average aerosol size, as well as in the particle shape, in the water solubility, in the hygroscopicity and in the refractive index. Thus, the chemical activity of the aerosol mixtures, their residence time in the atmosphere and their capability to act as CCN or INP are affected (Lesins et al., 2002). For instance, coating dust particles with sulfate increases their hygroscopicity and leads to chemical reactions. Also, if sulfate aerosol is absorbed by mineral dust particles, the number of sulfate particles, i.e., the number concentration of CCN and, thus, the cloud droplet number concentration are reduced (Tegen et al., 1997).

As it is difficult to describe the real mixing state of the aerosol mixture, two idealized assumptions exist. In an external mixture, the different aerosol components are physically separated, while an internal mixture is a homogeneous material of all contributing components (Lesins et al., 2002). Typically, the aerosol is internally mixed. Such mixtures might develop at the emission source or due to coagulatiuon. However, it is difficult to represent internal mixtures in global climate models so that aerosol mixtures are often parameterized as external mixtures (Lesins et al., 2002).

Investigating the vertically-resolved optical properties and global distribution of aerosol particles and especially aerosol mixtures in the atmosphere is of crucial importance in understanding aerosol-climate interactions. For this purpose, an aerosol lidar like the multiwavelength-Raman polarization lidar Polly^{XT} is the ideal device for profiling the atmospheric aerosol conditions in high resolution. In the next sections, the basic lidar principle in general and the features of Polly^{XT} in particular will be described.

2.2 Polly^{XT}—Lidar theory

2.2.1 General lidar principle

The terms Polly and Polly^{XT} denote a series of lidars built at the TROPOS–Leibniz-Institute for Tropospheric Research, Leipzig, Germany (Althausen et al., 2009; Engelmann et al., 2016). Generally, a lidar is an active remote sensing device emitting laser pulses at one or more wavelengths. In case of Polly^{XT}, typically a Nd:YAG laser is used to produce laser pulses at 1064 nm with a repetition rate of 20 Hz. Due to frequency doubling, light at 355 and 532 nm is generated (Althausen et al., 2009). The laser pulses are emitted almost vertically into the atmosphere. When they hit a target above the lidar (e.g., a measurement volume consisting of air molecules, aerosol particles and/or cloud particles), they are partly backscattered by this measurement volume. Receiving optics and photomultiplyer tubes or photodiodes within the lidar are used to detect the backscattered light (Wandinger, 2005). In case of Polly^{XT}, the signals are received with a vertical and temporal resolution of 7.5 m and 30 s, respectively (Engelmann et al., 2016). Attenuation of the emitted and the backscattered light on its way through the atmosphere has to be taken into account, as well as the incomplete overlap between the emitted laser beam and the field of view of the receiving telescope in low altitudes above the lidar. The latter has the consequence that no signal is received from these altitudes (Wandinger, 2005). To overcome this overlap issue, two telescopes are installed in Polly^{XT}—a Newtonian telescope with a 300 mm primary mirror for far-field measurements and a 50 mm refracting telescope for near-field measurements. Thus, a complete overlap above 1 km and 120 m, respectively, is enabled (Engelmann et al., 2016).

As a runtime measurement is performed with the lidar, the received signal P is a function of the range R between the lidar and the backscattering object and can be written in the simplest form as

$$P(R) = K \cdot G(R) \cdot \beta(R) \cdot T(R) \tag{2.1}$$

with K a system constant, $G(R)$ and $T(R)$ terms considering the measurement geometry and the transmission/attenuation of the emitted and backscattered light, respectivly, and $\beta(R)$ the backscatter coefficient of the measurement volume. $\beta(R)$ is the primary atmospheric component, describing the strength of the light which is backscattered to the lidar. Furthermore, the transmission term $T(R)$ includes another atmospheric quantity, namely the extinction coefficient α. Both, β and α, are composed of a molecular and a particle component (Wandinger, 2005). The ratio of the extinction coefficient to the backscatter coefficient, called lidar ratio (LR), is, in case of the particle lidar ratio, a characteristic measure for different aerosol types.

2.2.2 The Klett and Raman method

As the particle backscatter coefficient is the component of interest, Eq. 2.1 has to be solved accordingly. For this purpose, the Fernald-Klett method (Fernald, 1984; Klett, 1985; Ansmann & Müller, 2005) can be applied. It uses only elastic backscattering, i.e., the received signal has the same wavelength λ as the emitted one. Using the setup of Polly^{XT}, signals are detected at 355, 532 and 1064 nm, respectively. Equation 2.2 shows the corresponding elastic lidar equation with C^{λ}_{sys}, $O^{\lambda}(R)$ and P_{BG}; a system constant, the overlap function and a background signal, respectively. The subscripts m and p denote the respective molecular and particle components of β and α

$$P^{\lambda}(R) = \frac{C^{\lambda}_{\text{sys}} O^{\lambda}(R)}{R^2} \left[\beta^{\lambda}_{\text{p}}(R) + \beta^{\lambda}_{\text{m}}(R)\right] \exp\left\{-2 \int_0^R \left[\alpha^{\lambda}_{\text{p}}(r) + \alpha^{\lambda}_{\text{m}}(r)\right] \mathrm{d}r\right\} + P_{\text{BG}}. \tag{2.2}$$

β_m and α_m are easily calculated from temperature and pressure vertical profiles. Thus, two unknown quantities (β_p and α_p) are left with only one equation. As a consequence, a particle lidar ratio has to be assumed to replace α_p, i.e., a first guess of the particle type is made, which is the weak point of this method as the solution strongly depends on the correct assumption of LR_p. Furthermore, assuming a vertically constant particle lidar ratio is not realistic since different aerosol types are present at different altitudes and a proper vertically-resolved aerosol characterization is aimed for.

Instead, the Raman method offers a more suitable solution (Ansmann et al., 1992; Ansmann & Müller, 2005). In addition to elastic backscattering, inelastic scattering, i.e., a shift in the wavelength of the received signal due to a change in the rotational-vibrational state of the scattering molecules, is taken into account in this method (Wandinger, 2005). Thus, two signals are received—the elastic signal as described in the Klett method and the inelastic signal at the corresponding Raman wavelengths 387, 607 and 1058 nm. The signal received at a Raman wavelength is described by the inelastic lidar equation (Eq. 2.3) with λ_Ra as the Raman wavelength

$$P^{\lambda_\mathrm{Ra}}(R) = \frac{C_\mathrm{sys}^{\lambda_\mathrm{Ra}} O^{\lambda_\mathrm{Ra}}(R)}{R^2} \beta_\mathrm{m}^{\lambda_\mathrm{Ra}}(R) \exp\left\{ - \int_0^R \left[\alpha_\mathrm{p}^{\lambda}(r) + \alpha_\mathrm{m}^{\lambda}(r) + \alpha_\mathrm{p}^{\lambda_\mathrm{Ra}}(r) + \alpha_\mathrm{m}^{\lambda_\mathrm{Ra}}(r) \right] \mathrm{d}r \right\}. \quad (2.3)$$

As Eq. 2.3 illustrates, the atmospheric attenuation first affects the emitted wavelength and then the Raman wavelength. Furthermore, the backscatter coefficient has only a molecular component depending on the reference gas, e.g., nitrogen or oxygen. The molecular backscatter coefficient can, in turn, be calculated from the molecular number density. The particle extinction coefficients, both at the emitted and the Raman wavelengths, can be related to each other via the Ångström relation (Eq. 2.4)

$$\frac{\alpha_\lambda}{\alpha_{\lambda_\mathrm{Ra}}} = \left(\frac{\lambda_\mathrm{Ra}}{\lambda} \right)^{AE}. \quad (2.4)$$

It means that the ratio of the extinction coefficient at two different wavelengths equals the inverse ratio of the respective wavelengths to the power of the (extinction-related) Ångström exponent AE. In the same way, this relation is valid for the backscatter coefficient (backscatter-related Ångström exponent) and it can also be applied to the particle lidar ratio as well. Assuming an Ångström exponent in advance is also a first guess of the existing aerosol type but does not affect the solution as strongly as the estimation of the particle lidar ratio. After replacing $\alpha_\mathrm{p}^{\lambda_\mathrm{Ra}}$ by using Eq. 2.4, having two equations (the elastic (Eq. 2.2) and the inelastic (Eq. 2.3) lidar equation) for two unknown variables (β_p and α_p) allows us to solve for the particle backscatter coefficient. Thereby, the Raman method offers the great advantage that the particle backscatter and extinction coefficient can be calculated independently from each other and a direct and vertically-resolved measurement of the particle lidar ratio is possible. In addition, the overlap effect is canceled out at least for the particle backscatter coefficient. Unfortunately, this method is limited to nighttime as the Raman signal is very weak and cannot be detected under daylight conditions.

Regardless of the used method (Klett or Raman), the signal needs to be calibrated by using the reference height concept (Ansmann & Müller, 2005). This height is required to be very clean so that only molecular scattering and no particle scattering takes place, i.e., $\beta_\mathrm{p} = 0$.

2.2.3 Polarization

Another important capability of Polly$^\mathrm{XT}$ is the usage of the polarization technique (Sassen, 2005). It means that after the emission of linearly polarized light, a signal is detected in the cross-polar channel (perpendicular to the emitted polarization plane) additionally to the total signal

(all polarization planes). Only if the light is backscattered by depolarizing particles, i.e., non-spherical particles, a signal in the cross-polar channel occurs. Often, the measurement volume of the lidar contains both spherical and non-spherical particles, so that the backscattered light is partly polarized and partly unpolarized. For a quantitative description of the depolarization (Tesche et al., 2009), the (linear) volume depolarization ratio, shown in Eq. 2.5, can be calculated. It comprises the ratio of the cross ($\perp$) to the co-polar/parallel ($\parallel$) backscatter coefficient, which is composed of a molecular (subscript m) and a particle (subscript p) component. δ_v and δ_m denote the volume and molecular depolarization ratio, respectively. The latter is defined as the ratio of $\beta_\mathrm{m}^\perp$ and $\beta_\mathrm{m}^\parallel$

$$\delta_\mathrm{v} = \frac{\beta^\perp}{\beta^\parallel} = \frac{\beta_\mathrm{m}^\perp + \beta_\mathrm{p}^\perp}{\beta_\mathrm{m}^\parallel + \beta_\mathrm{p}^\parallel} = \frac{\frac{\beta_\mathrm{m}\delta_\mathrm{m}}{\delta_\mathrm{m}+1} + \frac{\beta_\mathrm{p}\delta_\mathrm{p}}{\delta_\mathrm{p}+1}}{\frac{\beta_\mathrm{m}}{\delta_\mathrm{m}+1} + \frac{\beta_\mathrm{p}}{\delta_\mathrm{p}+1}} \tag{2.5}$$

$$\text{with } \beta = \beta^\perp + \beta^\parallel,\ \beta^\parallel = \frac{\beta}{\delta+1} \text{ and } \beta^\perp = \frac{\beta\delta}{\delta+1}. \tag{2.6}$$

Using the relations in Eq. 2.6, where δ is either the molecular or particle depolarization ratio, Eq. 2.5 can be solved for the particle linear depolarization ratio δ_p (Eq. 2.7), in which β_m and β_p are the total molecular and particle backscatter coefficient, respectively

$$\delta_\mathrm{p} = \frac{\beta_\mathrm{m}(\delta_\mathrm{v} - \delta_\mathrm{m}) + \delta_\mathrm{v}\beta_\mathrm{p}(\delta_\mathrm{m} + 1)}{\beta_\mathrm{m}(\delta_\mathrm{m} - \delta_\mathrm{v}) + \beta_\mathrm{p}(\delta_\mathrm{m} + 1)}. \tag{2.7}$$

2.2.4 Lidar-derived optical properties

Following from Sect. 2.2.2 and Sect. 2.2.3, a set of five different lidar optical quantities can be determined, which are fundamental properties for the detection of aerosol layers and a proper aerosol type characterization. They are divided into two kinds of properties (Floutsi et al., 2023): extensive properties, such as the particle backscatter and extinction coefficient, depend on the aerosol concentration and indicate where aerosol layers occur in the atmosphere. They are a measure of the amount of aerosol and the strength of the attenuation of the light. On the other hand, intensive properties, such as the particle lidar ratio, the Ångström exponent and the particle linear depolarization ratio, depend only on the properties of single particles but not on the aerosol concentration. An elaborate description of how they can assist to aerosol typing is given in Sect. 2.3.1.

Most of the lidars of the type Polly$^\mathrm{XT}$ allow measurements of the particle backscatter coefficient at 355, 532 and 1064 nm and of the particle extinction coefficient, the particle lidar ratio and the particle linear depolarization ratio at 355 and 532 nm. Near-field measurements are possible for the particle backscatter and extinction coefficient as well as the particle lidar ratio at 355 and 532 nm (Engelmann et al., 2016). Newer systems are additionally equipped with channels enabling far-field measurements of the particle extinction coefficient and the particle linear depolarization ratio at 1064 nm (Haarig et al., 2016, 2022).

Although systematic errors (e.g., polarization effects in the receiver unit, dead-time effects and overlap effects) are generally corrected, the remaining systematic (e.g., reference height and value) and statistical uncertainties have to be considered for the particle backscatter coefficient determined with the Raman method. These aforementioned uncertainties are represented by a relative error of 15 %. In case of the particle extinction coefficient, only statistical uncertainties are considered while the systematic error is neglected. For the calculation of this statistical error, a linear fit of the derivative, including as many data points as the smoothing length, is applied every 7.5 m. The error of this linear fit is then used to derive the error of the extinction coefficient (Althausen et al., 2009; Baars et al., 2012; Engelmann et al., 2016; Baars et al., 2016). For the particle linear depolarization ratio, constant errors of 0.02 at 355 nm and 0.01 at 532 and

1064 nm have been considered in previous studies (e.g., Gebauer et al., 2024) and are applied in this thesis as well. Finally, the errors in the lidar ratio and the Ångström exponent are calculated via the Gaussian error propagation.

2.2.5 Polly^{NET} and the Polly^{NET} processing chain

Several Polly^{XT} lidars already have been operated at more than 20 different locations all around the world in the framework of campaigns (mobile stations, onboard of research vessels) or on a stationary long-term basis. Thus, a broad global coverage of observations has been provided, capturing regions from the Arctic to the tropics and up to Antarctica, although the US and Latin America are underrepresentated. All these observations are gathered in an international, independent and voluntary network called Polly^{NET} (Baars et al., 2016), which is a cooperation of TROPOS and other institutes operating automated and continuously measuring Polly^{XT} systems. The data are collected, processed and displayed in near-real time and are publicly available via the Polly^{NET} webpage (`https://polly.tropos.de/`).

The data processing is performed automatically with the Polly^{NET} processing chain, which is used to retrieve vertical profiles of the aerosol optical properties (Baars et al., 2016; Yin & Baars, 2021). The current version at the starting point of working on this thesis was version 3.3 and was continuously updated to version 4.0, from which the data used in this thesis originates. The new features of version 4.0 are an improved cloud screening invented within the framework of this thesis (see Sect. 3.4) and the use of 24 h measurement periods instead of 6 h periods of the raw data. In both versions, products like the 1-step POLIPHON output (see Sect. 2.3.3) or the lidar target classification (see Sect. 2.3.4) are implemented. For the retrieval of the aerosol optical properties described in Sect. 2.2.4, several steps are performed. At first, measurements in inappropriate weather conditions, i.e., rain and fog, are not considered. In the following preprocessing, background, range and overlap corrections are applied. The next crucial step is the cloud screening. It is applied to the lidar signal in raw resolution, i.e., 30 s or to an increased temporal resolution of up to 300 s, if the signal-to-noise ratio (SNR) is too low. For the cloud screening, the signal gradient algorithm is used in the versions 3.3 and 4.0 of the Polly^{NET} processing chain (Yin & Baars, 2021; Cloud mask - documentation, 2024). This method uses the fact that the lidar signal increases much more rapidly at a cloud base than at the base of a lofted aerosol layer. Thus, the slope of the photon count rate is derived and the cloud base is set to the height where this slope exceeds a certain threshold value. In the current version, this threshold is set to 4×10^6 MHz m. The corresponding time bin of this measurement is flagged as cloudy. Afterwards, an iterative procedure searches for contiguous cloud-free time bins, over which the lidar signal is averaged to derive the vertical profiles of the aerosol optical properties. This averaging is applied to increase the SNR. The minimum and maximum duration of these cloud-free periods is set to 15 min and 1 h, respectively, in the current version of the Polly^{NET} processing chain. However, high-level clouds, i.e., cirrus clouds, are usually not detected by the cloud screening.

Once sufficiently long cloud-free periods are found, the aerosol optical properties can be derived. Therefore, a calibration using a reference height (Ansmann & Müller, 2005) is applied. In the Polly^{NET} processing chain, it is implemented as follows (Baars et al., 2016): different height intervals with an extent of up to 2 km are tested. In this context, high altitudes are preferred, where aerosol-free conditions are more likely to occur. The Rayleigh scattering within these height intervals is calculated from temperature and pressure profiles. Furthermore, for height intervals for which the total SNR exceeds a certain threshold value (wavelength dependent value ranging between 1 and 2), the Rayleigh fit of the range and background corrected elastic backscatter signal is computed, i.e., it is normalized with the molecular attenuated backscatter coefficient. For aerosol-free conditions, the lidar signal is completely proportional to the molecular atten-

uated backscatter coefficient. Otherwise, a significant deviation of both quantities is observed. In this context, large wavelengths are more affected than small ones, often leading to difficulties in the calibration for the lidar signal at 1064 nm compared with 355 and 532 nm. Finally, the height interval with the best quality results of the Rayleigh fit is used as reference height and the aerosol optical properties are derived. The vertical profiles are saved with a user-defined vertical resolution, which is 99 bins, i.e., 742.5 m for the far-field measurements and 51 bins, i.e., 382.5 m for the near-field measurements in the version 4.0 of the Polly$^{\mathrm{NET}}$ processing chain. For this smoothing procedure, a moving average filter is applied, i.e., each data point at an arbitrary height contains information from half of the smoothing length below this point to half of the smoothing length above it (Yin & Baars, 2021).

2.3 Lidar-based aerosol characterization

2.3.1 DeLiAn—data collection of intensive lidar-derived optical properties

To achieve a proper identification of different aerosol types by using lidar measurements, the intensive optical properties (the particle lidar ratio, the particle linear depolarization ratio and the extinction and backscatter-related Ångström exponents) play a fundamental role. As briefly mentioned in Sect. 2.2.4, they represent a measure for the microphysical properties of single particles. In Sect. 2.2.3, the particle linear depolarization ratio was already introduced to be a proxy of the particle shape with large values being caused by non-spherical particles. Instead, spherical particles lead to low values of the particle linear depolarization ratio. Furthermore, the particle lidar ratio represents a typical quantity for different aerosol types. There are correlations with the particle size, shape and absorption properties (Floutsi et al., 2023). It is usually inversely related to the particle size and directly related to the absorption efficiency. Non-spherical particles usually cause higher values of the particle lidar ratio than spherical particles of the same size range. As a third intensive optical property, the extinction and backscatter-related Ångström exponents (cf. Sect. 2.2.2) describe the spectral dependence of the particle extinction and backscatter coefficient, respectively. Ångström exponents are an indicator for the size and absorption properties of the particles and, similarly to the particle lidar ratio, inversely related to the particle size. Small values of the Ångström exponent of about 0.5–1.0 are typical for large particles, such as marine aerosol and desert dust, whereas small particles, such as urban pollution and biomass burning aerosol/smoke with radii < 500 nm, cause values higher than 1.5 (Hofer et al., 2020b).

While the individual intensive optical quantities allow drawing conclusions about certain microphysical properties of the analyzed particles, a proper aerosol characterization requires the combination of these quantities. This fact is emphasized with regard to aerosol types causing the same particle linear depolarization ratio but having different values of the particle lidar ratio. Thus, both types cannot be distinguished by measuring the depolarization alone but additional measurements of the particle lidar ratio are required. Thereby, especially the combination of the particle lidar ratio and the particle linear depolarization ratio provides the strongest basis for a correct separation of different aerosol types (Burton et al., 2012; Floutsi et al., 2023). However, the development of aerosol typing schemes requires a basis of lidar measurements of the intensive properties. An overview of particle lidar ratio and Ångström exponent values for different aerosol types from global lidar measurements within a ten-year period was already provided by Müller et al. (2007). In this summary, the aerosol types marine aerosol, desert dust, urban haze/industrial aerosol, urban pollution mixed with Arctic haze, aged North American urban haze and forest fire smoke after long range transport and South and South East Asian aerosol were considered. An extended database of intensive optical properties can be found in the publication of Floutsi et al. (2023). This data collection called DeLiAn includes the particle

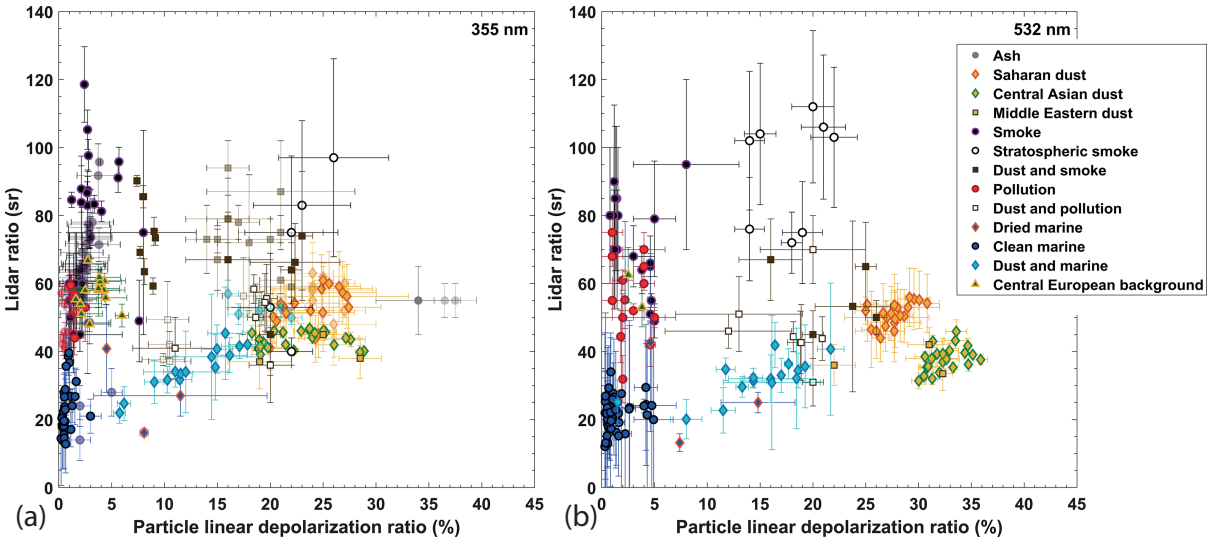

Figure 2.1: Lidar ratio in dependence of the particle linear depolarization ratio at (a) 355 and (b) 532 nm for different aerosol types collected in the DeLiAn data set (Floutsi et al., 2023).

Table 2.1: DeLiAn mean values of the lidar ratio and particle linear depolarization ratio (Depol) at 355 and 532 nm as well as the backscatter-related Ångström exponent (subscript b) between 355 and 532 nm and between 532 and 1064 nm and the extinction-related Ångström exponent (subscript e) for the aerosol types and aerosol mixtures relevant at Mindelo (Floutsi et al., 2023).

Aerosol type	Lidar ratio [sr]		Depol		Ångström exponent		
Wavelength	355	532	355	532	e355/532	b355/532	b532/1064
Saharan dust	53.5±7.7	53.1±7.9	24.4±2.5	28±1.3	0.1±0.2	0.03±0.08	0.5±0.1
Smoke	68.2±7.4	71.8±11.1	2.7±1.3	2.9±0.6	1.3±0.3	1.4±0.1	1.2±0.1
Dust-smoke	72.1±7.7	56.3±6.5	15.7±2	18.9±1.4	1.4±0.2	0.5±0.1	1±0.05
Pollution	51.1±8.7	47.4±7.4	1.1±0.3	2.8±1	1.8±1.4	1.2±0.7	0.9±0.5
Dust-pollution	48.5±9.2	46.4±8	15.7±1.7	17.7±2.5	0.7±0.4	0.3±0.1	0.9±0.1
Clean marine	22.4±5.6	21.9±13.4	1.3±0.3	1.4±0.3	0.7±1.3	0.8±0.1	0.5±0.1
Dried marine	28±6.6	26.9±10.6	7.5±1.7	8.3±1.1	1.1±1.3	0.6±0.04	-0.07±0.07
Dust-marine	39.4±5.6	32±7.8	14±1.5	14.7±1.1	0.5±0.5	0.3±0.1	0.6±0.1
Volcanic ash	51±7.5	48±7.5	36±2.3	–	0.8±0.6	0.6±0.4	1±0.4

lidar ratio, the particle linear depolarization ratio and the Ångström exponent at 355 and 532 nm based on globally-distributed multiwavelength Raman-polarization lidar observations. The consideration of different field campaigns, different locations and many years of observations ensures a large spatial and temporal coverage. Furthermore, DeLiAn includes a set of various aerosol types and it also takes into account new types, such as Central Asian dust, dried marine aerosol and stratospheric smoke. It is an important feature of the data set as Müller et al. (2007) already pointed out the variation of the particle lidar ratio of desert dust particles with their size range, their shape (also related to the size range) and the chemical composition. Thus, the optical properties of desert dust have to be considered based on the source of the dust. These global differences are found again in DeLiAn comparing the properties of Saharan dust and Central Asian dust, whereat the latter shows up with lower values (35–45 sr). On the other hand, clean marine aerosol does not show a source-dependent variability, while dried marine aerosol, occurring at a relative humidity below 45 %, has to be considered separately. Since it develops a cubic-like shape, the values of the particle linear depolarization ratio are higher. The complete DeLiAn

data collection considering the particle lidar ratio and the particle linear depolarization ratio is illustrated in Fig. 2.1. Table 2.1 summarizes the respective mean values of the intensive optical properties for the selected aerosol types which play a role in the Cabo Verde region.

2.3.2 The separation of smoke and dust

While the combination of different intensive optical properties enables a proper aerosol characterization, a pure separation of aerosol into a dust and a non-dust component can be achieved by using the particle linear depolarization ratio only. The corresponding method is described in Tesche et al. (2009). Assuming a mixture of two different aerosol types with one component strongly depolarizing (in this case desert dust) and the other almost non-depolarizing light (Tesche et al., 2011b), the particle linear depolarization ratio is used to split the total particle backscatter coefficient into a dust backscatter coefficient (β_{d}) and a non-dust backscatter coefficient (β_{nd}). Similarly to the division of the volume depolarization ratio into a molecular and a particle component, as described in Sect. 2.2.3, the particle linear depolarization ratio can be split into a dust (subscript d) and a non-dust (subscript nd) component. The relations shown in Eq. 2.6 are applied again and the non-dust backscatter coefficient is replaced by $\beta_{\mathrm{nd}} = \beta_{\mathrm{p}} - \beta_{\mathrm{d}}$ with β_{p} the total particle backscatter coefficient. Thus, Eq. 2.8 is derived and can be solved for the dust backscatter coefficient β_{d}:

$$\delta_{\mathrm{p}} = \frac{\beta_{\mathrm{nd}}^{\perp} + \beta_{\mathrm{d}}^{\perp}}{\beta_{\mathrm{nd}}^{\parallel} + \beta_{\mathrm{d}}^{\parallel}} = \frac{\frac{\beta_{\mathrm{nd}}\delta_{\mathrm{nd}}}{\delta_{\mathrm{nd}}+1} + \frac{\beta_{\mathrm{d}}\delta_{\mathrm{d}}}{\delta_{\mathrm{d}}+1}}{\frac{\beta_{\mathrm{nd}}}{\delta_{\mathrm{nd}}+1} + \frac{\beta_{\mathrm{d}}}{\delta_{\mathrm{d}}+1}} \tag{2.8}$$

$$\beta_{\mathrm{d}} = \beta_{\mathrm{p}} \frac{(\delta_{\mathrm{p}} - \delta_{\mathrm{nd}})(\delta_{\mathrm{d}} + 1)}{(\delta_{\mathrm{d}} - \delta_{\mathrm{nd}})(\delta_{\mathrm{p}} + 1)}. \tag{2.9}$$

While δ_{p} is calculated from the measured β_{p}, δ_{d} and δ_{nd}, the particle linear depolarization ratio of the dust and non-dust components have to be assumed. Previous lidar measurements in regions, where pure dust and non-dust aerosol occurs, assist the estimation of δ_{d} and δ_{nd}, as well as a pure dust particle lidar ratio. The latter is in turn used to calculate the pure dust extinction coefficient from β_{d}. Furthermore, the non-dust backscatter coefficient is obtained by substracting β_{d} from β_{p}. This separation method is applied to one wavelength first. Using the Ångström relation, the respective quantities at the remaining wavelengths are calculated. The procedure described in this section is also called 1-step POLIPHON method, while the complete POLIPHON method or 2-step POLIPHON, including the CCN and INP derivations, is explained in the following section.

2.3.3 POLIPHON

Going one step further, even microphysical properties of the aerosol particles can be derived from the measured optical properties. For this purpose, the polarization-lidar photometer networking algorithm (POLIPHON; Mamouri & Ansmann, 2017; Ansmann et al., 2019) was implemented. It is used to calculate the particle number, surface and volume concentration of the observed aerosol particles. At the end, vertical profiles of the particle mass and the CCN and INP concentration can be obtained. POLIPHON can be applied for the dust and non-dust components, as derived in Sect. 2.3.2, each. Furthermore, POLIPHON requires the synergy of a multiwavelength Raman-polarization lidar as Polly$^{\mathrm{XT}}$ and the long-term data base of the AERONET (Aerosol Robotic Network). While the former is essential for measuring the optical properties and the separation of the dust and non-dust components, the latter relates the optical properties to the cloud-relevant properties with the help of conversion factors.

The first step in the POLIPHON algorithm is the separation of the dust and non-dust

backscatter and extinction coefficients into fine mode (radii $< 500\,\mathrm{nm}$) and coarse mode (radii $> 500\,\mathrm{nm}$). Further calculations are applied to the dust and non-dust and fine and coarse mode profiles, each. From the extinction coefficient, the particle number, surface and volume concentration are calculated. The latter can be converted into the mass concentration. The particle number concentration is again derived for different size ranges, namely particles with radii $> 100\,\mathrm{nm}$ and $> 250\,\mathrm{nm}$. While the smaller size mode is used for calculating the CCN concentration, the larger size mode and the surface number concentration for particles with radii $> 100\,\mathrm{nm}$ are integrated into the calculation of the INP concentration.

2.3.4 Target categorization

A target categorization, which uses only lidar measurements, has been established (Baars et al., 2017). With this method, aerosol and cloud particles can be classified according to their physical properites, i.e., their shape and size, while an attribution to their source is neglected. The latter typing mechanism would require to include further instruments besides the lidar. Within the lidar-only target classification, 11 categories are considered, which are clean atmosphere, non-typed particles of low concentration, small spherical particles, large spherical particles, non-spherical particles and a mixture of spherical and non-spherical particles for aerosol particles as well as non-typed clouds, liquid water clouds, likely liquid water clouds, ice clouds, likely ice clouds in case of cloud particles.

The typing mechanism is applied to 24 h measurements with a temporal resolution of 30 s (Yin & Baars, 2021) and uses the quasi-particle backscatter coefficients (representing the best estimates for the particle backscatter coefficients) at 532 and 1064 nm, the quasi-particle Ångström exponent between both, the volume depolarization ratio at 532 nm and the corresponding quasi-particle linear depolarization ratio. In this algorithm, the quasi-particle backscatter coefficient is used because it is the best estimate for the particle backscatter coefficient. In this approach, the attenuation caused by particles is neglected in the lidar equation (cf. $\alpha_\mathrm{p}^\lambda = 0$ in Eq. 2.1). The result is then multiplied by a constant lidar ratio of 55 sr in version 1 of the target categorization, similarly to the Klett method (cf. Sect. 2.2.2), to obtain the quasi-particle extinction coefficient. In a newer version (version 2), additionally, the Raman signal is considered to derive the quasi-particle extinction coefficient via the Ångström relation. However, there are differences between both versions, which are the missing target categorization in the overlap region for version 1. Furthermore, version 2 is less affected by the attenuation due to aerosol and provides a higher stability of the calibration constant. In contrast, the SNR is lower during daytime than it is for version 1. No matter which version is applied, in the following procedure, the quasi-particle extinction coefficient is inserted into the lidar equation, which can be solved for the quasi-particle backscatter coefficient. From the latter, the intensive properties are calculated.

The first step of the typing procedure is to detect non-ice clouds. Due to the strong attenuation of the lidar signal by liquid water and mixed phase clouds, only the cloud base and the hydrometeors a few meters above can be detected. Thus, no particle classification is possible above a liquid water or non-typed cloud. For the identification of these clouds, the Cloudnet target categorization (Hogan & O'Connor, 2004; Illingworth et al., 2007) is applied detecting clouds where the quasi-particle backscatter coefficient at 1064 nm exceeds $2 \times 10^{-5}\,\mathrm{m^{-1}\,sr^{-1}}$ and a signal decrease by a factor of ten is observed in the 250 m above the maximum backscatter signal. At first, the clouds are flagged as non-typed. They are further typed into likely liquid droplets when the quasi-particle linear depolarization ratio is smaller than 0.05 and into liquid droplets when additionally the quasi-Ångström exponent is below 0.5. After the identification of these optically thick clouds, the quasi-particle backscatter coefficient at 1064 nm is used to detect clean atmosphere (values below $1 \times 10^{-8}\,\mathrm{m^{-1}\,sr^{-1}}$ and a SNR > 0.5 at 355 nm in raw resolution of 30 s, otherwise no typing is available) or to induce the further typing procedure

(values $> 1 \times 10^{-8}\,\mathrm{m^{-1}\,sr^{-1}}$). If the quasi-particle backscatter coefficient at 1064 nm is smaller than $2 \times 10^{-7}\,\mathrm{m^{-1}\,sr^{-1}}$, the pixels are flagged as non-typed particles, which can be aerosol or cloud particles. Otherwise, large non-spherical particles are classified for a quasi-particle linear depolarization ratio > 0.2. They are flagged as small spherical particles for a quasi-particle linear depolarization ratio < 0.07 and a quasi-Ångström exponent ≥ 0.75 and as large spherical particles for the same range of the quasi-particle linear depolarization ratio but a quasi-Ångström exponent < 0.75. If the quasi-particle linear depolarization ratio is between 0.07 and 0.2, a mixture of spherical and non-spherical particles is detected. Finally, ice crystals are identified independently from this procedure so that previously typed pixels might be overwritten. While the same threshold of the quasi-particle backscatter coefficient at 1064 nm is used for the detection of ice crystals as it is for the typing of aerosol particles, it additionally considers the volume depolarization ratio at 532 nm. If the latter is larger than 0.3, the pixels are flagged as likely ice crystals. If, additionally, the quasi particle linear depolarization ratio is larger than 0.35, they are classified as ice crystals. However, ice clouds sometimes may be not classified or typed as non-typed aerosol or clouds because of a low SNR of the depolarization measurements but an existing backscatter signal at 1064 nm.

Based on the target classification, a product including information about the cloud occurrence is derived within the Polly$^{\mathrm{NET}}$ processing chain. In this context, the height of the cloud base and the cloud top, the phase and its probability and the number of cloud layers are derived (Yin & Baars, 2021).

2.4 Saharan dust and its transport in the region of Cabo Verde

2.4.1 Typical meteorological conditions over the African continent and Cabo Verde

The North African region and the Cabo Verde islands are mainly influenced by the inner tropical convergence zone (ITCZ) and its movement over the year as well as the strength and location of the subtropical anticyclone (Azores high) over the eastern Atlantic and North Africa. The subtropical anticyclone controls the Harmattan winds (dry northeasterly winds over the Sahara and Sahel region during winter and spring), which have a major impact on the annual variability of dust activity, main dust sources and dust transport beyond the African continent resulting in a strong seasonal cycle (Prospero et al., 2002; Knippertz et al., 2011; Tesche et al., 2011a). For the Saharan desert, there are two main dust seasons with intense dust storms, one from December to February and the other from May to August (Knippertz et al., 2011; Rodríguez & López-Darias, 2021). Mineral dust is predominantly transported towards the west to the Caribbean, the mid-latitude western North Atlantic and the southeastern part of the US due to the subtropical jet and easterly waves but also to Europe and the Middle East. The peak of this dust transport occurs in northern hemispheric summer. Also in northern hemispheric winter, there is a dust transport towards South America. During this time of the year, the dust activity in North Africa is largest in the low latitudes and shifts to higher latitudes during the year, driven by the northward movement of the ITCZ. A minimum in the dust transport can be observed in fall (Prospero et al., 2002; Tesche et al., 2011a).

Besides Saharan dust, the African continent is an important source for biomass burning aerosol (BBA, smoke) mainly originating from agricultural activity following a seasonal cycle as well. During winter (Fig. 2.2, left plot), the fire activity is greatest close to the equator in the southern west Africa, while it shifts more to the south during summer (Fig. 2.2, right plot). Thus during this season, the burning regions and the dust sources are clearly separated by the more in the north located ITCZ. Instead, during winter, when the ITCZ is shifted more to the south,

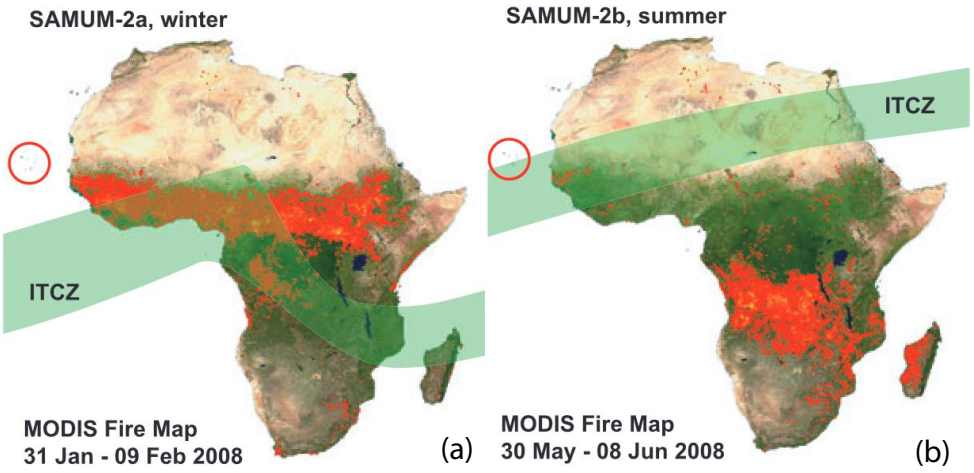

Figure 2.2: Northern hemispheric (a) winter and (b) summer conditions of the location of the inner tropical convergence zone (ITCZ) and the wildfire areas on the African continent as representative for the SAMUM–2 campaign (Tesche et al., 2011a).

the BBA and the dust get mixed over low-latitude West Africa and the Gulf of Guinea, mainly driven by deep convection, and a dust-smoke-mix is transported towards the west (Knippertz et al., 2011; Tesche et al., 2011a).

To study the westward transport of pure dust as well as mixtures of dust and smoke, an optimal study area can be found with the Cabo Verde islands (marked with red circles in Fig. 2.2) located 900 km west of the West African coast directly in the outflow zone of the dust transport (Gong et al., 2020). Included in the Sahel climate belt at the edge of the main convective intensity of the ITCZ, they are characterized by an arid and semi-arid climate with a high variability in precipitation and few rain events with great intensity in the rainy season from August to October under the influence of the ITCZ (Martins et al., 2018). In the dry season, Cabo Verde is under anticyclonic influence. Furthermore, constant northeasterly trade winds are prevailing in that region and often stratocumulus clouds occur, especially in the planetary boundary layer (PBL; Martins et al., 2018; Gong et al., 2020; Rodríguez & López-Darias, 2021).

2.4.2 Overview of previous measurement campaigns over West Africa and Cabo Verde

The Saharan region has been an area of scientific interest for quite a long time. A large number of campaigns have already been carried out in West Africa and at Cabo Verde to study the spatial distribution and the optical and microphysical properties of Saharan dust and to use the findings for the validation of numerical models. Aircraft and ground-based in-situ measurements took place in the framework of the Saharan Dust Experiment (SHADE; Formenti et al., 2003) over the Cabo Verde region in September 2000, the Dust Outflow and Deposition to the Ocean project (DODO; McConnell et al., 2008) at Dakar, Senegal, in February and August 2006, the Geostationary Earth Radiation Budget Intercomparison of Longwave and shortwave radiation (GERBILS; Haywood et al., 2011) over the southwestern Sahara and the coastal stretches of the Atlantic in June 2007 and the Fennec campaign (Ryder et al., 2013; Rocha-Lima et al., 2018) at Mauritania and Mali in June 2011. Furthermore, with the African Monsoon Multidisciplinary Analysis (AMMA; Lebel et al., 2010), a large interdisciplinary study on the West African monsoon was conducted including different spatial scales and ground-based and airborne in-situ and remote sensing instruments as well as radiosoundings. At three different stations in Senegal,

Mali and Niger, measurements of PM_{10} and observations with AERONET sun photometers and a micro-lidar were performed from 2005 to 2007 with a special focus on the period January–February 2006. As a part of AMMA, NASA AMMA (NAMMA; Chen et al., 2011) included aircraft in-situ observations of Saharan dust layers over the Cabo Verde region.

While the DODO campaign already contrasted observations of a summer and a winter month and a micro-pulsed lidar has been used in the context of AMMA, the Saharan Mineral Dust Experiment (SAMUM; Ansmann et al., 2011a) represents a major step forward in terms of lidar observations and a seasonal point of view. This field experiment was conducted in two parts. Pure Saharan dust near the source region was investigated at Southern Morocco in May and June 2006 during SAMUM–1 (Freudenthaler et al., 2009). Far-transported dust as well as mixtures of dust with marine, urban and biomass burning aerosol where studied at Praia, on the island Santiago at Cabo Verde, during SAMUM–2a (15 January–15 February 2008) and SAMUM–2b (15 May–15 June 2008; Groß et al., 2011; Tesche et al., 2011a,b). During this part of the campaign, the impact of aging and mixing processes on the microphysical, optical and radiative properties of Saharan dust as well as contrasting the summer and winter period was of special interest. Besides ground-based in-situ measurements, sun photometer observations, radiosoundings and ground-based radiation measurements, it was the first time that an aerosol multiwavelength-Raman polarization lidar was used to study Saharan dust in that region. Furthermore, wind measurements with a Doppler lidar and aircraft observations with a High Spectral Resolution Lidar (HSRL) were performed.

In addition to studying the westward transport of Saharan dust at its beginning, the Saharan Aerosol long-range transport and aerosol-cloud-interaction experiment (SALTRACE; Weinzierl et al., 2017) aimed to investigate the impact of aging of the dust particles on the radiative effect and cloud microphysical processes. For this purpose, the complete transport from West Africa to the Caribbean was captured focusing on dust removal aspects and the annual variability of the dust flow into the Caribbean. Again, a multiwavelength-Raman polarization lidar was operated at Barbados in June and July 2013 (Groß et al., 2015). Previously, a research vessel equipped with this lidar crossed the Atlantic, tracking the pathway of the dust transport in April and May 2013, which covers the final phase of the burning season at southern West Africa (Rittmeister et al., 2017). In addition, the shipping route provided ideal conditions for pure marine observations. Further instruments, such as a sun photometer and ground-based and airborne in-situ measurements were included. Research flights were performed both, at Cabo Verde and in the Caribbean (Weinzierl et al., 2017).

Ground-based in-situ measurements of aerosol at Cabo Verde and in particular at Mindelo on the island São Vicente were performed from 13 September to 13 October 2017 in the context of the project 'Marine biological production, organic aerosol particles and marine clouds: a Process chain' (Gong et al., 2020, MarParCloud). PM_{10} was measured at a sea level station (10 m a.s.l.) and at a mountain station (744 m a.s.l.) on the island São Vicente and during a vehicle campaign on the island Santo Antão and at Mindelo, São Vicente, from 1 to 7 October 2019 (Rodríguez & López-Darias, 2021). For the latter campaign, measurement devices for PM_{10}, $PM_{2.5}$ and PM_1 were installed on the roof of a slow moving vehicle providing high resolution measurements of transects (movement at ground level), vertical profiles (movement from sea level to 1500 m a.s.l. within only few horizontal kilometers) and stationary measurements near specific sources. The low number of other vehicles passing the measurement vehicle ensured the representativeness of the measurements for the ambient air. However, it should be noted that both campaigns covered only a period during fall.

2.4.3 Aerosol conditions over Cabo Verde

Thanks to the aforementioned campaigns, some information about the aerosol conditions over Cabo Verde has been provided. Yet, it is well known that the major aerosol types occurring in that region are especially Saharan dust, but also marine aerosol and BBA from the African continent. PM_{10} at São Vicente island is with 70 % dominated by Saharan dust and marine aerosol of which a background aerosol load is always present (Gong et al., 2020) but being only a minor contributor to the AOD (Knippertz et al., 2011). The AOD is mainly controlled by dust and smoke. The latter occurs during wintertime (Tesche et al., 2011a,b).

However, for their observation period in October 2019, Rodríguez & López-Darias (2021) found a significant variability of the concentration of PM_{10} and the particle size, represented by the PM_x ratios, with regard to the location of the measurements on the islands São Vicente and Santo Antão and the meteorological conditions. High PM_x concentrations were recorded for Saharan dust events, while local sources had only low scale impact on the PM_x concentrations. The characteristic $PM_1/PM_{2.5}$ ratios were linked to vehicle exhaust, biomass burning and local dust. Furthermore, the vertical profiles of PM_x and the depth of the marine PBL strongly varied depending on the air flow above the marine PBL. The latter was constantly influenced by the trade winds. The largest extents of the PBL with layer top heights up to 1400 m were observed when the air above originated from the North Atlantic. In this case, PM_x quickly decreased with height. Under African easterly inflow, the PBL reached up to 500 m. Above hydrophilic aerosols were imbedded in relatively humid air. In contrast, under influence of the SAL, the PBL was restricted to 70 m and complex aerosol structures were observed even within the SAL, where dry layers with high dust load alternated with more humid layers having a lower aerosol load. Concerning the vertical aerosol stratification, from Gong et al. (2020), we learn that during the absence of clouds the PBL was well mixed in fall 2017 so that the aerosol conditions at sea level are representative for the mountain level as well.

While the described observations only cover a single season, namely northern hemispheric fall, and are restricted to the lowermost 2 km of the troposphere, the results of SAMUM–2 allow a comparison between summer and winter aerosol conditions by vertical profiles of lidar optical properties and sun photometer measurements (Ansmann et al., 2011a; Tesche et al., 2011a,b; Tesche, 2011). The latter was used to derive the AOD at 500 nm, which showed only little seasonal variation. During summer it was with on average 0.4±0.02 slightly larger than during winter, when a mean value of 0.35±0.18 was observed. Similar findings were seen for the aerosol layer top height with a slightly smaller mean value of 3.5±1.2 km during winter compared with 4.4±0.7 km during summer. Anyhow, there was some variability concerning the maximum aerosol layer top height. While during summer, most aerosol layers reached up to 5 or 6 km, during winter, aerosol layers up to 6 km as well as shallower layers only reaching up to 1 or 3 km were found. The differences concerning the layer extent were much more pronounced with regard to the dominating aerosol type of these layers. Thus, pure dust layers were quite shallow in winter (average depth of 1.0±0.1 km) and much broader in summer (average depth of 4.1±0.7 km). However, the main seasonal differences were observed with regard to the aerosol types which are present over Cabo Verde. As well visualized in Fig. 2.3, the layering during summer was quite simple. In all cases, a geometrically thick layer of pure dust occurred above a shallow marine PBL. In contrast, during wintertime, a much more complex aerosol stratification was observed including many different scenarios like optically and geometrically thick layers of dust-smoke mixtures above thin layers of pure dust sometimes with a marine PBL below. In addition, there were also cases without any pure dust but only dust-smoke mixtures above the marine PBL. Pure dust conditions, with or without a marine PBL, and completely clean marine cases were observed as well.

As could be seen in this chapter, Saharan dust and the aerosol conditions over Cabo Verde

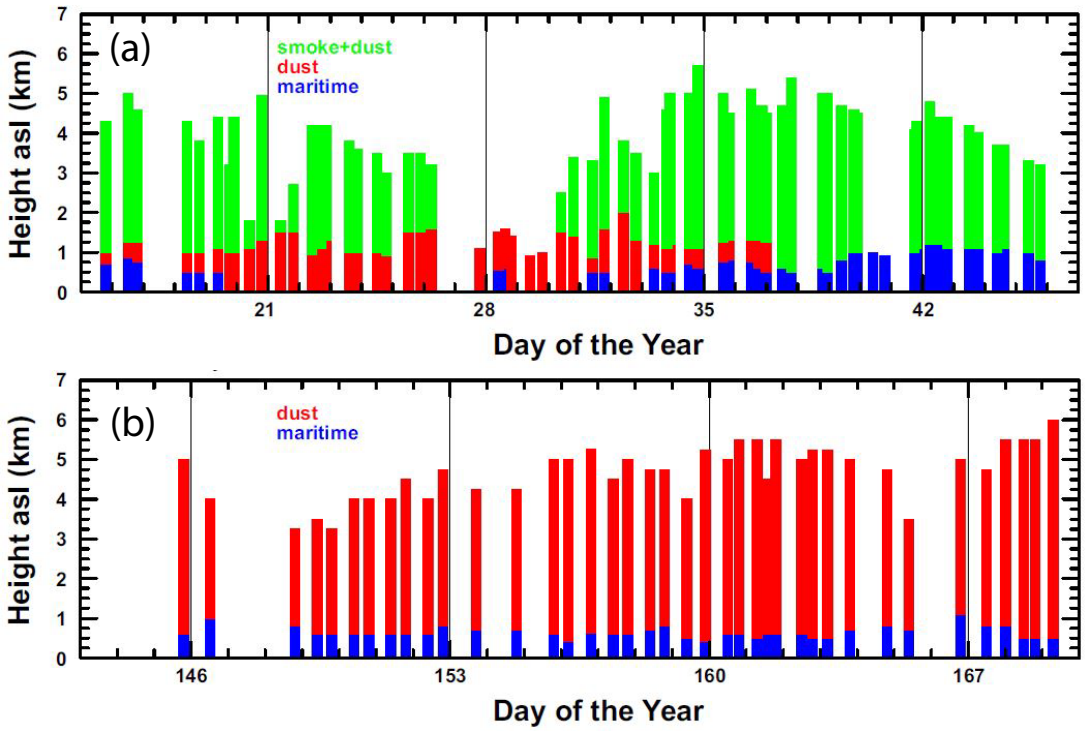

Figure 2.3: In a time series (day of the year 2008 on the x-axis) for the SAMUM-2a winter (top) and SAMUM-2b summer (bottom) campaign the observed aerosol layers are illustrated, including their vertical extent and aerosol type (Tesche, 2011).

have been subjects to numerous studies till now, as the observed aerosol types have various direct and indirect effects on the global radiation budget. At Cabo Verde, a strong influence of Saharan dust was reported in multiple studies and large seasonal differences between northern hemispheric summer and winter were revealed, representing a dust season and a mixing season. Powerful techniques to detect and characterize highly-resolved vertical profiles of aerosol particles exist. How the existing knowledge from literature and previous campaigns and the available measurement techniques and typing algorithms can be used to answer the current research question will be shown in the next chapters.

Chapter 3

Instrumentation and methodology

3.1 The Joint Aeolus Tropical Atlantic Campaign (JATAC) and ASKOS

This thesis is based on the Joint Aeolus Tropical Atlantic Campaign (JATAC; Fehr et al., 2023; Borne et al., 2024) and its ground-based part ASKOS (Marinou et al., 2023). ASKOS took place around Mindelo, Cabo Verde, between 2021 and 2022 with three intense phases in September 2021, June 2022 and September 2022. The ASKOS campaign included a collaboration of several institutions (e.g., the National Observatory of Athens (NOA), the Leibniz Institute for Tropospheric Research (TROPOS), the Cyprus Institute (CyI) and the Romanian National Institute for Research and Development for Optoelectronics (INOE) with the main goal of collecting synergistic measurements for a quality-assured reference data set for the calibration and validation activities of ESA's satellite Aeolus (Straume-Lindner et al., 2021). During this campaign, Aeolus was passing directly over Mindelo each Friday evening at around 19:30 UTC. In the framework of JATAC's ground-based part ASKOS, called after a Greek legend, a complete aerosol and cloud remote sensing facility of the Aerosol, Clouds and Trace Gases Research Infrastructure (ACTRIS, 2024; Laj et al., 2024) has been set up and continuously operated at Mindelo from June 2021 until today. It includes the multiwavelength-Raman-polarization lidar Polly^{XT} (cf. Sect. 2.2), a CIMEL Sun Sky Lunar photometer of type CE318-T, which is part of the Aerosol Robotic Network (AERONET; Holben et al., 1998), a scanning Doppler wind lidar (Pearson et al., 2009), a microwave radiometer and the 94 GHz cloud radar FRM4Radar of ESA. During the intense phases, additional instrumentation was used, e.g., the eVe lidar of ESA (Paschou et al., 2022), the polarization lidar WALL-E (Tsekeri et al., 2021), airborne in-situ measurements (Yus Díez et al., 2023), UAV (Kezoudi et al., 2023), radiosondes (Marinou et al., 2023; Borne et al., 2024) and radiation measurements. The data are meanwhile available at ESA's Atmospheric Validation Data Centre (Amiridis et al., 2023). The relevant instruments for this thesis are described in the next section.

3.2 Measurement site and instrumentation

The measurement site of ASKOS has been set up at the Ocean Science Center Mindelo (OSCM, 16.878°N, 24.995°W, 10 m a.s.l.), which is located on the west coast of the island São Vicente belonging to the Cabo Verde Islands. Anthropogenic influence is relatively low. Cabo Verde is located downwind the Saharan desert and in the trade wind zone with the predominant wind direction being northeast in the lower altitudes. During the night, cumulus convection usually occurs in the PBL above Mindelo. As Mindelo is located in the tropics, there is only low annual

variation of the time of sunset (20:15 UTC at northern hemispheric mid summer, 19:34 UTC at equinox, 19:11 UTC at northern hemispheric mid winter) and the time of sunrise (07:07, 07:29 and 08:04 UTC, respectively). During the 11–13 h-lasting nights, the application of the Raman method is possible.

For this study, mainly the Polly^{XT} lidar (Engelmann et al., 2016; Baars et al., 2016; Gebauer et al., 2024) was used, which has a few improvements compared with the previous Polly^{XT} systems. Instead of using the typical flashlamp pumped Nd:YAG laser having a repetition rate of 20–30 Hz, the system deployed at Mindelo is equipped with a diode pumped Nd:YAG laser, which has a higher repetition rate of 100 Hz. This feature allows to derive vertical profiles of the aerosol optical properties from signals averaged over short time periods down to 15 min. Due to the frequent cloud occurrence at Mindelo with often short cloud-free periods, this capability is particularly important for this measurement site. The receiver unit of the lidar consists of 15 channels. Thus, far-field measurements of the elastic backscatter coefficient at 355, 532 and 1064 nm, the inelastic backscatter coefficient at 387, 607 and 1058 nm, the cross-polar signal at 355, 532 and 1064 nm and the inelastic signal from water vapor at 407 nm are possible. Near-field measurements are available at 355, 532, 387 and 607 nm. Furthermore, a dual-field-of-view polarization channel (Jimenez et al., 2020a) can be used for the determination of microphysical liquid-water properties to study aerosol-cloud-interactions (Jimenez et al., 2020b). With the described setup, vertical profiles of the particle backscatter and extinction coefficients, the lidar ratio and the particle linear depolarization ratio each at 355, 532 and 1064 nm can be derived as well as the backscatter-related and extinction-related Ångström exponent between the different wavelengths. A new feature of the Polly^{XT} at Mindelo is the possibility to retrieve the backscatter and extinction coefficients and the lidar ratio at 1064 nm via the rotational Raman technique (Haarig et al., 2016) in addition to the well known standard of the vibrational-rotational Raman methods applied at 355 and 532 nm. As the signals detected on this channel require a specific calibration (Haarig et al., 2022), they are not yet implemented in the Polly^{NET} processing chain and were not used in this study.

Furthermore, measurements of the AERONET sun photometer (Holben et al., 1998) operated at the OSCM were taken for comparison with the lidar measurements. With the sun photometer, the AOD at 340, 380, 440, 500, 675, 870, 1020 and 1640 nm, respectively, can be derived. In addition, some more optical properties are available, which are the columnar Ångström exponent between six wavelength pairs, the volume size distribution, the refractive index, the single-scattering albedo, the absorption AOD, the extinction AOD, the asymmetry factor and the phase function.

3.3 Description of the data set

The basis for this study is a two-year data set of continuous lidar measurements obtained during the JATAC campaign at Mindelo. The data set captures the time period from 1 July 2021 to 31 August 2023. As the lidar has been installed at Mindelo in June 2021 and measurements were available only for a few days at the end of this month, July 2021 was chosen as starting point for the data set, because it was the first complete month having measurements. The endpoint of this data set was chosen accordingly to capture two complete years of measurements. August 2023 was included additonally as there was a large data gap for August in the year before. Out of this period, a sub data set was created. All nights from Friday 18 UTC to Saturday 6 UTC were considered to guarantee representative and independent measurements. The nighttime measurements allowed for a consistent derivation of vertically-resolved aerosol optical properties profiles with the Raman method (cf. Sect. 2.2.2). From now on, this sub data set will be referred to as Fri/Sat nights. The measurement time during the Fri/Sat nights was preferred as it included

the time of the direct overpass of the Aeolus satellite over Mindelo. The detailed analysis of the data of these measurement periods done for this study provides also a mature basis for future Aeolus-Polly^{XT}-intercomparison activities. In total, the described two-year period includes 113 nights. Despite all efforts to guarantee continuous measurements, measurement gaps due to failure of Polly^{XT} or maintenance on the lidar system occurred. Hence, on 24 of the 113 nights no data is available. These data gaps are mostly distributed homogeneously among the two-year period except one longer period from 15 July to 2 September 2022. Thus, data from 89 nights could be used for the processing.

3.4 Processing of vertical profiles—cloud screening

Vertical profiles of the aerosol optical properties (particle backscatter and extinction coefficients, lidar ratio, particle linear depolarization ratio and backscatter-related and extinction-related Ångström exponents) were derived automatically using the Polly^{NET} processing chain (cf. Sect. 2.2.5). In this study, a special focus was given to the improvement of the cloud detection implemented in the processing chain, which is particularly important at Mindelo as small convective clouds are frequently occurring in the PBL especially during the night. Per default, the gradient method is applied in the current version (3.3) of the Polly^{NET} processing chain using a threshold value of 4×10^6 MHz m. As this threshold did not lead to satisfying results yet, it was decreased from 1×10^5 MHz m to 0.5×10^5 MHz m in steps of 0.1×10^5 MHz m for 19 test nights (17 Sep, 8 Oct, 12 Nov, 26 Nov 2021; 4 Feb, 27 May, 3 Jun, 1 Jul, 21 Oct, 16 Dec 2022; 24 Mar, 21 Apr, 2 Jun, 9 Jun, 16 Jun, 22 Jul, 28 Jul, 11 Aug, 25 Aug 2023). Decreasing the threshold value is equivalent with a stricter cloud screening and often leads to shorter periods of temporal averaging to derive the profiles, which might cause difficulties for a correct calibration and stable results. Optimally, the signal should be averaged over 1 h, but this study has shown that averaging periods of around 0.5 h are sufficient as well thanks to the powerful diode pumped Nd:YAG laser used in the system operated at Mindelo. However, the averaging period should not be shorter than 15 min. To find an appropriate threshold is challenging and there is no perfect solution for all analyzed nights. For now, a value of 0.7×10^5 MHz m was found as the best solution for the analyzed Fri/Sat nights and especially for the 19 test nights. However, it is a compromise between nights, when this threshold leads to a too strict cloud screening and other nights, when the derived profiles are still cloud-contaminated. In a next step, the current cloud screening has to be tested for all measurements at Mindelo beyond the Fri/Sat nights between July 2021 and August 2023 and for other locations in Polly^{NET}.

An example case which illustrates the sensitivity of the retrieval of vertical profiles on the choice of the threshold value is presented in Fig. 3.1. The figure shows a typical situation of the atmosphere above Mindelo as observed during most of the analyzed nights. Both upper panels (plots a and b) show the temporal development of the vertically-resolved calibrated attenuated backscatter coefficient at 1064 nm on 27 May 2022, 18–24 UTC. The logarithmic color scale indicates the backscatter strength. During that time, the PBL reached up to 700–800 m height. Above, a lofted aerosol layer can be identified up to a height of around 4 km. At the top of the PBL, small clouds are visible. They are represented by a very strong backscatter signal (red colors) and complete attenuation (no signal) directly above the cloud base, e.g., around 20 UTC or 22–23 UTC. In panel c, which shows the corresponding target classification according to Baars et al. (2017), water and non-typed clouds were detected for these times.

The investigation of the different threshold values was based on a visual inspection, i.e., the time-height-plot of the calibrated attenuated backscatter coefficient was used to check the derived profiles for cloud-contamination. Profiles usually were retrieved for 1 h time periods starting on full hour. As illustrated by the temporal development of the calibrated attenuated backscat-

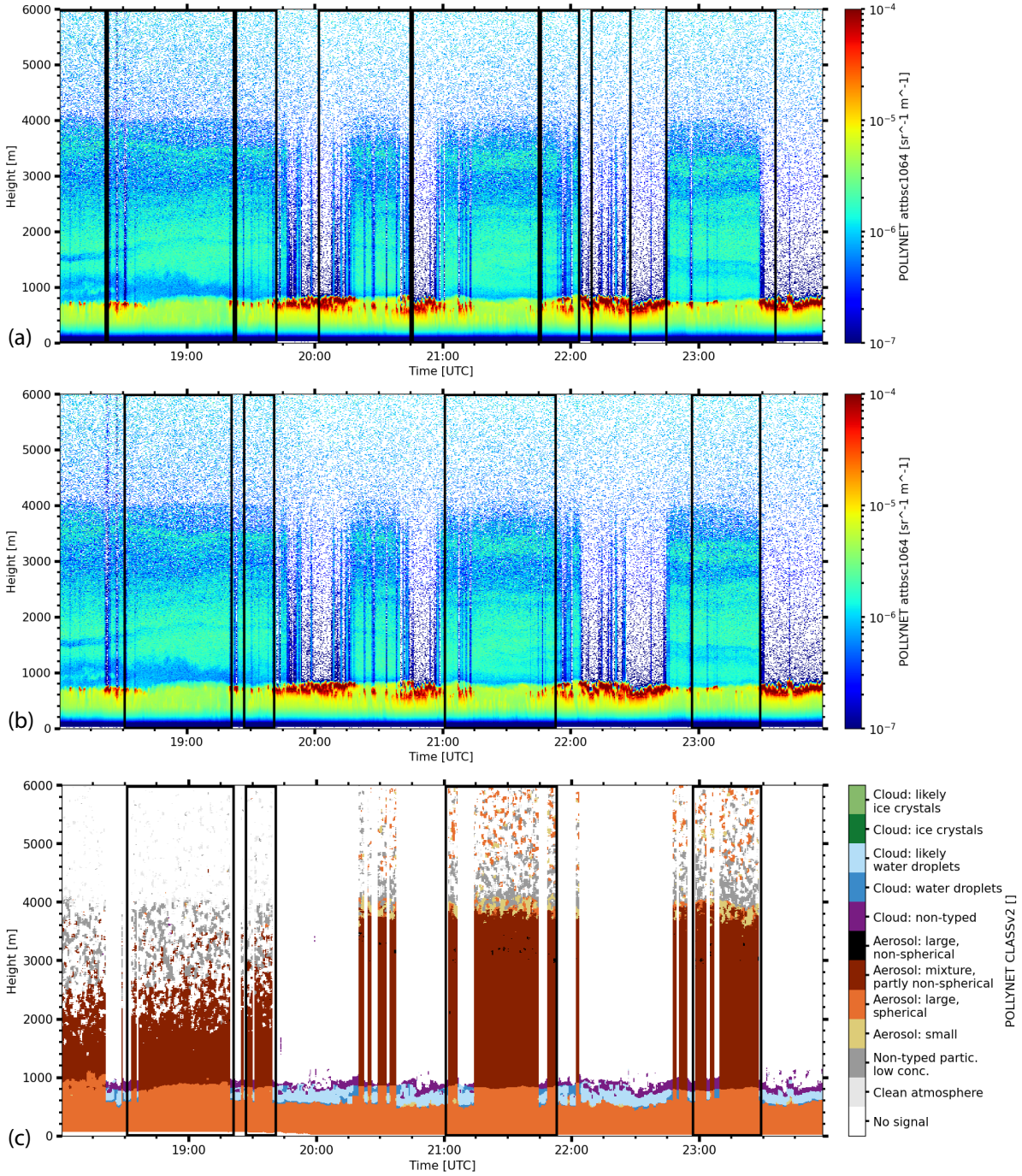

Figure 3.1: Case study for 27 May 2022, 18–24 UTC, concerning the adjustment of the cloud screening in the Polly$^{\mathrm{NET}}$ processing chain showing in (a) and (b) the height resolved temporal development of the calibrated attenuated backscatter coefficient at 1064 nm and in (c) the lidar target classification. The black rectangles indicate the time periods for which vertical profiles of the aerosol optical properties were derived automatically using a cloud screening threshold of 1×10^5 MHz m in (a) and of 0.7×10^5 MHz m in (b) and (c).

ter coefficient in Fig. 3.1, the described 1 h periods are not cloud-free. The results of a stricter cloud screening with a threshold value of 1×10^5 MHz m and the finally implemented value of

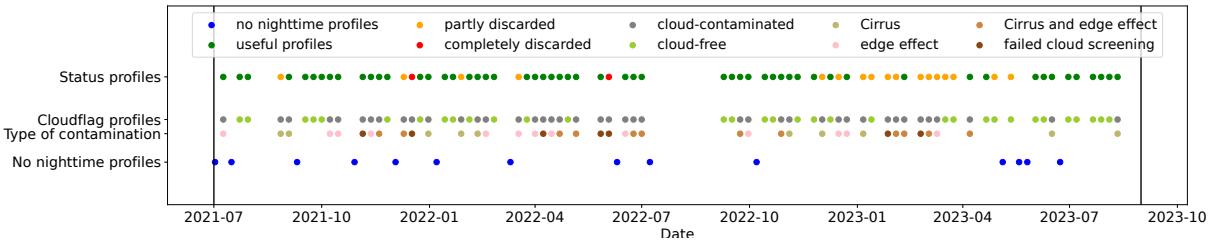

Figure 3.2: Overview of available measurements and lidar profiles at Fri/Sat nights between July 2021–August 2023 (marked by the vertical black lines), including information about the cloud-contamination of the derived profiles.

0.7×10^5 MHz m are represented by the black rectangles Figs. 3.1a and b/c, respectively. They indicate over which time periods the raw signal was averaged to obtain vertical profiles of the aerosol optical properties. For the threshold of 1×10^5 MHz m, one can clearly see that the derived profiles are strongly contaminated by clouds. This is valid especially for the profiles averaged from 20:02–20:45, 20:46–21:45 and 22:10–22:28 UTC. The reduction of the threshold value led to shorter averaging periods and fewer profiles were retrieved. Although longer cloudy periods were identified by the cloud screening, short-term clouds or the marginal periods of longer-lasting cloud occurrence are still included in the retrieved profiles, as indicated with Fig. 3.1c.

A major limitation of this gradient method is that the choice of the threshold value follows a visual inspection using the time-height-plots of the attenuated backscatter coefficients (at different wavelengths, far-field and near-field) but needs a more robust definition of clouds. Furthermore, it neglects cirrus clouds. Thus, the gradient method should be replaced with a more appropriate algorithm, e.g., using the target classification. However, the latter entails its own challenges, which need to be evaluated using the new cloud radar.

3.5 Quality control and availability of the retrieved aerosol vertical profiles

As a result of the cloud screening, the data set of 89 nights was reduced to 74 nights, as on the other nights, the algorithm did not detect any cloud-free periods that were long enough to fulfill the requirements for a stable calibration. Furthermore, one profile per night was selected to be used for the statistical analysis of the aerosol conditions in the atmosphere above Mindelo. The decision to consider only one profile per night was made to guarantee quality-assured profiles. The profiles were manually carefully checked and any badly calibrated profiles (mainly single aerosol optical properties at single wavelengths) were removed from the data set.

Figure 3.2 provides an overview of the availability of measurements and vertical profiles for the Fri/Sat nights in the period from July 2021 to August 2023. The blue markers in the lowermost row indicate the nights for which no profiles could be derived by the algorithm due to the strict cloud screening. The temporal distribution of the selected profiles is summarized in the uppermost row. The red and orange colors indicate profiles which had to be discarded due to complete cloud-contamination or from which several aerosol optical properties were discarded due to miscalibration, respectively.

For checking the cloud-contamination of the derived lidar profiles, the cloud information product obtained from the target classification v2 (cf. Sect. 2.3.4) was used. Amongst others, it provides the cloud base height, the cloud phase probability and the number of detected cloud layers. The lidar profiles were considered as cloud-contaminated (gray dots in Fig. 3.2) when at least one value for the cloud base height appeared within the corresponding averaging period,

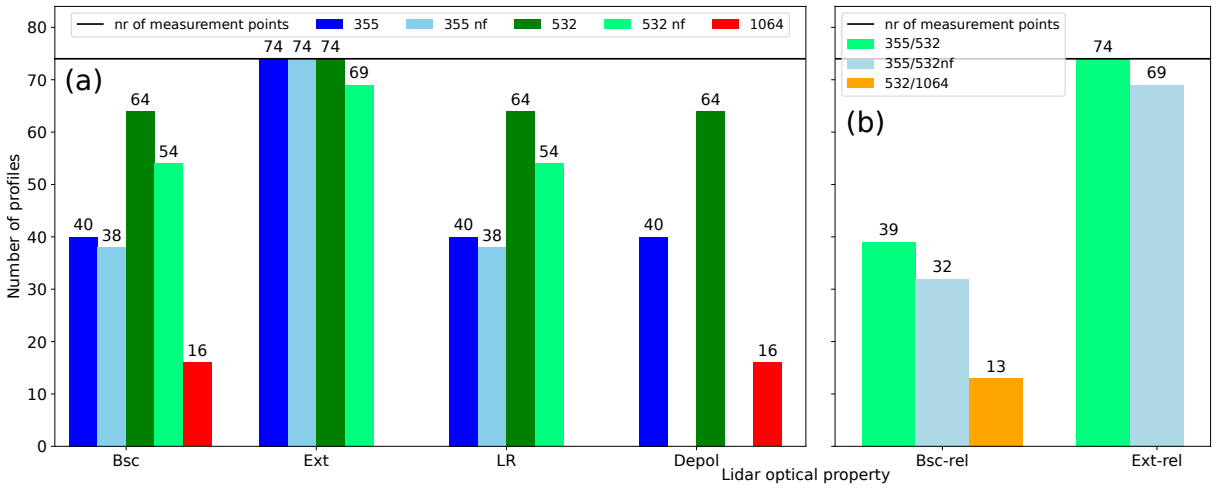

Figure 3.3: For Fri/Sat nights between July 2021–August 2023: number of available profiles of the particle backscatter (Bsc) and extinction (Ext) coefficients, the lidar ratio (LR), the particle linear depolarization ratio (Depol) and the backscatter-related (Bsc-rel) and extinction-related (Ext-rel) Ångström exponents at the corresponding wavelength. The black line indicates the total number (nr) of measurement nights, for which profiles are derived.

which was valid for around half of the profiles. In this context, the cloud-contamination was categorized based on three options: a completely failed cloud screening (dark brown dots), edge effects (pink dots), i.e., very few cloudy time bins within the first and last 10 min of the averaging period, high-level clouds above 8 km, which are not considered by the algorithm (khaki dots) and a mix of the latter two categories (light brown dots). These profiles were reviewed with special attention. High-level clouds and edge effects turned out to be negligible. Completely failed cloud screening means a permanent contamination with low-level clouds below 2 km altitude according to the target categorization v2. In most of these cases, the profiles were used anyway, if the clouds were not visible in the time-height-plot of the attenuated backscatter coefficient. Otherwise, only the PBL was neglected. Thus, 73 nights (dark green and orange dots) were included into the data set used for the statistical analysis.

However, there is a large discrepancy between the availability of aerosol optical properties at different wavelengths as presented in Fig. 3.3. These differences arise from the fact that several profiles were not derived by the Polly^{NET} processing chain or had to be discarded. As the lidar ratio, the particle linear depolarization ratio and the Ångström exponent are calculated from the particle backscatter and extinction coefficients, their availability depends on the availability of the latter ones. Generally, the particle extinction coefficient and the extinction-related Ångström exponent exist in almost all cases. This fact is valid for the far-field as well as for the near-field profiles. For the particle backscatter coefficient, far-field profiles are slightly more often available than near-field profiles. Another noticeable point is that a (useful) particle backscatter coefficient exists more often at 532 nm (73–86 % of all cases) than at 355 nm (51–54 % of all cases). In contrast, there are only very few cases, for which the particle backscatter coefficient at 1064 nm was derived (22 % of all cases). The latter point is not surprising as the calibration of the 1064 nm channel is typically more challenging than for 355 or 532 nm as explained in Sect. 2.2.5. However, these results emphasize that there are still open issues concerning the calibration, i.e., the automatic finding and selection of a reference height window for the optical profiles in the Polly^{NET} processing chain, which have to be tackled in the future. Furthermore, the presented overview shows that the number of measurements is sufficiently large to guarantee statistical significance for the following analysis of the annual cycle of aerosol concerning the

particle extinction coefficient at 355 and 532 nm as well as the particle backscatter coefficient at 532 nm but not for the particle backscatter coefficient and the particle linear depolarization ratio at 1064 nm.

3.6 Methods for the characterization of aerosol layers

3.6.1 Overview

As a basis for the statistical analysis of the aerosol optical properties, aerosol layers had to be defined. For this purpose, a visual inspection is commonly used (e.g., Hofer et al., 2020b; Heese et al., 2022). Although automatic retrievals for the detection of the PBL top height (Baars et al., 2008) or the aerosol layer top height (see Sect. 3.6.4; Hofer et al., 2020a) exist, it is still challenging to find an overall appropriate automatic algorithm, which is able to detect the lower and upper boundaries of (multiple) lofted aerosol layers. The algorithm of Hofer et al. (2020a) can be used only for the detection of the boundary of the uppermost layer and is, thus, not convenient for cases for which more than one lofted aerosol layer exists. Furthermore, it cannot detect the lower boundaries of the lofted aerosol layers. Therefore, the visual inspection, which is explained in Sect. 3.6.2, was considered to be the best approach for this study to obtain an optimal data set including as much profiles of the different aerosol optical properties as possible, while the automatized detection of the aerosol layer top height according to Hofer et al. (2020a) was used additonally for checking the consistency with the manually-defined aerosol layer top heights as presented in Sect. 3.6.4.

To use a completely automatic procedure was not convenient for this study also because of the issue that the output of the Polly$^{\mathrm{NET}}$ processing chain did not provide a homogeneous data set, whereat often several aerosol optical properties were not derived at all possible wavelengths (cf. Fig. 3.3). For instance, the algorithm of Hofer et al. (2020a) is based on the particle backscatter coefficient at 532 nm. When the particle backscatter coefficient is not available at this wavelength or at any wavelength no aerosol layer top height can be derived. Thus, for the further calculations of, e.g., layer mean aerosol optical properties, only the manually-defined layer top heights were considered because the aim was not to discard too many cases because of the missing particle backscatter coefficient. Furthermore, a mixing of two different methods for the detection of the layer boundaries should be avoided for reasons of consistency.

3.6.2 Definition of the aerosol layers by visual inspection

The procedure of the visual inspection to obtain the boundaries of aerosol layers is described in the following example for the profiles derived on 1 October 2021, 19:56–20:56 UTC. Figure 3.4a shows vertical profiles of the particle backscatter and extinction coefficients, the lidar ratio, the Ångström exponent and the particle linear depolarization ratio as it is the typical output of the Polly$^{\mathrm{NET}}$ processing chain and had to be used for the further post-processing. The standardized vertical smoothing is 742.5 m for the far-field and 382.5 m for the near-field measurements. In this case, all aerosol optical properties are available at all wavelengths except the particle backscatter coefficient and the particle linear depolarization ratio at 1064 nm. As there is a lot of noise, especially in the lidar ratio, the extinction-related Ångström exponent and the near-field measurements, a first step was to cut the profiles above the heights, where the noise starts and, in case of the extinction-related properties, below the heights of complete overlap. The latter are around 800 m for the far-field and around 400 m for the near-field measurements. In addition, the lowermost 100 m of the backscatter-related properties and the particle linear depolarization ratio were cut to exclude ultra-near-range effects.

Figure 3.4b shows the resulting profiles, from which at first the PBL top height was derived

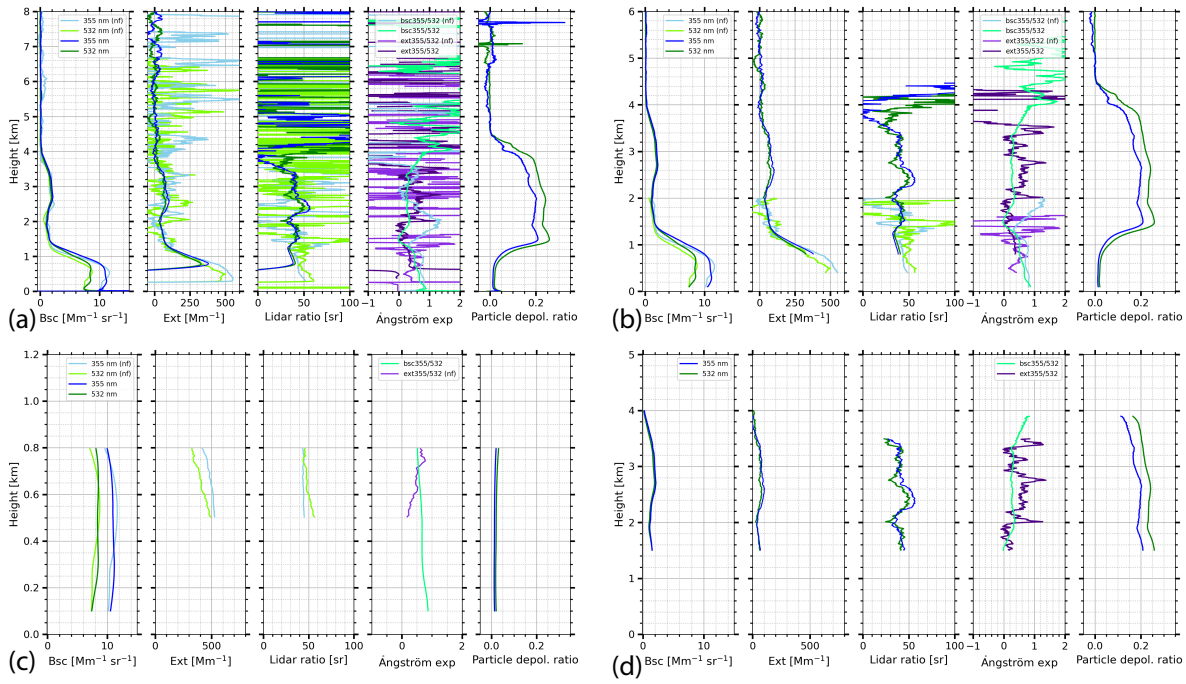

Figure 3.4: Case study for 1 October 2021, 19:65–20:56 UTC: Vertical profiles of the lidar-derived aerosol optical properties (from the left to the right in each subplot: particle backscatter and extinction coefficients, lidar ratio, backscatter- and extinction-related Ångström exponents and particle linear depolarization ratio) (a) as obtained from the Polly$^{\mathrm{NET}}$ processing chain, (b) after cutting of noise and overlap effects and (c) and (d) for the defined PBL and lofted aerosol layer, respectively. Note that the height scale is different in each plot.

using the near-field profiles of the particle backscatter coefficient. Generally, the PBL detection is challenging and strongly depends on the definition of the PBL (Stull, 2012; Belegante et al., 2014). Due to the vertical smoothing of the existing output from the Polly$^{\mathrm{NET}}$ processing chain, no sharp boundary between the PBL and the free troposphere is visible but an expanded transition zone reaching from the maximum of the backscatter coefficient at around 500 m height to the next point of inflection at around 1200 m height. The PBL top was estimated to be in the middle of this transition zone with preference to its lower half. In this example, it was set to 800 m. Generally, a vertical accuracy of 100 m could be ensured within this visual inspection, i.e., the uncertainty of the derived heights is ±50 m.

For the detection of the upper and lower boundary of the lofted aerosol layer, the far-field profiles of mainly the particle backscatter coefficient were used in combination with the particle linear depolarization ratio. Furthermore, the backscatter-related Ångström exponent could be an indicator for the layer boundaries as it should remain nearly constant within a homogeneous aerosol layer, similarly to the particle linear depolarization ratio. For the shown example, an agreement of the local maximum and minimum of the particle linear depolarization ratio and the backscatter-related Ångström exponent, respectively, and the point of inflection in the profile of the particle backscatter coefficient suggested the lower boundary of the lofted aerosol layer to be at around 1500 m. While the particle backscatter coefficient indicated an upper boundary at around 4000 m, the particle linear depolarization ratio dropped to almost zero at 4400 m height. A similar behavior was often seen in the analyzed cases and a more restrictive aerosol layer top height detection based on the backscatter coefficient rather than on the depolarization ratio was preferred because of the goal to characterize the intensive optical properties representative for

each layer. Furthermore, remaining noise in the profiles of the lidar ratio and the Ångström exponent was cut. In addition, large gradients in the profiles of the intensive properties were excluded. Therefore, the different aerosol optical properties sometimes were cut at different altitudes with the aim of including as much data as possible and avoiding the production of a systematic bias. If indicated by noticeable vertical differences in the aerosol optical properties, the lofted aerosol layer was split into multiple sublayers. The resulting profiles for the PBL and the lofted aerosol layer shown in Figs. 3.4c and d, respectively, were used for the further calculations, which are explained in Sect. 3.6.3.

A major challenge in this visual inspection of the aerosol layer boundaries was the handling of noise and the decision which parts of the vertical profiles to include in the calculation of layer mean values. Furthermore, in this study, especially low PBL heights (<800 m) in combination with the overlap issue have raised the question of how representative it is to average over a layer of 100–200 m thickness when only noise exists above. Generally, an agreement of the layer mean values obtained from the far-field and from the near-field profiles was considered as an indicator for representativeness in these cases. However, the visual inspection of the boundaries of the aerosol layers needs to be automatized and requires more robust methods as it is too time consuming and includes a rather subjective component. The use of tools based on artificial intelligence will be for sure subject of future research in this field.

3.6.3 Calculation of layer-resolved aerosol optical and microphysical properties

For the further calculations of the layer-resolved aerosol optical properties, near-field measurements were used for the PBL, while the far-field measurements were used for the lofted aerosol layers. However, for the PBL, far-field measurements had to be used as well, namely in case of the particle backscatter coefficient at 1064 nm, the corresponding backscatter-related Ångström exponent and the particle linear depolarization ratio at all three wavelengths because no near-field measurements are available for these properties. In the following, layer mean values were calculated for the intensive optical properties, while for the extensive optical properties a vertical integration was applied resulting in an integrated particle backscatter coefficient and the AOD. For this purpose, the particle backscatter and extinction coefficients were interpolated to the ground in the PBL, i.e., the lowermost values shown in Fig. 3.4c were assumed to be constant down to the ground. This assumption can be made as the PBL provides well-mixed aerosol conditions (Michailidis et al., 2023). Another important point had to be considered for the PBL, which is the different smoothing of the near-field and far-field measurements. This inconsistency may lead to a slight overestimation of the far-field integrated particle backscatter coefficient and the AOD as the corresponding profiles start to decrease at higher altitudes than for the near-field profiles. Similarly, the transition zone in the profile of the particle linear depolarization ratio starts at higher altitudes than it would have been observed for a lower vertical smoothing. Both described effects are worth to be mentioned and should be improved for future studies but can be neglected for this study as the far-field intensive optical properties usually were cut at an altitude below which they should be nearly constant anyway.

In addition to the analysis of the aerosol optical properties shown in Fig. 3.4, the integrated dust and non-dust particle backscatter coefficients as well as the dust fraction were calculated using the 1-step POLIPHON output of the Polly^{NET} processing chain. For the dust fraction, deriving the vertical profile of the dust fraction first and determining its layer mean values afterwards was considered to be the more precise method rather than dividing the integrated dust backscatter by the integrated total particle backscatter coefficient, which led to slightly different results. Concerning the uncertainty of the layer mean and integrated optical properties, it is worth to mention that for the intensive optical properties and the dust fraction the layer mean

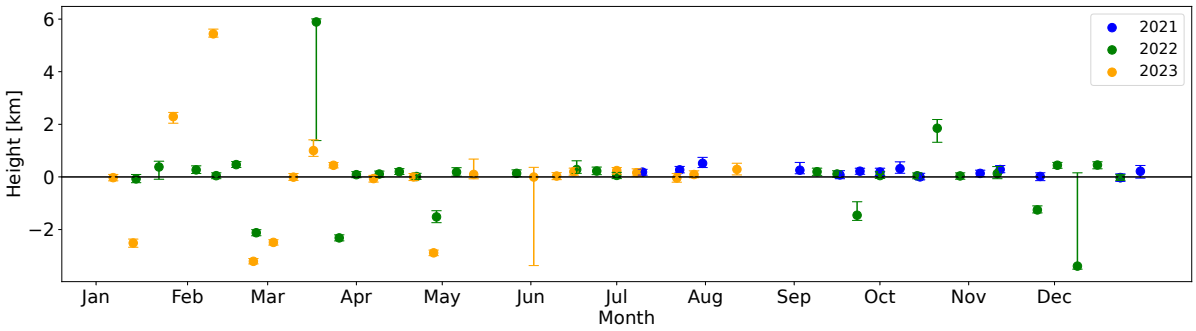

Figure 3.5: Deviation of the manually-defined layer top height from the automatically retrieved one obtained from the Fri/Sat cases. The error bars represent the sum of the uncertainty of the automatically-retrieved and manually-defined aerosol layer top heights.

values of the errors described in Sect. 2.2.4 or derived via the Gaussian error propagation, respectively, were calculated. For the integrated optical properties, the given errors were used and the Gaussian error propagation was applied to the formula which was used for the integration. In case of the particle backscatter coefficient, the resulting error is equivalent to a relative error of 15 % of the integrated property.

3.6.4 Automatized detection of the aerosol layer top height

In the algorithm of Hofer et al. (2020a), the layer top of the uppermost aerosol layer is set at the height where the far-field particle backscatter coefficient at 532 nm falls below a certain threshold, i.e., 0.1 $\mathrm{Mm^{-1}sr^{-1}}$ for the first time. For the estimation of the uncertainty of the derived height, the algorithm was applied to a slightly varied threshold of the particle backscatter coefficient (±15 %, which is in agreement with the uncertainty of the particle backscatter coefficient) and the differences between these heights and the previously derived layer top height were calculated.

As both methods, the visual inspection and the algorithm of Hofer et al. (2020a), strongly differ in their working principle, differences in the results are expected. However, the results of the algorithm of Hofer et al. (2020a) generally agree with the results of the visual inspection as illustrated in Fig. 3.5 showing the automatically retrieved layer top height minus the value from the visual inspection. The agreement is better from April to December but the automatic algorithm often slightly overestimates the layer top height with around 200 m. In contrast, the differences between both methods are larger from January to March. The large underestimation of the layer top height of around 2 km can be explained by the generally low signal in higher altitudes during northern hemispheric winter due to the comparably small aerosol load in the lofted layer or between the PBL and the lofted layer. Thus, the signal often had decreased below the threshold some few hundred meters above the PBL before it increased again due to the presence of a lofted aerosol layer, which was neglected by the algorithm of Hofer et al. (2020a). Instead, in the visual inspection, the lofted layer was considered, which led to large differences in the determined layer top heights. Another reason for the underestimation of the layer top height by the automatic retrieval was the presence of Cirrus clouds, which sometimes caused the miscalibration of the particle backscatter coefficient. In these cases, a systematic shift to negative values was observed for the backscatter coefficient. As a consequence, it dropped below the threshold already at low altitudes. Cases with miscalibrated profiles were discarded for the further analysis but are still included in this comparison emphasizing the necessity of cross checking the automatical retrievals and the output of the Polly$^{\mathrm{NET}}$ processing chain. In the cases, when the layer top height was overestimated (e.g., 18 Mar 2022, 10 Feb 2023), the

backscatter coefficient showed comparably large values slightly above the threshold value up to altitudes of around 10 km, maybe due to miscalibration (cirrus cloud on 10 Feb 2022) or noise. Furthermore, the large error bars of a range up to 4 km range arise from the effects described before. For instance, on 9 December 2022, the PBL top was detected as layer top height by the algorithm of Hofer et al. (2020a) although a lofted layer was present. In analogy, on 2 June 2023, the algorithm detected a lofted layer, which could not be identified by visual inspection. Furthermore, a larger difference between the automatically-derived and manually-defined layer top height occurred when only the PBL was present because of the different working principle of both methods. While in the algorithm of Hofer et al. (2020a), the layer top height is set to heights where the particle backscatter coefficient has already reached low values, i.e., below the threshold, the PBL top is set in the middle of the transition zone.

3.6.5 Analysis of the cloud occurrence

Although the main focus of this work is on the evaluation of the aerosol conditions over Mindelo, the occurrence of clouds, especially in the PBL, has turned out to be a fundamental issue with large impact on the quality of the lidar-derived vertical profiles of the aerosol optical properties. For this reason, a statistical analysis of the cloud occurrence is presented in addition to the statistical analysis of the layer mean and integrated aerosol optical properties. Therefore, the complete two-year data set from July 2021 to August 2023 was considered including daytime as well as nighttime measurements. Additionally, results are shown for the Fri/Sat nights only (defined from sunset to sunrise).

The analysis was based on the cloud base heights obtained from the cloud information output of the Polly$^{\mathrm{NET}}$ processing chain, which uses the target categorization v2 described in Sect. 2.3.4. All time bins of the 30 s resolved temporal measurement for which at least one cloud base height was detected were flagged as cloudy times. This flagging was applied generally for all cloud base independent of their height level as well as for the different cloud levels based on the definition of the World Meteorological Organization (WMO cloud definitions, 2024), i.e., low-level clouds (cloud base height $\leq$ 2 km), mid-level clouds (cloud base height $>$ 2 km and $\leq$ 8 km) and high-level clouds (cloud base height $>$ 8 km). A day (or a night, respectively) was flagged as cloudy if any cloudy time bin was detected during that day or night, respectively. This procedure was repeated for the single cloud level categories separately. For time bins for which low-level clouds were detected, mid-level and high-level clouds were neglected even if cloud base heights for these height levels are included in the cloud information output. Similarly, high-level clouds were only considered for time bins without low-level and mid-level clouds. Due to the strong attenuation of the lidar signal by liquid water clouds, the results for cloud levels above are not trustworthy. An example illustrating this aspect is given in Fig. 3.6a showing the target classification v2 for 15 September 2022. During the displayed time from 12–24 UTC, a layer of liquid water droplets was almost permanently present at around 1 km height. Above, many pixels were obviously misclassified as likely water droplets or non-typed clouds and cloud bases heights in the mid-level were derived. Considering this example, it is clear that they are not correct and have to be neglected. The strong attenuation of the lidar signal by clouds so that higher-altitude clouds may be not detected when low clouds are present is one major limitation in this analysis. Generally, noise within the target categorization needs to be considered better in future studies, i.e., single cloudy pixels within a completely cloud-free surrounding may arose from misclassification and should be screened out.

Another problem can arise if the cloud base height of the low-level clouds persisting at around 2 km alternates around the threshold value for classifying the cloud levels. This effect would lead to a splitting of low-level clouds into different categories so that the occurrence of low-level clouds is underestimated, while the occurrence of mid-level clouds is overestimated. An

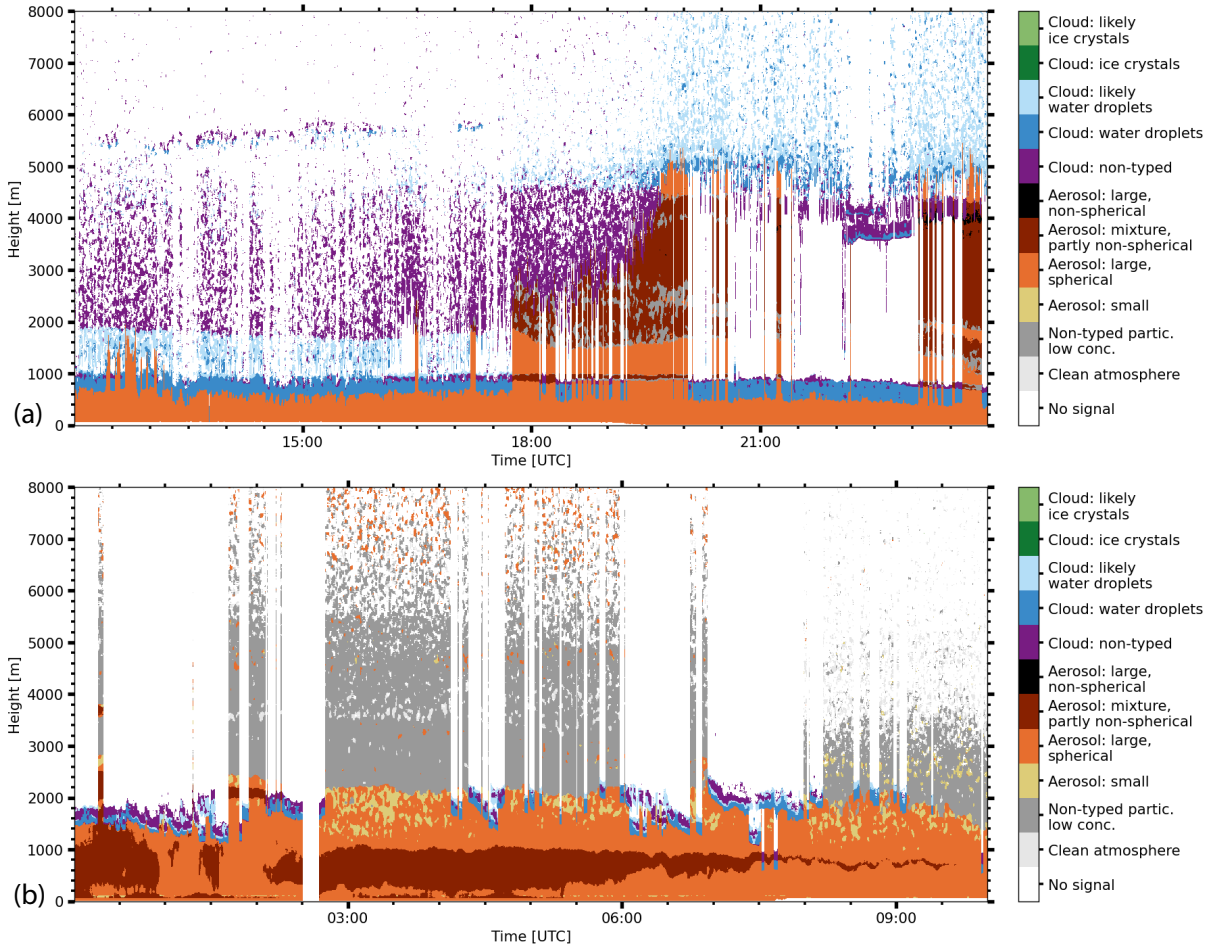

Figure 3.6: Lidar target classification (a) on 15 September 2022, 12–24 UTC, and (b) on 24 September 2022, 0–10 UTC.

example case representing this issue is shown in the target classification v2 for 24 September 2022 in Fig. 3.6b. In this case, the cloud base height was usually slightly below 2 km but between 5:45–9 UTC, cloud base heights slightly above 2 km were detected. Thus, for most time bins the observed clouds were flagged as low-level clouds but for some time bins they were flagged as mid-level clouds only because of the choice of the threshold value of 2 km. For future studies, the representativeness of the chosen threshold value should be discussed. However, for this thesis it is kept because the cases with low-level clouds occurring in altitudes around 2 km were very rare. Typically, these low cloud layers occurred at heights significantly lower than 2 km. Thus, the overestimation of mid-level clouds due to the described effect is assumed to be negligibly small.

3.6.6 Air mass source attribution

To attribute the observed aerosol particles to their emission sources, backward simulations with the Hybrid Single-Particle Lagrangian Integrated Trajectory model (HYSPLIT, 2024; Stein et al., 2015) were calculated. The model is publicly available via the web-based Real-Time Environmental Applications and Display System (READY; Rolph et al., 2017). The fundamental principle of HYSPLIT is based on a hybrid approach of a combined Lagrangian-Eulerian methodology. Single trajectories can be calculated as well as ensemble trajectories. Trajectory ensembles assist in accounting for the uncertainties in trajectory calculations caused by differences in the initial

conditions and parameterizations, such as offsets in the meteorological data or atmospheric turbulence.

In combination with HYSPLIT backward trajectories, the fire spot analysis of the Fire Information for Resource Managment System (FIRMS; Davies et al., 2009) was used in this study. This system provides publicly available daily global fire information. The fire product is obtained from the Moderate-resolution Imaging Spectroradiometer (MODIS; Xiong & Barnes, 2006) onboard the NASA satellites Terra and Aqua. MODIS uses the strong emission of mid-infrared radiation from fires to flag pixels if they contain one or more actively buring fires.

Chapter 4

Results and discussion

4.1 Two years of lidar observations—an overview

Two years of continuous lidar measurements have been performed at Mindelo and were analyzed in the framework of this thesis. An overview of the complete measurement period in terms of (a) the vertically-resolved temporal development of the calibrated attenuated backscatter coefficient at 1064 nm and (b) the volume depolarization ratio at 532 nm between 1 July 2021 and 31 August 2023 is provided in Fig. 4.1. Data gaps within this two-year period were rare and rather short, except two longer phases, one in May 2022 and one from the end of July to the beginning of September 2022. Two further data gaps covering a time span of around one week each can be identified in November and December 2022. The stable availability of lidar measurements provides a good basis for studying the annual cycle of the aerosol in the atmosphere above Mindelo. This cycle is clearly indicated by the temporal development of the calibrated attenuated backscatter coefficient and the volume depolarization ratio. Red colors in the lowermost 1000 m of the upper plot represent strong backscattering in the PBL showing only small annual variability in intensity and extent. During all the time, clouds could be identified at the top of the PBL, represented by the white color, i.e., very strong backscattering. The volume depolarization ratio in the PBL usually was low (blue colors in the lowermost 1000 m of Fig. 4.1b). On only few days, it exceeded 0.1, e.g., in February 2022. The observed pattern indicate that mainly spherical particles were present in the PBL. Above the PBL, a lofted aerosol layer was visible most of the time. Its top height strongly varied with the annual cycle. Beginning at around 6 km height on 1 July 2021, it decreased to around 3 km height in the time of November 2021–February 2022. Afterwards, an increase in the aerosol layer top reaching a maximum of around 6 km height before the data gap in July/August 2022 could be seen. After that time, a similar pattern as described for the previous period was observed. The backscatter strength in the lofted aerosol layer was rather moderate while the volume depolarization ratio varied from values up to 0.3 during the months of northern hemispheric summer and fall (June–September) to values around 0.1 or even less during the months of northern hemispheric winter and spring (November–March). The larger depolarization during the summer months indicate the presence of non-spherical particles, i.e., desert dust during that time.

As the figure clearly illustrates, a measurement period capturing two complete annual cycles of the atmospheric aerosol conditions was the basis for this study. Furthermore, a period representing a very rare deviation from the typical atmospheric situation is included, namely the time interval from September to December 2021, when volcanic sulfate originating from the eruption of Cumbre Vieja at La Palma, Canary Islands, was observed in the PBL above Mindelo. Based on a case study, this event was described in Gebauer et al. (2024). A detailed investigation of the atmospheric situation above Mindelo during the complete two years is presented in the following

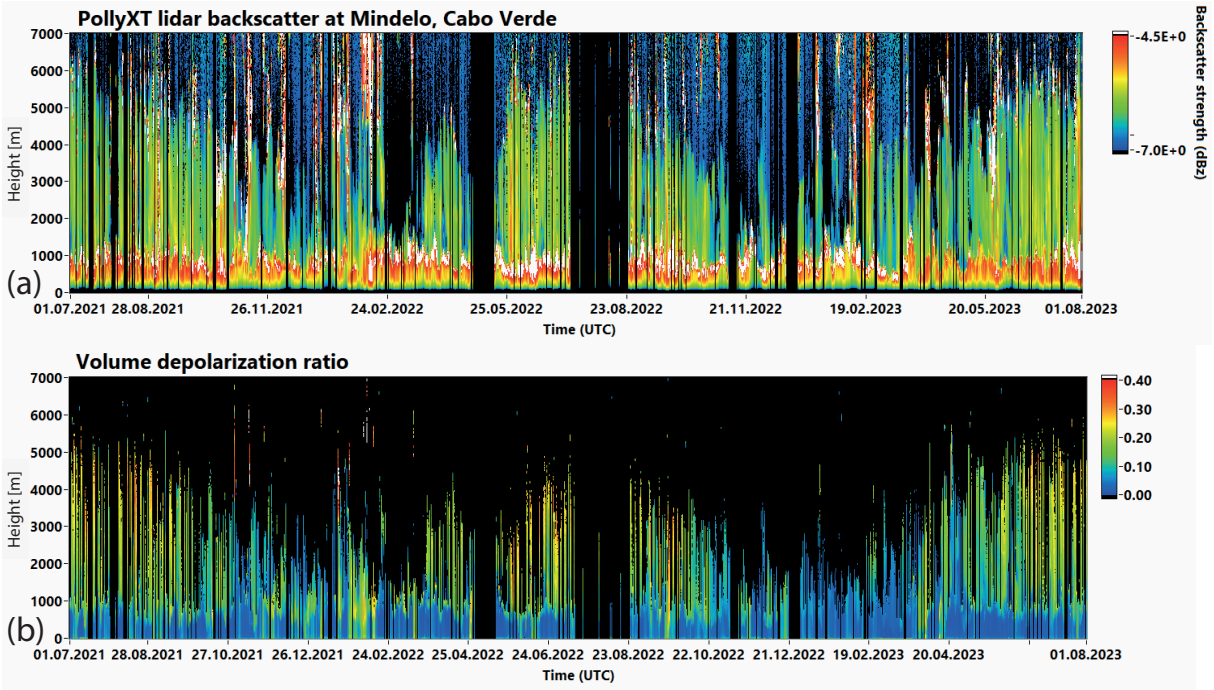

Figure 4.1: Temporal development of the height-resolved (a) calibrated attenuated backscatter coefficient at 1064 nm and (b) the volume depolarization ratio at 532 nm measured with Polly^{XT} at Mindelo between 1 July 2021 and 31 August 2023.

sections, starting with a statistical analysis of the cloud occurrence in Sect. 4.2. Next, two case studies are described in Sect. 4.3 contrasting a measurement originating from the mixing season with a typical example from the dust season. Finally, an in-depth analysis of the annual cycle by means of the aerosol optical properties obtained from the Fri/Sat nights data set is presented in Sect. 4.4.

4.2 Cloud occurrence

First, the results of the cloud occurrence for the complete two-year data set are described. They were obtained following the methodology described in Sect. 3.6.5. Generally speaking, 43 % of all time bins for which the target categorization is available were flagged as cloudy. A more detailed overview of the cloud occurrence is given in Fig. 4.2, showing a histogram of cloudy days including (a) all days within these two years and (b) only the Fri/Sat nights, defined from sunset to sunrise. For the entire period, 680 days could be included in this evaluation. On 663 days, i.e., on around 98 % of the days, any cloud was detected by the target categorization algorithm, represented by the black bar. The remaining bars indicate the number of days for which at least one cloud layer (low-, mid- or high-level clouds) or multiple cloud layers in general independent from their height level (labelled as "generally" in Fig. 4.2) were detected. Absolute numbers are given in green. As a subset of these categories, the orange bars show the number of days on which clouds of only one cloud level occurred. Except for the black bar, which is related to the complete number of measurement days, the bars indicate the relative occurrence of a certain cloud type with regard to the cloudy days, i.e., 663 days.

Figure 4.2a reveals significant differences between the number of days on which only one cloud type occurred and days with clouds at multiple height levels. While days with clouds of only one height level were very rare with only 0.3–8 %, most of the time, i.e., in 91 % of all cloudy days,

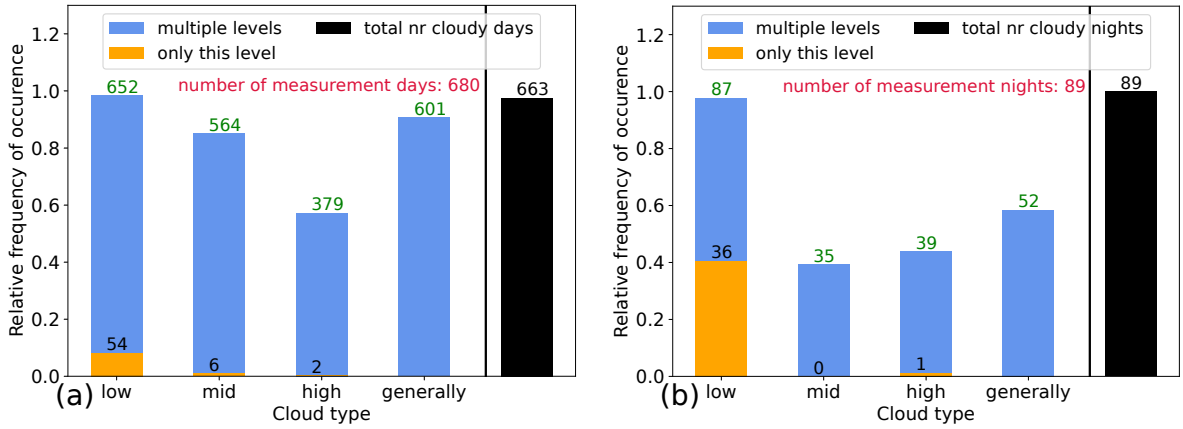

Figure 4.2: Relative frequency of cloud occurrence at Mindelo, July 2021–August 2023, for (a) all days and (b) the Fri/Sat nights: Number of cloudy days (nights, respectively) related to the number of measurement days (black bar) and (in green) number of days/nights with low-, mid- or high-level clouds and mixtures of these types (labelled as "generally") relative to the number of cloudy days/nights. Number of days/nights with only one cloud level (orange bars, black numbers).

mixtures were observed. Furthermore, there were differences between the varying cloud levels. Low-level clouds were more common than mid-level clouds followed by high-level clouds. The observed pattern may be influenced by the measurement principle of the aerosol lidar. As the lidar signal is strongly attenuated by clouds, higher clouds often cannot be detected while lower clouds are present. Thus, the mid-level and even more the high-level clouds may be underrepresented in this study, especially as there was a frequent occurrence of low-level clouds. The great importance of low-level clouds for the location at Mindelo can be highlighted with this study, showing that on 98 % of the cloudy days and on 96 % of all measurement days low-level clouds were present at least once during the day.

In addition to the general overview, Fig. 4.3 provides a monthly-resolved analysis. Again, the relative numbers of the generally cloudy days refer to the number of all measurement days, while the relative frequency of occurrence in the height-resolved analysis refers to the cloudy days only. The data can be regarded as sufficiently large for statistical significance although there is some variation in the number of measurement days between the single months. Mostly, around 50–60 measurement days per month could be analyzed. Even for the months with data gaps (May and August), at least 47 days were included. The number of measurement days for July is much higher than for the other months because it includes three years (2021, 2022 and 2023), while for the rest only two years were considered.

Overall, the general cloud occurrence did not exhibit an annual cycle. For all months, almost all measurement days were flagged as cloudy days. Only 17 completely cloud-free days existed within these two years and were distributed among July, August, September, November, January and February. A similar pattern was observed for the different cloud-levels. Only the occurrence of mid-level clouds showed a slight monthly variation. The relative number of days having mid-level clouds while no low-level clouds were present was larger from May to October. This temporal development can be explained with this time span covering the main dust season. As described before and indicated by Fig. 4.1, during the northern hemispheric summer, geometrically thick lofted layers of Saharan dust particles occur over Mindelo reaching altitudes of up to 6 km. With mineral dust particles acting as effective INPs, favorable conditions for

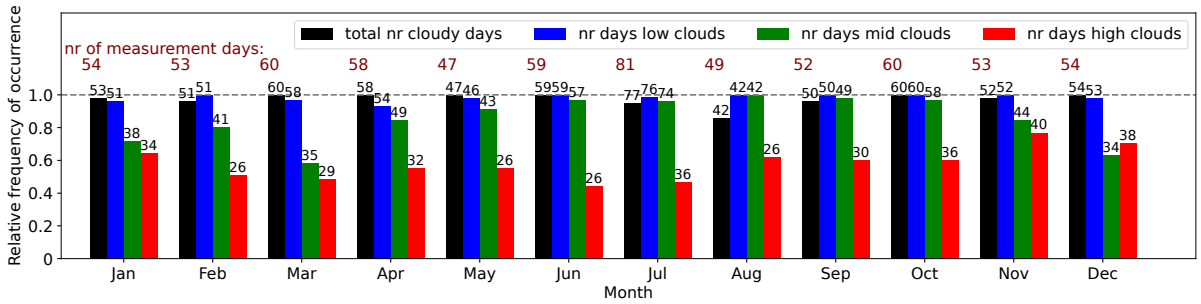

Figure 4.3: For July 2021–August 2023: frequency of occurrence of cloudy days referred to all measurement days and of days with at least one of the cloud types referred to the number of cloudy days. Absolute numbers are given additionally.

the formation of mid-level clouds, at the top of the dust layer, seemed to be provided. Instead, the proportion of high-level clouds is slightly larger in the fall and winter seasons (November–January) compared to the rest of the year.

To get an impression of the representativeness of the Fri/Sat nights in terms of cloud occurrence, another histogram is provided in Fig. 4.2b, similarly to Fig. 4.2a. The patterns of both histograms generally agree. In all of the 89 measurement nights, clouds were detected. Due to the reduced number of measurement nights compared to the full data set, no nights with only mid-level and only one night with only high-level clouds were detected. Another reason for this observation could be the higher percentage of nights with only low-level clouds, which is around 29 % compared with 8 % for the full data set. In analogy to this finding, the proportion of nights with mixtures is reduced to 58 % compared with 91 % in the complete two years. Generally, during the Fri/Sat nights, the relative frequency of occurrence of low-level clouds is much higher, almost more than double than that of mid- and high-level clouds. These findings might indicate a larger importance of low-level clouds during nighttime compared with the other cloud levels. A possible reason could be that during nighttime longer time periods may be covered by low-level clouds than during daytime. Thus, the remaining cloud levels will be underrepresented more strongly.

To answer this question, a more detailed analysis of the cloud occurrence beyond the flagging of complete nights but also considering the amount of time covered by clouds, is provided with Fig. 4.4. It shows the relative cloudy time per night, i.e., the ratio of cloudy time bins to all time bins having the target categorization, as gray bars. Furthermore, the relative occurrence time of at least low-, mid- or high-level clouds referred to the cloudy time is added in colored triangles. During the analyzed period, there was a large variation of general cloud occurrence. Completely cloudy nights (cloudy time >95 %) were observed (19 Nov 2021, 7 Jan 2022, 28 Jan 2022, 10 Jun 2022, 8 Jul 2022, 7 Oct 2022, 3 Mar 2023, 7 Apr 2023 – please note that the Friday dates are given) as well as almost cloud-free ones (cloudy time < 5 %; 14 Jan 2022, 14 Oct 2022). Until March 2022, more nights with a relative cloud occurrence of < 50 % and only few nights with > 70 % existed but no nights with a relative cloudy time in between. Besides that, no general trend was observable, especially after March 2022. A completely different pattern can be observed if the different cloud levels are considered. During most of the nights, when clouds were detected, low-level clouds were present for almost all the time. Instead, mid-level and high-level clouds were usually completely absent or not detectable due to the permanent occurrence of low-level clouds. These findings confirm the hypothesis that the reduction of nights with other cloud-levels than low-level clouds and/or nights with mixtures as discussed in Fig. 4.2b was caused by an underestimation of higher clouds. However, no annual cycle could be identified, for the Fri/Sat nights even less than for the monthly resolved analysis of the entire two years. Anyway, the importance

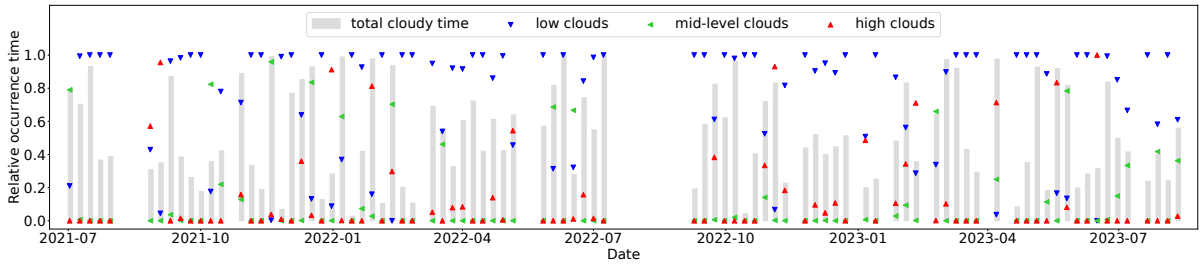

Figure 4.4: For Friday nights (July 2021–August 2023): relative cloudy time per night (gray bars) and relative time for low-, mid- and high-level clouds related to cloudy time (colored triangles).

of low-level clouds for the measurement site at Mindelo was shown. Its higher frequency of occurrence for the Fri/Sat cases may be explained by the fact that only nighttime measurements were considered and emphasizes the importance of low-level clouds especially during nighttime and especially for the analyzed sub data set.

4.3 Case studies of the different seasons

A first seasonal comparison of the aerosol conditions over Mindelo is presented in a case study analysis contrasting a measurement obtained during the dust season with one example from the mixing season. Therefore, two cases were selected from the Fri/Sat nights data set and analyzed in detail – 26 November 2021 and 4 August 2023. These examples were chosen to represent the common aerosol conditions during both seasonal regimes. However, for the mixing season, no typical situation exists as the variation in the occurrence and structure of aerosol layers was large. This statement is in agreement with the findings from SAMUM–2a, showing complex aerosol structures and aerosol mixtures during the mixing regime. Thus, the chosen example represents a common situation but it is not the only situation that was observed during northern hemispheric fall and winter. Instead, during the dust regime, most of the cases, from which this example was selected, were quite similar.

4.3.1 General overview

The corresponding vertically-resolved temporal development of the calibrated attenuated backscatter coefficient at 1064 nm and the volume depolarization ratio at 532 nm are shown in Fig. 4.5 for both cases. During both nights, a similar vertical aerosol layering consisting of the PBL and a lofted layer of aerosol was present. However, the extent of the PBL was slightly larger at the beginning of the displayed time period for 4 August (up to 1 km height at 18 UTC slightly decreasing to 0.7 km height at 24 UTC) than on 26 November (PBL top all the time around 0.6–0.7 km height). The lofted layer reached up to 3 km height on 26 November, 18 UTC, and expanded up to 3.4 km height at 24 UTC. On 4 August, aerosol particles were present up to more than 5 km height. While on 26 November at some times, small clouds could be identified in the PBL (red spots in Fig. 4.5a above which the signal suddenly strongly decreases), the period from 18–24 UTC on 4 August was completely cloud-free. Another difference between both cases is that on 26 November, the PBL transited directly to the lofted layer of aerosol while on 4 August, the PBL and the lofted layer were clearly separated by a zone of relatively low backscatter signal. Furthermore, the volume depolarization ratio (Figs. 4.5c and d) strongly differed between both cases. Generally, it was much lower on 26 November than on 4 August. This contrast is valid for the PBL, where the depolarization ratio was almost zero on 26 November but slightly higher with up to 0.1 on 4 August, and especially for the lofted layer. On 26 November, the

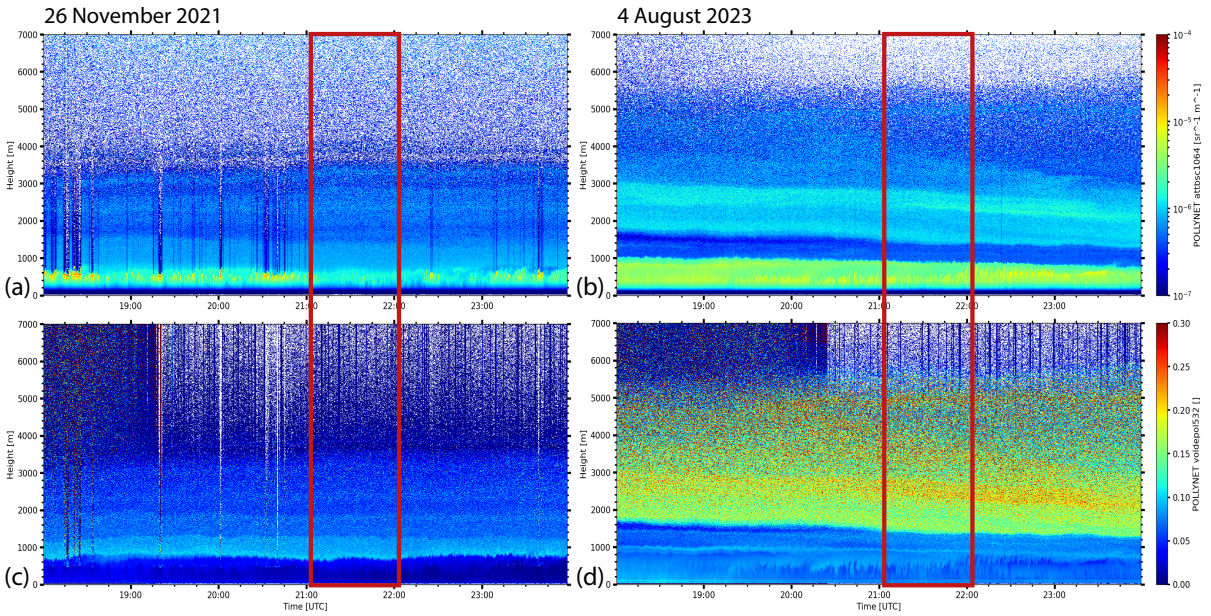

Figure 4.5: Vertically-resolved temporal development of the attenuated calibrated backscatter coefficient at 1064 nm and the volume depolarization ratio at 532 nm between 18–24 UTC on 26 November 2021 (left panels) and 4 August 2023 (right panels). The time periods for which vertical profiles of the aerosol optical properties were derived are indicated by the red rectangles.

volume depolarization ratio hardly exceeded 0.1 in the lofted layer and notably decreased with increasing altitude, whereas on 4 August, high values from 0.15 to more than 0.2 were observed among the lofted aerosol layer. The described findings indicate that on 4 August non-spherical particles were present in the lofted aerosol layer and that the PBL was not completely free of non-spherical particles as it seemed to be the case on 26 November. However, non-spherical particles in the lofted layer were also present on 26 November.

As the calibrated attenuated backscatter coefficient shown in Figs. 4.5a and b is not corrected for atmospheric attenuation and does not allow a quantitative comparison of the backscatter strength between both cases, vertical profiles of the aerosol optical properties were derived. Therefore, the lidar signal was averaged over a 1 h period each: 21:03–22:03 UTC on 26 November 2021 and 21:02–22:02 UTC on 4 August 2023. In both cases, the profiles are cloud-free according to the target classification v2. Selecting these examples for the case study, special attention was paid to provide the nearly complete set of aerosol optical properties at all wavelengths. For the case of the mixing season, only measurements from the 1064 nm channel are missing, while the example for the dust regime captures one of the rare retrievals having the particle backscatter coefficient and the particle linear depolarization ratio at 1064 nm additionally to the wavelengths of 355 and 532 nm. The vertical profiles are shown in Fig. 4.6. On 4 August, the lowermost 200 m of the near-field and the lowermost 400 m of the far-field backscatter-related properties, respectivley, had to be neglected due to a technichal artefact at these heights. The same artefact was observed in multiple other cases.

4.3.2 Definition of the aerosol layer heights

The boundaries of the aerosol layers were defined by visual inspection and the automatic retrieval of the aerosol layer top height was applied (both as described in Sects. 3.6.2 and 3.6.4). In both cases, the PBL top was defined to be at around 0.7 km. On 4 August, the near-field particle

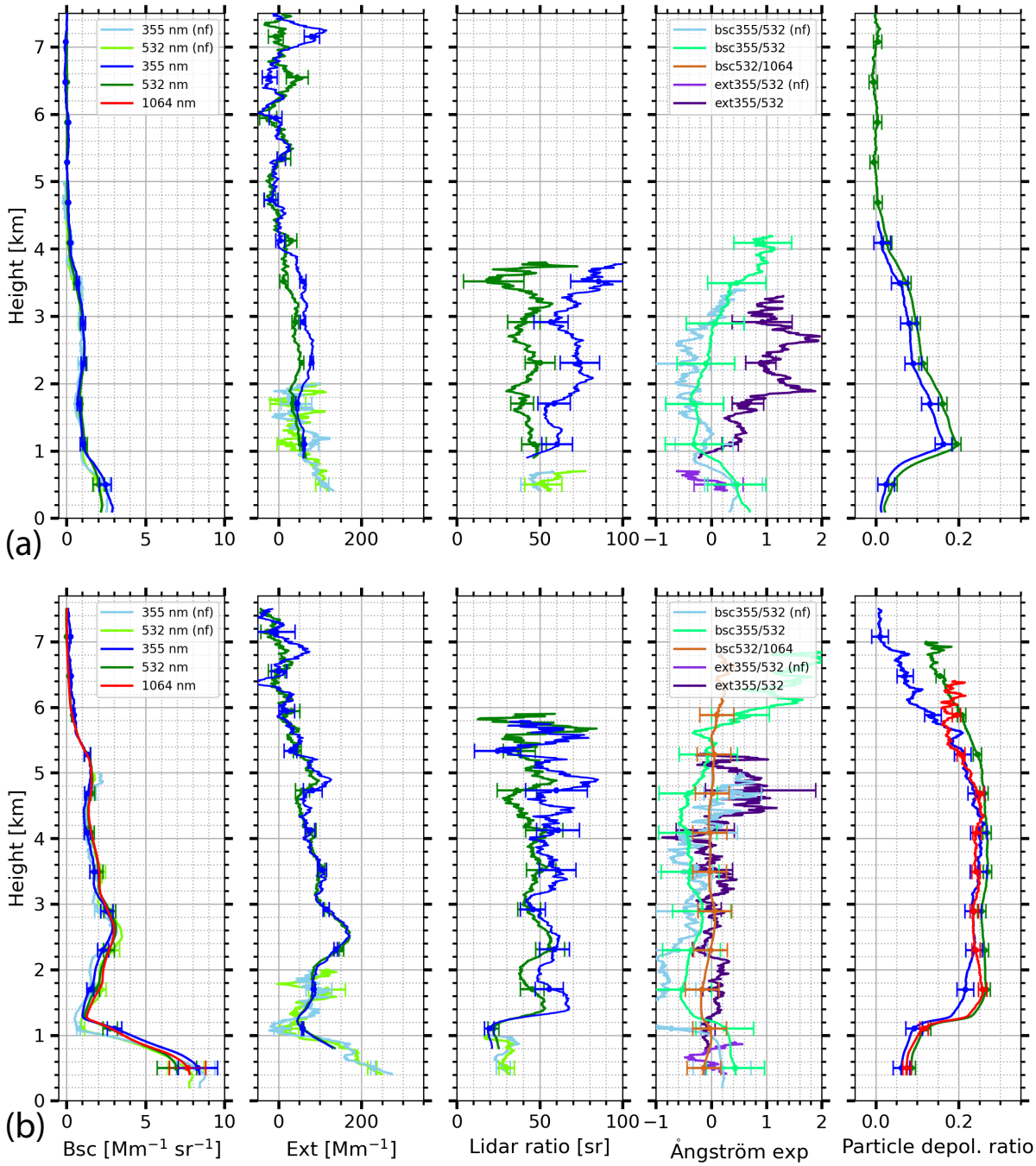

Figure 4.6: Automatically-retrieved vertical profiles of the aerosol optical properties measured with Polly^{XT} at Mindelo, Cabo Verde, on (a) 26 November 2021, 21:03–22:03 UTC, and (b) 4 August 2023, 21:02–22:02 UTC. From the left to the right, the particle backscatter and extinction coefficients, the lidar ratio the backscatter- (bsc) and extinction- (ext) related Ångström exponents and the particle linear depolarization ratio are displayed for the available wavelengths. The errors used for the error bars are described in Sect. 2.2.4.

backscatter coefficients reach their minimum at around 1 km height. However, the smaller PBL top height of 0.7 km was chosen because it is the middle of the transition zone. Although on 4 August, two peaks in the profiles of the particle backscatter and extinction coefficients can

be identified at around 2.6 and 5 km, respectively, the lofted aerosol layer was defined as one homogeneous layer reaching from 1.3 to 6.2 km because the intensive aerosol optical properties were nearly constant within this height range. Instead, on 26 November, a monotonic change with height was observed for the particle linear depolarization ratio and the backscatter-related Ångström exponent in the lofted aerosol layer, as already indicated by the color plot of the volume depolarization ratio. While there was only small vertical variation in the lidar ratio, the particle linear depolarization ratio strongly decreased with height in the lofted layer. In contrast, the backscatter- and extinction-related Ångström exponents partly increased with height in the lofted layer. Based on the structure of the particle backscatter coefficient and mainly the backscatter-related Ångström exponent, the lofted layer observed on 26 November was divided into three sublayers. The first sublayer was defined from 1.1 to 1.7 km with a nearly constant backscatter-related Ångström exponent < 0. The second sublayer was defined between 1.9 and 3.9 km, because the backscatter-related Ångström exponent increased to positive values before it was nearly constant at around 1 between 4 and 4.4 km height. Therefore, this height range was considered as a separate sublayer although it is almost negligible due to the very low values of the particle backscatter and extinction coefficients. Furthermore, the layer mean values of the lidar ratio and the extinction-related Ångström exponent are missing for this sublayer as the corresponding profiles were cut below that height due to strong noise. With the automatic algorithm of Hofer et al. (2020a), layer top heights of 4.4±0.05 and 6.7±0.05 km were retrieved for 26 November and 4 August, respectively. While the first fits exactly with the manually-defined layer top height, in the dust case, the automatically-retrieved layer top height is determined around 0.5 km higher than the manually-defined upper boundary of the lofted layer. Based on the particle linear depolarization ratio and the particle backscatter coefficient, aerosol was present up to a height of 6.7 km. However, above 6 km, the backscatter-related Ångström exponent between 355 and 532 nm strongly differed from the rest of the layer and the particle linear depolarization ratio at 355 and 532 nm already started to decrease at heights just below 6 km. Thus, the manually-defined upper boundary of the lofted layer seems to be more reasonable for the purpose of calculating layer mean values of the aerosol optical properties, while the automatically-retrieved layer top height might be the better approach for finding the highest heights, where aerosol particles were detected.

4.3.3 PBL

The corresponding layer mean and integrated aerosol optical properties for these case studies are given in Tab. 4.1. In the PBL, the backscattering was less in the mixing case than in the dust case, with values of the integrated particle backscatter coefficient of around $1.5 \times 10^{-3}\,\mathrm{sr}^{-1}$ (355 and 532 nm) compared with around $5.5 \times 10^{-3}\,\mathrm{sr}^{-1}$ (355, 532 and 1064 nm). Similarly, the AOD in the PBL was as low as 0.08 (355 and 532 nm) on 26 November and almost double on 4 August. Concluding from the small values of the AOD as well as the layer mean particle linear depolarization ratio of < 0.04 (at 355 and 532 nm), the presence of Saharan dust in the PBL can be excluded for 26 November. However, also no clean marine conditions existed indicated by the high layer mean lidar ratio of 48–57 sr (355 and 532 nm) indicating the presence of rather absorbing aerosol particles e.g., pollution-related or smoke. However, the low layer mean values of the Ångström exponent < 1.0 contradict this hypothesis. In case of pollution or smoke, values of > 1.0 are typical (Floutsi et al., 2023). Considering the date of this case, the presence of volcanic sulfate originating from La Palma could be possible. Although the layer mean lidar ratio was somewhat smaller than in the case study of 24 September 2021 (Gebauer et al., 2024), where layer mean values > 60 sr were reported for the wavelengths 355 and 532 nm, the layer mean values of the backscatter-related Ångström exponent were identical in both cases (0.4±0.5 on 26 November vs. 0.42±0.52 on 24 September). Using HYSPLIT backward trajectories (Fig. 4.7a),

Table 4.1: For the case study of 26 November 2021 and 4 August 2023: Geometric information about the PBL and the lofted layer as well as layer mean and integrated values of the aerosol optical properties as described in Sect. 3.6.1. The uncertainties were obtained as described in Sect. 2.2.4 and are neglected for the AOD, for which they were always smaller than 0.001. If the uncertainty exceeds the physically possible values, the range of possible values is given in brackets.

Date	26 Nov 2021, 21:03–22:03 UTC				4 Aug 2023, 21:02–22:02 UTC	
Layer top [km]	4.4±0.05				6.7±0.05	
Layer	PBL	lofted 1	lofted 2	lofted 3	PBL	lofted
Height [km]	0–0.7	1.1–1.7	1.9–3.9	4–4.4	0–0.7	1.3–6.2
Extensive aerosol optical properties and microphysical properties						
Integrated particle backscatter coefficient [$10^{-3}\,sr^{-1}$]						
355 nm	1.7±0.3	0.5±0.08	1.8±0.3	0.09±0.01	5.7±0.9	7.5±1.1
532 nm	1.4±0.2	0.6±0.09	1.7±0.3	0.06±0.01	5.3±0.8	8.4±1.3
1064 nm	-	-	-	-	5.3±0.8	8.5±1.3
Aerosol optical depth						
355 nm	0.08	0.03	0.13	<0.01	0.17	0.41
532 nm	0.08	0.03	0.07	<0.01	0.166	0.39
Dust fraction						
355 nm	<0.01	0.57±0.09	0.17±0.03	<0.01	0.08±0.01	0.90 (0.76–1.0)
532 nm	0.01±0.001	0.54±0.08	0.21±0.03	<0.01	0.17±0.03	0.81±0.12
1064 nm	-	-	-	-	0.15±0.02	0.91 (0.77–1.0)
Intensive aerosol optical properties and microphysical properties						
Lidar ratio [sr]						
355 nm	48±8	58±9	74±14	-	27±4	56±13
532 nm	57±12	42±7	41±12	-	29±5	46±11
Ångström exponent (b:backscatter related, e: extinction-related)						
b 355/532	0.4±0.5	-0.3±0.5	0.2±0.5	1.0±0.5	0.2±0.5	-0.3±0.5
b 532/1064	-	-	-	-	-0.1±0.3	0.0±0.3
e 355/532	-0.1±0.4	0.5±0.2	1.2±0.4	-	-0.1±0.2	0.2±0.4
Particle linear depolarization ratio						
355 nm	0.02±0.02	0.15±0.02	0.07±0.02	0.01 (0–0.03)	0.06±0.02	0.22±0.02
532 nm	0.04±0.01	0.18±0.01	0.10±0.01	0.02±0.01	0.09±0.01	0.26±0.01
1064 nm	-	-	-	-	0.08±0.01	0.23±0.01

the presence of aerosol mixtures containing smoke could be feasible as some of the trajectories of the ensemble crossed Guinea, where a strong fire activity was observed during that time as indicated by the FIRMS product. Apart from that, the trajectories mainly accumulated over the Atlantic Ocean between Cabo Verde and the Canary Islands from which possibly volcanic sulfate could have been advected. However, the lower lidar ratio and the small AOD suggest a mixture of marine aerosol and smoke. In contrast, on 4 August, the presence of Saharan dust in the PBL was likely. The layer mean lidar ratio of 27–29 sr (355 and 532 nm) and the layer mean particle linear depolarization ratio of 0.06–0.08 (355, 532 and 1064 nm) indicate a mixture of dust and marine particles (Floutsi et al., 2023). The calculated layer mean dust fraction of 0.08–0.15 (355, 532 and 1064 nm) confirms a low amount of dust mixed into the marine PBL. The layer

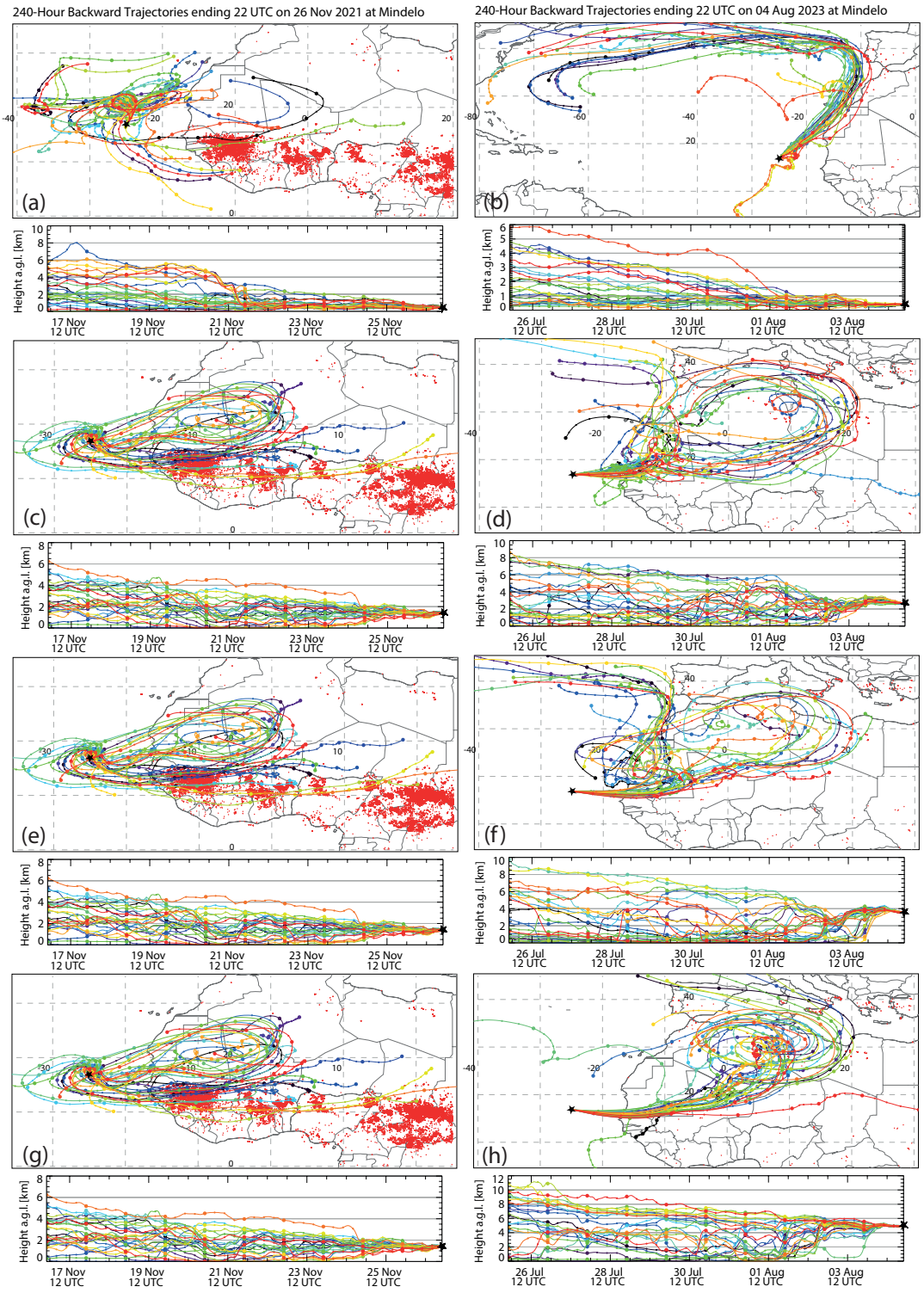

Figure 4.7: 10-days backward ensemble trajectories from HYSPLIT arriving at Mindelo (black star) on 26 November 2021, 22 UTC, at (a) 0.4 km, (c) 1.4 km, (e) 2.5 km and (g) 4.2 km and on 4 August 2023, 22 UTC, at (b) 0.4 km, (d) 2.7 km, (f) 3.6 km and (h) 5 km. MODIS fire activity (left panels: 16–26 November 2021, right panels: 26 July–4 August 2023) visualized by red dots (FIRMS, 2024, `firms.modaps.eosdis.nasa.gov`, last access: 2 May 2024).

mean values of the backscatter- and extinction-related Ångström exponents were around zero and, thus, lower than the values reported in literature (Floutsi et al., 2023), but within the range of an acceptable uncertainty for a dust-marine-mixture. Considering the HYSPLIT backward trajectories for the PBL on 4 August (Fig. 4.7b), the advection of desert dust is likely as they crossed the west coast of Morocco and Western Sahara.

4.3.4 Lofted aerosol layers

Concerning the lofted aerosol layers, a clear dominance of Saharan dust was seen on 4 August as indicated by the large layer mean dust fraction of 0.81–0.91 (355, 532 and 1064 nm). Furthermore, the layer mean lidar ratio of 45–56 sr (355 and 532 nm) was in a typical range for desert dust (Floutsi et al., 2023). The wavelength dependence of the aerosol optical properties confirms the presence of Saharan dust. The higher layer mean lidar ratio of 56±13 sr at 355 nm in contrast with 46±11 sr at 532 nm is in agreement with Veselovskii et al. (2020) indicating specific source regions in the Saharan desert. These are the regions in the northwestern Sahara around Algeria, Mauretania and Senegal as HYSPLIT backward trajectories (Fig. 4.7d) revealed. In addition, the layer mean particle linear depolarization ratio decreased from 0.26±0.01 at 532 nm to 0.23±0.01 at 1064 nm, i.e., a relative decrease of 12 %, which is in line with measurements at Morocco and Leipzig, Germany (Freudenthaler et al., 2009; Haarig et al., 2022), where a relative decrease of 13–31 % was observed for dust from the same source regions. The layer mean values of the Ångström exponent on 4 August 2023, which are around zero, fit well with what is known for Saharan dust from literature (Veselovskii et al., 2020; Floutsi et al., 2023). Generally, the intensive aerosol optical properties in the lofted aerosol layer did not vary with height on 4 August. This structure is in agreement with backward trajectories for different arrival heights covering the same areas in the northwestern Sahara (Figs. 4.7d, f and h). This geometrically thick dust layer caused an AOD of around 0.39–0.41 (355 and 532 nm). This is more than double than what was observed for the lofted layer on 26 November.

Generally, the lofted layer of the case of the mixing season strongly differed from the lofted layer of the dust case. Although the main contrasts are the smaller vertical extension and the large vertical inhomogenity on 26 November leading to a dissection into three sublayers, the lofted layer on that day also had a much lower aerosol load represented by an AOD of only 0.1 and 0.17 (355 and 532 nm). In terms of the aerosol load, the lowermost and the uppermost sublayer had a negligibly small contribution. As the intensive aerosol optical properties strongly differed between the sublayers, it is indeed necessary to consider them separately. For the lowermost sublayer, a notable contribution of dust was observed, expressed by the layer mean dust fraction of 0.54–0.57 (355 and 532 nm). The layer mean values of the Ångström exponents and the lidar ratio were in a similar range like for the lofted layer on 4 August, although the lidar ratio on 26 November exhibited a larger wavelength dependence with layer mean values of 58±9 sr at 355 nm (slightly larger than on 4 August) and 42±7 sr at 532 nm (slightly smaller than on 4 August). Together with the high layer mean particle linear depolarization ratio of 0.15±0.02 and 0.18±0.01 (355 and 532 nm), the presence of dust mixed with smoke is likely. HYSPLIT backward trajectories (Fig. 4.7c) confirm that a mixture of Saharan dust and smoke was observed. The large contribution of dust becomes evident as the trajectories mainly accumulated over Mauretania and northern Mali. Later on, they crossed Guinea and western Mali, regions for which a strong fire activity was recorded. In contrast, in the central sublayer, the contribution of dust decreased while the contribution of smoke increased, represented by the smaller layer mean particle linear depolarization ratio of 0.07–0.1 (355 and 532 nm) and the changes in the Ångström exponent and the lidar ratio. The latter exhibited a much larger wavelength dependence in the second sublayer. While a slight decrease to 41±12 sr at 532 nm was observed, the layer mean lidar ratio at 355 nm strongly increased to 74±14 sr. This spectral dependence is typical for dust-smoke mixtures

(Tesche et al., 2011a; Veselovskii et al., 2020; Floutsi et al., 2023). Another indicator for the presence of small, absorbing particles, i.e., smoke, is the extinction-related Ångström exponent between 355 and 532 nm, which strongly increased to a layer mean value of 1.2±0.4. Instead, the backscatter-related Ångström exponent between 355 and 532 nm strongly varied with height starting at around -0.3 at the bottom of this sublayer increasing to around 0.3 at its top. This increase, in combination with the particle linear depolarization ratio decreasing with height in the second sublayer, points to an increasing contribution of smoke and a decreasing contribution of dust with increasing height. Generally, the larger smoke and smaller dust contribution compared with the lowermost sublayer is confirmed by the trajectory analysis (Fig. 4.7e) showing still some trajoctories crossing over Mauretania and northern Mali but for some trajectories also a change towards a more easterly advection of air masses along the complete fire belt (cf. FIRMS fire spots in Fig. 4.7e) from Chad and Nigeria over the countries at the southern coast of West Africa. For higher arrival heights of the trajectories (Fig. 4.7g), the advection of air masses from the Saharan desert vanished while the trajectories still partly crossed the fire regions but were shifted to the south, where they mostly passed over the south coast of West Africa and the adjacent Atlantic Ocean. This pattern explains the missing contribution of dust in the uppermost sublayer (particle linear depolarization ratio close to zero). Instead, the backscatter-related Ångström exponent between 355 and 532 nm strongly increased to a layer mean value of 1.0±0.5, pointing to the contribution of small absorbing smoke particles.

4.3.5 Summary

To summarize, the presented case studies for the dust regime and the mixing regime strongly differed from each other. For the mixing case the total columnar lidar-derived AOD was 0.18 and 0.24 at 355 and 532 nm, respectively, with an only slightly higher contribution of the lofted layer (around 55–67 %). In contrast, the total AOD for the dust case was much higher with values of 0.55 to 0.58 at 355 and 532 nm and a larger contribution of the lofted layer (around 71 % at both wavelengths). These findings fit well with the AERONET sun photometer measurements for which a total columnar AOD of around 0.2 to 0.3 at 340–500 nm and around 0.5 at 340–440 nm on 26 November and 4 August, respectively, was recorded for the latest daytime measurements during these days and the first daytime measurements of the following days, each. On both days, the lofted layers represented the typical conditions, which were observed during SAMUM–2 with a geometrically and optically thick layer of Saharan dust during northern hemispheric summer and a dust-smoke-mix and a more complex vertical structure during northern hemispheric winter. While for the PBL on 26 November 2021 the existing aerosol types could not be distinctly classified, the PBL contaminated with some Saharan dust on 4 August 2023 is in contrast with the findings from SAMUM–2b. During that campaign, the typical situation was a clean marine PBL. If this difference arose from the inner-annual difference of both measurement periods (mid of May–mid of June for SAMUM–2b and 4 August for this case study) or may be explained by inter-annual variation will be discussed in Sect. 4.4. In the same section, the representativeness of the presented cases for the complete dust and mixing seasons will be discussed. Therefore, it is necessary to define in a first step the rough time frame of these seasons. In this context, the temporal evolution of the aerosol optical properties will be analyzed in detail.

4.4 Analysis of the annual cycle of aerosol optical properties

4.4.1 Aerosol layer top height

In this section, the temporal development of the aerosol conditions over Mindelo is presented based on the methods introduced in Sects.3.3–3.6.4 using one lidar profile for each Fri/Sat night.

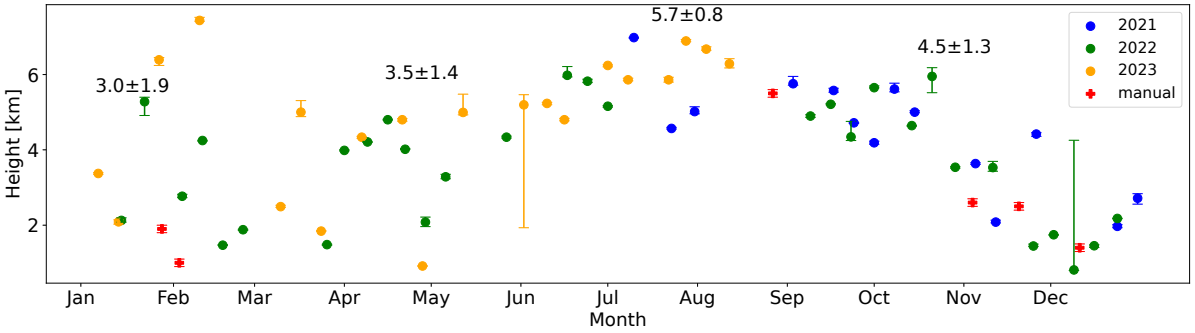

Figure 4.8: Aerosol layer top height (automatically-retrieved) for the Fri/Sat cases. Manually-defined layer top heights are given in red for cases with missing automatic results. The origin of the errors used for the error bars is described in Sect. 3.6.1. Seasonal mean values and their standard deviation plus the seasonal mean error are given as numbers.

Figure 4.8 provides the annual evolution of the aerosol layer top height for the Fri/Sat cases obtained from the automatic retrieval described in Sect. 3.6.4. The colors blue, green and orange indicate the years from which the measurement points originate. In 2022, the entire year could be covered, while the data points of the years 2021 and 2023 range from July to December and from January to August, respectively. Additionally, the layer top heights manually-defined by visual inspection for the cases having no particle backscatter coefficient at 532 nm (i.e., no automatically-retrieved layer top height) are included in red. Seasonal mean values for DJF, MAM, JJA and SON, not considering the manually-defined values, are added as numbers. Their uncertainty includes the temporal mean of the errors of the single data points (mean of upper and lower error bar due to their asymmetry) as well as the temporal standard deviation of the mean layer top heights. First, the seasonal means and standard deviations of the single years were calculated before both were averaged over the different years. Two outliers in the error bars are remarkable. On 9 December 2022, the PBL top was detected as layer top height when the defined threshold of $0.1\,\mathrm{Mm^{-1}sr^{-1}}$ for the particle backscatter coefficient at 532 nm was used while a lofted aerosol layer was present above. The latter was then recognized using the lower backscatter threshold value ($0.085\,\mathrm{Mm^{-1}sr^{-1}}$) for the error calculation, i.e., on that day, the correct layer top height is not represent by the given data point but by the endpoint of the upper error bar. In analogy, on 2 June 2023, the inverse effect was observed with the higher threshold value ($0.115\,\mathrm{Mm^{-1}sr^{-1}}$) detecting the PBL top instead of the top of the lofted aerosol layer. In that case, the data point represents the layer top height correctly.

Concerning the temporal evolution of the layer top height, from May to December, a clear annual cycle with low short-term variability was observed. In the months before, more fluctuation was present. The larger variability from January to April can be partly explained with the automatic algorithm performing worse during that time than during the rest of the year (cf. Sect. 3.6.4). However, there was also slightly more variability in the layer top height from January to April. Considering the occurrence of more diverse aerosol structures during SAMUM–2a, i.e., during January and February of one specific year, the larger variability of the layer top height observed at Mindelo between January and April is reasonable. The mean aerosol layer top height for DJF was 3.0±1.9 km. For the MAM-period a mean value of 3.5±1.4 km was calculated. From May onwards, the layer top heights started to increase from values around 4 km height to values of 6–7 km height during July. From August onwards, the layer top height decreased again and droped below 4 km in October, reaching a minimum of < 1 km in the first half of December. Afterwards, an increase to layer top heights of around 2 km was observed. Seasonal

mean values for JJA and SON are 5.7±0.8 km and 4.5±1.3 km, respectively. The measurements analyzed here suggest the main period of the dust regime to be in July, when the highest layer top heights at around 6 km were detected. The results discussed here give a quantified measure of the aerosol layering above Mindelo and, thus, confirm and, therefore, mature the qualitative impression provided in Fig. 4.1.

4.4.2 Geometrical and optical layer properties

In Fig. 4.9, (a) the occurrence and extent of the single aerosol layers and (b) the layer-resolved AOD are presented. The PBL reached from 400 to 500 m up to heights of around 2 km. The largest values were observed between October and April. In these cases, often no lofted aerosol layer was present. However, during this time of the year, the variation of the PBL height was large and also low PBL top heights of approximately 400 m occurred. During northern hemispheric summer, the top height of the PBL was mainly in the range of 700 m up to around 1 km. The top height of the lofted layer distinctly increased during northern hemispheric spring and summer and was usually lower in northern hemispheric fall and winter. Generally, the lofted layer was geometrically thicker during northern hemispheric summer having an extent of up to 4 km. During northern hemispheric fall and winter, shallow low lofted layers of around 1 km extent were observed in addition to thick lofted layers of around 4 km extent. Occasionally, there was not even a clearly separated lofted layer. In some cases, the lofted layer was split into different sublayers, similarly to the case of the mixing season presented in Sect. 4.3. This is valid for 29 measurements, which are distributed all over the complete annual cycle. In four of these cases (26 Nov 2021, 9 Sep 2022, 14 Oct 2022, 9 Jun 2023), three sublayers were defined, while in the other 25 cases, they were split into two sublayers. Multiple lofted layers, which were distinctively separated from each other, were only observed on 13 and 27 January 2023. Furthermore, shallow layers of dried marine aerosol directly above the top of the PBL but separated from the lofted layer were observed especially during northern hemispheric summer, e.g., on 12 August 2023.

Besides the geometrical thickness of the layers, the layer-resolved AOD at 532 nm was calculated from the lidar-derived extinction profiles and is shown in Fig. 4.9b together with the columnar AOD at 500 nm from AERONET. As the sun photometer measurements exist only for daytime and the lidar-derived AOD was derived during night, the latest AERONET measurement from the day before was averaged with the first measurement of the day after. If only one of both measurements was available, either the latest data point from the evening or the first data point from the morning was taken as reference. To provide as much homogenity as possible, level 1.5 data were used, as the level 2 data were only available until 14 March 2023. However, level 1.5 data at 500 nm were not available from 21 April 2023 onwards as well. For the period from 21 April–12 August 2023, the average of the AERONET AOD at 440 and 675 nm was used for the comparison. In most cases, the AERONET AOD totally agreed with the sum of the layer AODs derived from the lidar measurements. Large deviations between both methods with larger AERONET AODs were observed for the first five cases, which can be explained by the missing AOD of the PBL due to missing near-field profiles at 532 nm on these dates. Furthermore, having a larger AERONET AOD compared with the lidar-derived one was expected as the visual inspection for the definition of the layer boundaries was kept quite conservative. Thus, in some cases, a few meters at the bottom and the top of the aerosol layers were neglected as well as the transition zones between the different layers. In contrast, in the AERONET AOD the total atmospheric column was considered. Observed differences between the lidar-derived AOD and the AERONET AOD can be also attributed to the rapidly changing aerosol conditions between the different measurement times (nighttime vs. daytime). This was the case on 12 August 2023, when the AERONET AOD was about 0.25 larger than the total lidar-derived one. The latter, characterizes the atmosphere around 1 UTC in the morning, while the AERONET AOD is from

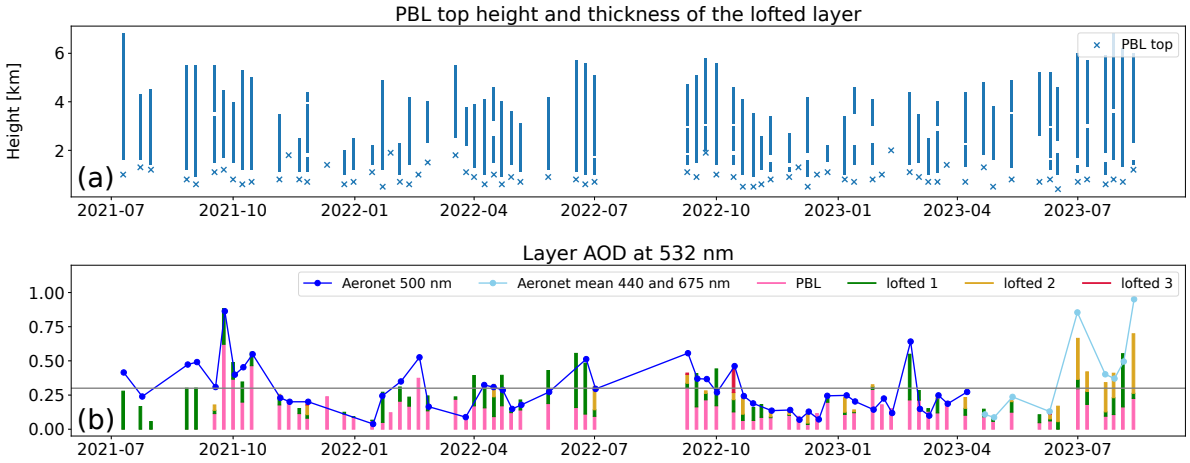

Figure 4.9: Time series of the Fri/Sat cases including (a) the PBL height and the occurrence of lofted layers and (b) the layer-resolved lidar-derived AOD at 532 nm in comparison with the columnar AOD from AERONET.

11:30 UTC, when the lofted aerosol layer was of larger intensity. AERONET data for the day before (11 August) are not available. The general agreement of both methods to derive the AOD emphasizes the validity and representivity of the selected cases while the lidar measurements allow a layer-resolved evaluation of the AOD.

Concerning the temporal development of the total and the layer-AOD, a large annual variation can be identified. Large total AODs up to values of around 0.5 and 0.6 were observed in June–July 2022 and in July–August 2023, respectively. In these periods, the contribution of the lofted layers to the total AOD was usually at least 50 %. Furthermore, an agreement with the layer thickness was found, i.e., during these summer months, the observed lofted layers were geometrically and optically thick. The opposite was observed in the spring season, both, in 2022 and 2023, when geometrically thick lofted layers (extending up to 4 km) caused only small values of the AOD (usually <0.1). During November–February, the total AOD of <0.1 up to around 0.3 was generally lower and the contribution of the lofted layer was usually smaller than the one of the PBL compared with June–August. However, single outliers were observed, e.g., on 24 February 2023, when the total AOD was around 0.55. A lofted aerosol layer of around 4 km extent having an AOD of around 0.33 was present. Another outstanding pattern was observed in September/October 2021, when the total AOD reached comparably high values up to 0.9 driven by a large contribution (60–80 %) of the PBL. This anomaly was caused by the volcanic eruption at La Palma, Canary Islands as described in Gebauer et al. (2024) by means of a case study analysis. The evening of 24 September represents the largest AOD of all analyzed Fri/Sat cases with a value of 0.88 at 532 nm. Additionally to that case, the volcanic influence was evident for at least two more dates: 1 and 15 October 2021. The presence of volcanic sulfate in the PBL is also indicated by the high layer mean values of the lidar ratio at 532 nm (Fig. A.2b), which ranged from around 49 sr on 1 October to $>$ 60 sr on 24 September and 15 October while the layer mean particle linear depolarization ratio (Fig. A.2f) was close to zero. Apart from that, layer mean values of the lidar ratio of up to 60 sr were only observed on 26 November 2021 (still period of volcanic activity) and around the beginning of January 2022 in combination with a higher layer mean particle linear depolarization ratio of around 0.1 indicating the presence of polluted dust.

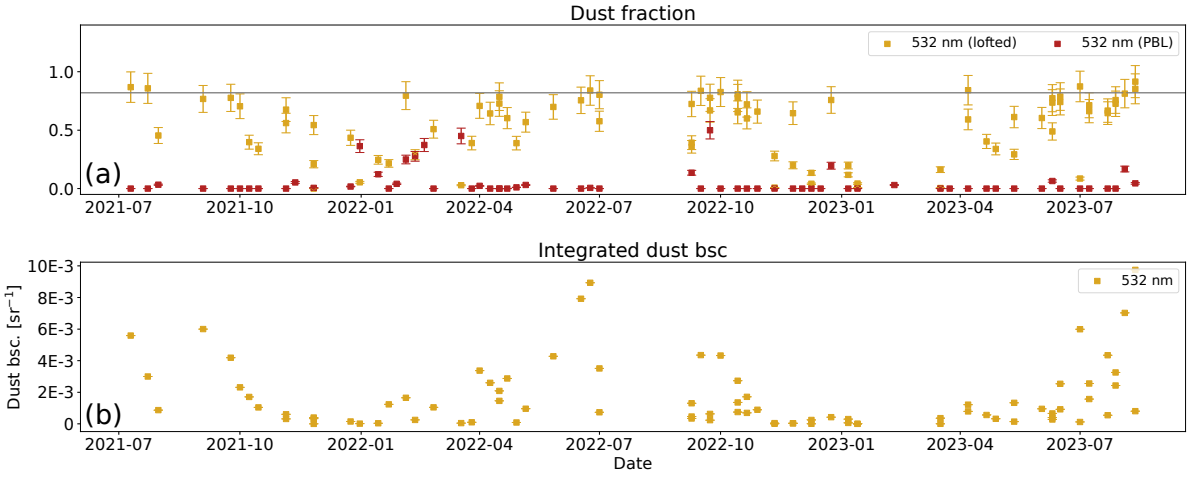

Figure 4.10: Time series of the Fri/Sat cases including (a) the dust fraction at 532 nm for the PBL and the lofted layers and (b) the integrated dust backscatter at 532 nm for the lofted layers.

4.4.3 Dust fraction and integrated dust backscatter coefficient

The layer mean dust fraction, displayed for 532 nm in Fig. 4.10a, is a major property allowing us to characterize the dust occurrence in the aerosol layers presented in the previous section. For the PBL, the layer mean dust fraction observed was negligibly low for most of the cases and, thus, we conclude that dust was not present in the PBL for most parts of the evaluated period. A higher dust fraction in the PBL with layer mean values up to 0.5 was found between 31 December 2021 and 18 March 2022 as well as during September 2022 and on 23 December 2022. Especially during the period December 2021–March 2022, the dust fraction of the lofted layer was comparably small and in a similar range as for the PBL. These findings indicate a low dust content in the lofted layers during winter and spring, furthermore supported by the small values of the integrated dust backscatter coefficient (Fig. 4.10b), and the mixing of the dust down into the PBL. In contrast, during summer, the dust contribution was clearly separated between the PBL and the lofted layer with almost no dust in the PBL and dust fractions up to 0.9 in the lofted layer. However, due to the assumption of the dust particle linear depolarization ratio of 0.31 in the POLIPHON algorithm (Tesche et al., 2009), the layer mean dust fraction hardly exceeded 0.9 even in the summer months, i.e., June–August, when largest dust fractions were observed. Usually, they were in the range of 0.7–0.9. A value of 0.82 was found as the 90th percentile (horizontal line in Fig. 4.10a). In these periods, the integrated dust backscatter partly increased up to 0.009 sr^{-1}. The annual cycle of the dust fraction with higher layer mean values in the summer months than in the winter months originates from the temporal development of the particle linear depolarization ratio (Fig. A.2e and f) showing high layer mean values >0.2 during summer and low layer mean values around 0.1 during winter for the lofted layer as well as low layer mean values close to zero in summer and high layer mean values around 0.1 in winter for the PBL. In all cases, the layer mean particle linear depolarization ratio was larger at 532 nm compared with 355 nm. This finding is in agreement with the spectral dependence as known from literature for the typical aerosol types at Mindelo, i.e., Saharan dust, dust-smoke-mixtures and marine aerosol (Tesche et al., 2011a; Floutsi et al., 2023).

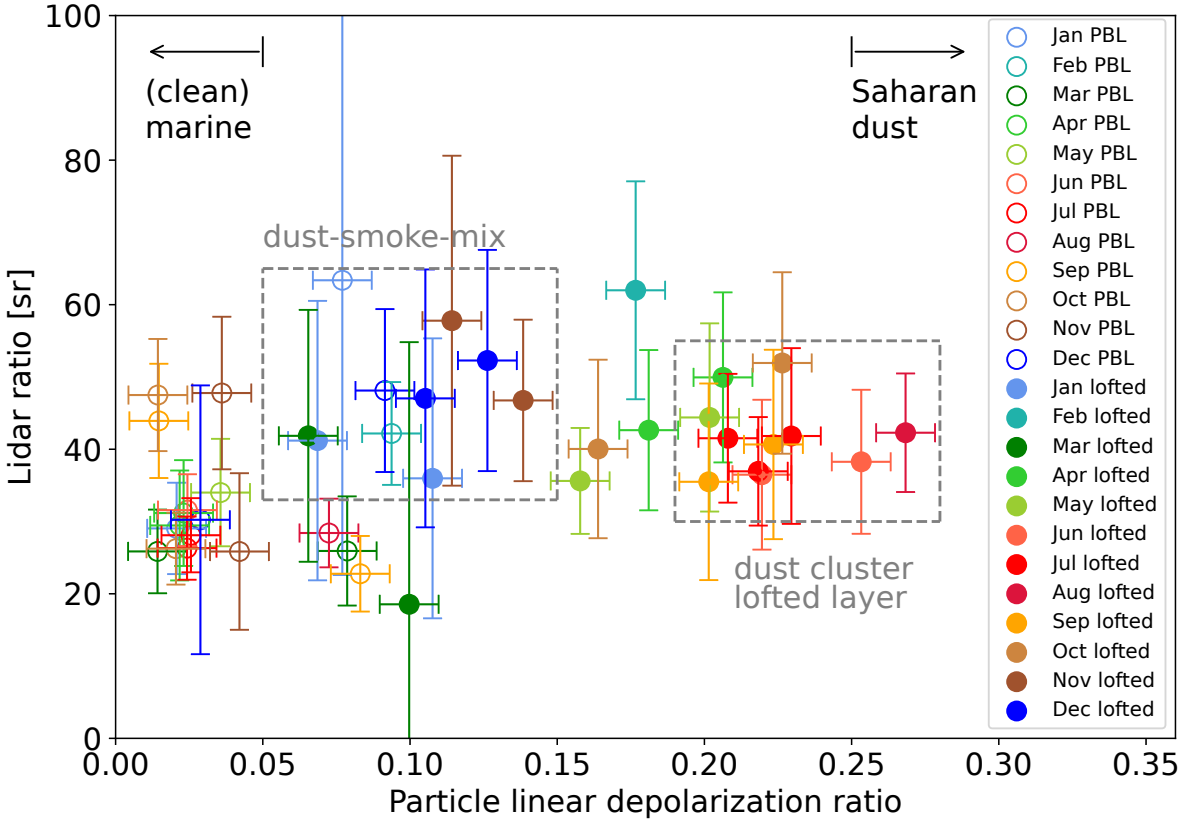

Figure 4.11: Monthly mean particle linear depolarization ratio vs. monthly mean lidar ratio (both at 532 nm) for the PBL and the lofted layer (unfilled and filled circles, respectively) based on the Fri/Sat cases. The error bars include the monthly mean error (described in Sect. 3.6.1) plus the standard deviation (temporal variability).

4.4.4 Lidar ratio and particle linear depolarization ratio

The measured lidar ratio (Fig. A.2a) followed an annual cycle, in consistency with the annual cycle of the dust fraction in the lofted layer. During northern hemispheric summer, layer mean values of around 40–60 sr usually were observed at 355 and 532 nm. From October onwards, an increase in the lidar ratio at 355 nm and in the wavelength dependence could be identified. Especially during winter 2022/2023, layer mean values of the lidar ratio of around 70–80 sr were reached at 355 nm while the layer mean lidar ratio at 532 nm was around 40 sr. In combination with the lower layer mean values of the particle linear depolarization ratio around 0.1, the observed pattern was typical for a mixture of dust and smoke particles.

Creating a 2D space of the lidar ratio and the particle linear depolarization ratio allows a more concrete evaluation of the temporal behavior of the several aerosol types present in the different aerosol layers, as shown in Floutsi et al. (2023). In Fig. 4.11, it is shown for 532 nm including data points for the PBL (unfilled circles) and for the lofted aerosol layers (filled circles). The original data were averaged over the single months of the several years. The corresponding time series of these monthly mean values for the single layers can be found in Fig. A.3. From June to September, the monthly means of the layer mean particle linear depolarization ratio of the lofted aerosol layers were always > 0.2 while the corresponding lidar ratio was around 40 sr (cf. gray dashed rectangle in Fig. 4.11 labelled as "dust cluster lofted layer"). In consistency with the assumptions made for the lidar target classification (Baars et al., 2017), a particle linear

depolarization ratio > 0.2 represents dust particles. However, the observed depolarization ratio was mostly small compared to the values prevalent in literature. According to Floutsi et al. (2023), Saharan dust typically shows a particle linear depolarization ratio > 0.25, which was seen in the study presented here only for the monthly mean values of June 2022 and August 2023 (cf. Fig.A.3h). However, Saharan dust as the main contributor can be still identified for the described lofted layers analyzed in the study presented here, confirmed by a dust fraction > 60 % (cf. Fig. A.3b). Instead, for the lofted aerosol layers from November to January, the monthly mean particle linear depolarization ratio varied between 0.05–0.15 while monthly mean values of the lidar ratio of around 40 sr and up to 60 sr were observed. However, the findings indicate a mixture of dust and smoke particles (Tesche, 2011; Tesche et al., 2011a). Small monthly mean particle linear depolarization ratios were also found for the lofted layers of March—both in 2022 and 2023. In contrast, the only existing monthly mean data point for the lofted layers of February (2022) had a particle linear depolarization ratio of around 0.18 and a lidar ratio of around 60 sr caused by the presence of two days with occurrence of dust (4 and 25 February 2022). These observations cannot be contextualized as the number of measurements is generally limited and often either the particle linear depolarization ratio or the lidar ratio is missing at 532 nm for this time of the year. For the months April, May and October, the monthly mean values of the particle linear depolarization ratio and the lidar ratio in the lofted layers varied between 0.15–0.25 and 30–50 sr, respectively, indicating that pure dust as well as dust-mixtures occurred during that time of the year. The data points showing a monthly mean particle linear depolarization ratio > 0.2 occurred in April, May and October 2022 and may point to a longer-lasting dust season during that year compared with 2021 and 2023. However, a clear main dust season with dust occurrence in the lofted aerosol layer ranging from June to September could be identified based on Fig. 4.11 as well as an explicit mixing season with dust-smoke-mixtures in the lofted layers covering the months November to January. Considering the data point of February 2022 as an outlier, the mixing season might extend until March as indicated by the monthly mean data points for March originating from two different years.

In contrast to the lofted layers, the monthly mean particle linear depolarization ratio in the PBL was usually < 0.05 while the lidar ratio was in the range of 20–40 sr. These are typical values for (clean) marine conditions. Higher monthly mean lidar ratios in this cluster of low depolarization ratios were observed for September–November 2021. In all these cases, the lidar ratio reached monthly mean values around 50 sr. The high values in fall 2021 coincided with the volcanic eruption at La Palma and can be attributed to volcanic sulfate (Gebauer et al., 2024). A second cluster of monthly mean data points of the PBL can be found with particle linear depolarization ratios between 0.07 and 0.1. The monthly mean lidar ratio in these cases ranged from 40 to 60 sr for December 2021–February 2022 and from 20 to 30 sr for March 2022, September 2022 and August 2023 (cf. Fig. A.3h). The months with the higher lidar ratios, i.e., the winter months, were associated with dust-smoke-mixtures and are clearly embedded in the cluster of data points for the lofted layer during that time of the year, i.e., the aerosol types occurring in the PBL and in the lofted layers were similar. Instead, in the cases of March 2022, September 2022 and August 2023, a mixture of dust and marine aerosol was present in the PBL, indicated by the enhanced particle linear depolarization ratio but the relatively low lidar ratio.

In fact, a slight seasonal dependence could be observed for the PBL as well, having a mixture of dust and smoke during northern hemispheric winter, more precisely December–February, and mainly clean marine conditions for the rest of the year. For the months of the mixing season, this pattern is in agreement with the findings from SAMUM–2a, according to which more complex and diverse aerosol layers both in the PBL and in the lofted layer are typical. On the other side, the prevalence of only a clean marine PBL during the dust regime could not be proven with the study presented here as dust-marine-mixtures occurred as well. Furthermore, with the volcanic

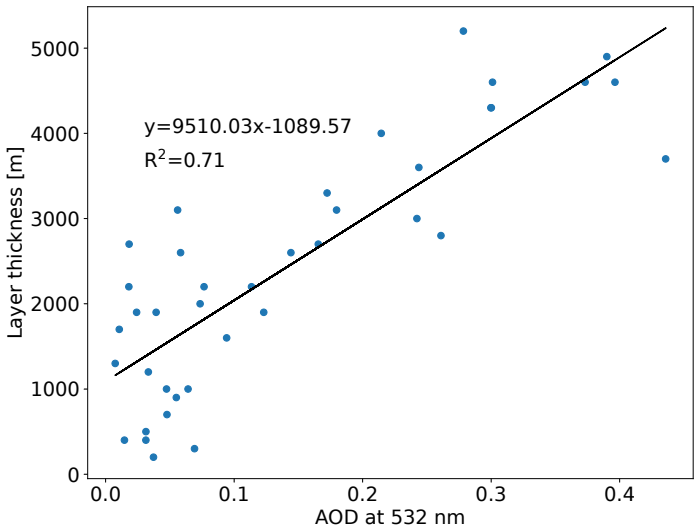

Figure 4.12: Geometrical thickness of the lofted aerosol layer in dependence of its AOD at 532 nm for the Fri/Sat cases of May–September.

period, a completely untypical situation was captured.

4.4.5 Definition of the seasons at Mindelo

Based on two years of lidar profiling, a first attempt to distinctly define the dust season and the mixing season at Mindelo was done. Therefore, several criteria were applied to the results presented in the sections before.

One approach to define the dust regime at Mindelo uses the AOD and its correlation with the layer thickness. According to Barnaba & Gobbi (2004) and Kosmopoulos et al. (2008), a dust event is characterized by an AERONET AOD > 0.3 at 550 nm (cf. gray horizontal line in Fig. 4.9b). Despite the agreement between the AERONET AOD and the lidar-derived AOD in this study, the latter one at 532 nm is used in this approach for reasons of consistency with the following criteria, which were newly defined within the framework of this thesis: One of them is that the contribution of the lidar-derived AOD of the lofted layer to the total lidar-derived AOD exceeded 50 %. Furthermore, a correlation between the AOD of the lofted layer and its geometrical thickness was tested for several months of northern hemispheric spring to fall and different combinations of them. A total lidar-derived AOD > 0.3 dominated by the lofted layer was found for most cases in the periods from April to the mid of October 2022 and in July and August 2023. As no lidar-derived AOD for the PBL was available from July to the beginning of September 2021, for this time span, the AOD of the PBL was approached by the difference of the AERONET AOD and the lidar-derived AOD of the lofted layer. According to this approach, the aforementioned months fulfill the criterion of a contribution of the lofted aerosol layer AOD to the total AOD of > 50 % as well. Thus, the months July, August and September can be assigned for sure to the dust regime as most of the corresponding cases meet the required conditions for dust events, (AOD > 0.3 at 532 nm and contribution of the lofted aerosol layer AOD > 50 %) in at least two different years. Furthermore, these are the months for which the largest layer top heights were observed. For the months April, May, June and October, a clear classification is not yet possible as a higher variability was observed and the criteria where not met each year. Thus, they may be considered as transition months to or from the dust season.

Considering the geometrical thickness of the lofted layer as an indicator for the dust season,

a positive correlation with the optical thickness was found for the months April–October. For different combinations of these months, the linear regression models were checked and evaluated based on the coefficient of determination (square of correlation coefficient). The best value of the coefficient of determination was found for a combination of May and June. For the period from May to September, the coefficient of determination is 0.71 and, thus, confirms the positive correlation between the geometrical and the optical thickness of the lofted aerosol layers during the dust season. The corresponding scatter plot is shown in Fig. 4.12.

A further indicator for the months belonging to the dust season was found by illustrating the seasonal and layer mean lidar ratio in dependence of the seasonal and layer mean particle linear depolarization ratio previously discussed in Sect. 4.4.4 based on Fig. 4.11. A dust cluster (indicated by the gray dashed rectangle in Fig. 4.11) can be found for the months June–September, which show a particle linear depolarization ratio > 0.2 and lidar ratio around 40–50 sr. Additionally, in 2022, the months April, May and October were seen in this cluster and mostly included dust cases fulfilling the criteria of a total AOD > 0.3 and a contribution of the lofted layer to the total AOD of $> 50\,\%$.

To conclude, within the framework of this thesis, the dust regime at Mindelo was identified to include the months having a monthly mean particle linear depolarization ratio > 0.2 for the lofted aerosol layer and the months of which the single measurement cases show a total AOD > 0.3, a contribution of the lofted aerosol layer AOD to the total AOD of $> 50\,\%$ and a positive correlation between the geometrical and the optical thickness of the lofted aerosol layers. These criteria were met for the months June–September in multiple years and for April, May and October in 2022. Thus, the dust season generally has been determined to occur in the time period June–September. The months April, May and October were found to be transition months.

The corresponding seasonal mean geometrical and aerosol optical properties are summarized in Tab. 4.2. The dust regime was characterized by an average layer top height of around 5.6 km and geometrically and optically thick lofted layers of Saharan dust (average thickness of around 4 km and seasonal mean lidar-derived layer AOD of around 0.23–0.25 at 355 and 532 nm, respectively). A seasonal mean dust fraction of around 0.65–0.77 at 355, 532 and 1064 nm, respectively, and a mean lidar ratio of around 39–48 sr at 355 and 532 nm, respectively, were observed in the lofted layer. In the PBL, the dust content was low (dust fraction around 0.03–0.07 at 355, 532 and 1064 nm, respectively), but single cases with a dust-marine-mixture occurred. The relatively large seasonal mean AOD of 0.18–0.19 as well as the slightly enhanced seasonal mean lidar ratio of around 32–34 sr in the PBL were caused by the volcanic sulfate, which was observed in September 2021. In the case study of 4 August 2023, higher values of the aerosol layer top height as well as AOD and dust fraction of the lofted layer were observed compared with the seasonal mean values for the dust season. This selected case study originated from the main period of the dust season, while the seasonal mean of course includes some inner-seasonal variability influenced by less dusty cases as well.

The definition of a mixing season, the definition was less clear than for the dust season. Using as main criterion the occurrence of dust in the PBL in combination with a lower dust content in the lofted layer, in Fig. 4.11, a cluster of data points was identified (gray dashed rectangle in Fig. 4.11) with monthly mean values of the particle linear depolarization ratios between 0.02–0.15 and a monthly mean lidar ratio between 30–70 sr. Generally, this cluster for the non-pure marine PBL covers the months November–March. Several cases in January and March showed an Ångström exponent > 0.61 for the lidar ratio (typical for dust-smoke-mixtures) in combination with a dust fraction < 0.5 at 532 nm, both in the lofted aerosol layers. This was valid also for single cases in November and December, in the transition month April and for one case in June. Finally, the mixing regime was defined as the period from November to March, when dust in the PBL and smoke-dust-mixtures in the lofted aerosol layer were observed.

Table 4.2: Seasonal mean geometrical, microphysical and aerosol optical properties for the dust and the mixing regime at Mindelo. Far-field measurements were used for the lofted layer and near-field measurements for the PBL (except at 1064 nm and for the particle linear depolarization ratio and the dust fraction). The uncertainty includes the seasonal mean of the errors described in Sect. 3.6.1 plus the temporal standard deviation of the corresponding property. If the uncertainty exceeds the physically possible values, the range of possible values is given in braces. Sublayers of the lofted layer were considered separately for averaging, except for the AOD and the layer thickness, which are given for the total lofted layer.

Months	Dust season Jun–Sep		Mixing season Nov–Mar	
Layer	PBL	lofted	PBL	lofted
Geometrical properties [km]				
Layer top (auto.)	-	5.6±0.9	-	3.0±1.8
Layer top (vis.)	0.9±0.4	4.3±1.7	1.0±0.4	3.1±1.1
Extent	0.9±0.4	4.1±1.2	1.0±0.4	1.6 (0–3.4)
Extensive aerosol optical properties and microphysical properties				
Integrated particle backscatter coefficient [$10^{-3}\,sr^{-1}$]				
355 nm	4.5±3.0	3.1±2.9	4.1±3.1	1.2 (0–2.8)
532 nm	5.2±3.8	3.5±3.5	3.5±2.5	0.9 (0–2)
1064 nm	2.5±1.7	2.8 (0–5.8)	3.9±2.9	0.7±0.7
Aerosol optical depth				
355 nm	0.19±0.17	0.25±0.13	0.15±0.08	0.07 (0–0.16)
532 nm	0.18±0.14	0.23±0.13	0.15±0.07	0.05 (0–0.12)
Dust fraction				
355 nm	0.03 (0–0.12)	0.65±0.32	0.03 (0–0.11)	0.32±0.29
532 nm	0.05 (0–0.17)	0.70±0.28	0.09 (0–0.24)	0.28 (0–0.57)
1064 nm	0.07 (0–0.19)	0.77 (0.48–1.0)	0.20±0.17	0.56±0.44
Intensive aerosol optical properties				
Lidar ratio [sr]				
355 nm	34±18	48±19	33±16	63±33
532 nm	32±19	39±18	38±25	47±32
Ångström exponent (b: backscatter-related, e: extinction-related)				
b 355/532	0.5±0.8	-0.1±1.1	0.5±0.8	0.0±1.2
b 532/1064	0.3±0.7	0.3±0.7	0.3±0.4	0.7±0.6
e 355/532	0.3±0.7	0.2±0.6	0.0±0.8	0.7±0.9
Particle linear depolarization ratio				
355 nm	0.02 (0–0.07)	0.16±0.07	0.03 (0–0.08)	0.17 (0–0.41)
532 nm	0.04 (0–0.09)	0.22±0.06	0.05 (0–0.11)	0.11±0.07
1064 nm	0.05±0.05	0.20±0.05	0.06±0.05	0.16±0.08

The seasonal mean geometrical and aerosol optical properties for the mixing season are presented in Tab. 4.2, too. A seasonal mean layer top height of around 3 km and an average extent of the lofted aerosol layer of around 1.6 km were found. The AOD in the lofted layer was only half of the AOD of the PBL and in total a mean AOD of around 0.2 was found for the mixing regime. Some dust contribution in the lofted layer is included in the seasonal mean values, lead-

ing to a dust fraction of around 0.28–0.56 at 355, 532 and 1064 nm and a lidar ratio of 63±33 and 47±32 sr at 355 and 532 nm, respectively. The higher lidar ratio at 355 nm and the larger wavelength dependence indicate the contribution of smoke in the mixing regime. The case study of 26 November 2021 differs from the seasonal mean values. In contrast to the average values of the mixing season, in the case study, a much larger layer top height of around 4.4 km was observed and the AOD was larger in the lofted layer than in the PBL. However, the layer mean lidar ratios have similar values as the seasonal means given in Tab. 4.2. The mixing regime is characterized by more seasonal variability and the chosen example only represents a snapshot of the complete season. However, both chosen case studies are representative for the two main seasons. The definition of these seasons at Mindelo is of course only a first attempt based on two years of lidar observations. The long-term observations envisaged in the framework of ACTRIS for the next decade will show how mich inter-annual varibaility will occur over Mindelo in a changing climate.

4.4.6 Comparison with SAMUM–2

With the continuous lidar observations at Mindelo covering two complete annual cycles, many findings from SAMUM–2 can be consolidated but also a more detailed insight in the complete annual cycle of the aerosol occurrence over Cabo Verde is given including, e.g., a layer-resolved AOD as well as a two-year time series of lidar ratio profiles and dust fractions, which has not been available before. Similarities to SAMUM–2 are, for instance, the observed distribution of aerosol layers with a more complex layering during the mixing regime, while during the dust regime, usually geometrically thick lofted layers of Saharan dust were present.

Apart from that, several differences were found between the seasonal mean values at Mindelo and the results from SAMUM–2. The fact that the measurements during SAMUM–2 were obtained at an island further south obviously had less effect on these differences than the different measurement time within the annual cycle. SAMUM–2b captured some weeks at the beginning of the dust regime (May/June of one specific year) explaining the lower mean aerosol layer top height of 4.4±0.7 km compared with the seasonal mean aerosol layer top height of 5.6±0.9 km. At Mindelo, the lofted aerosol layers during May and June also did not reach as high as during the main period in July and August. Furthermore, during SAMUM–2b, there was always a clean marine PBL, while dust-marine-mixtures were found in this study, e.g., in the case study of 4 August 2023. At the beginning of the dust regime, dust-marine-mixtures were absent in the measurements at Mindelo as well. However, this difference concerning the PBL could of course also be caused by inter-annual variation. Furthermore, the seasonal mean lidar ratio of the lofted layer was slightly lower for the dust season (48±19 and 39±18 sr at 355 and 532 nm, respectively) compared with SAMUM–2b, when 53±10 and 54±10 sr were observed at 355 and 532 nm, respectively, but the uncertainties given in Tab. 4.2 indicate a strong seasonal variability for the measurements at Mindelo. The particle linear depolarization ratio of the lofted aerosol layers was mostly smaller during the dust season (≤ 0.22). During SAMUM–2b, a mean particle linear depolarization ratio of 0.31±0.1 was found. Differences were also found between the seasonal mean values of the mixing season and SAMUM–2a. The seasonal mean layer top height of 3.04±1.8 km and the seasonal mean total AOD of 0.20±0.14 (at 532 nm) are smaller compared with a mean layer top height of 3.5±1.2 km and a mean AERONET AOD of 0.35±0.18 at 500 nm for SAMUM–2a. Main difference is that during SAMUM–2a no wavelength dependence of the lidar ratio was found. However, further studies collected in Floutsi et al. (2023) indicated a wavelength dependence for dust-smoke-mixtures or for pure smoke. The seasonal mean values of the particle linear depolarization ratio of the lofted aerosol layer agree with the findings from SAMUM–2a (mean particle linear depolarization ratio of 0.15±0.05 at 532 nm) but were smaller (values around 0.1) for most cases within this season.

Chapter 5

Conclusions and outlook

In this thesis, the annual cycle of the aerosol conditions and the cloud occurrence over Mindelo was analyzed based on a two-year data set of multiwavelength-Raman-polarization lidar measurements of Polly^{XT} covering the period from July 2021 to August 2023. Vertical profiles of the aerosol optical properties were derived automatically with the Raman method using the Polly^{NET} processing chain. Improvements in the cloud screening routines of the Polly^{NET} processing chain were made but this process also demonstrated the challenges of the gradient method. Using the lidar target classification for the cloud screening may be considered for future work on the automatic retrieval. One profile per week, originating from the nights from Fridayn to Saturday, i.e., the nights of the overpass of the Aeolus satellite over Mindelo, was chosen and manually reviewed with regard to quality assurance. However, a need for improvements in the calibration of the vertical profiles was seen. For instance, the particle backscatter coefficients at 355 and 532 nm were derived in around 40 and 65 % of the analyzed cases only, respectively. For the 1064 nm channel, it was even less with the particle backscatter coefficient available only in around 15 % of all the cases. Layer boundaries of the PBL and lofted aerosol layers were defined based on visual inspection. An automatic retrieval of the aerosol layer top height was used in addition and compared with the manually-derived results even though both approaches do per se use different definitions. Layer mean and integrated values of the aerosol optical properties were calculated and used for the general analysis of the two-year period. Thus, a quality-assured time series of more than 70 measurement cases was analyzed to obtain detailed insights into the annual cycle using a layer-resolved approach. In contrast to the manual analysis of lidar vertical profiles, which has been most common so far (e.g., Tesche, 2011; Hofer et al., 2020a; Heese et al., 2022), the automatically-retrieved profiles obtained from the Polly^{NET} processing chain allowed to evaluate a larger amount of data. Additionally, two case studies were presented to contrast the aerosol conditions between the two main seasons—the dust season and the mixing season.

Furthermore, a statistical analysis of the cloud occurrence based on the lidar-derived target classification was presented and discussed as the presence of clouds turned out to be an essential factor for the characterization of the atmospheric conditions over Mindelo. On 98 % of all days and in 43 % of all time bins, clouds were detected. The occurrence of more than one cloud level per day (in 91 % of all cloudy days) and especially the presence of low-level clouds (in 98 % of all cloudy days) revealed to be of importance for the measurement site. However, due to the limitations of a lidar-based investigation of the cloud occurrence, which is affected by the strong attenuation by clouds leading to an underestimation of higher clouds when lower clouds are present, a bias in the analysis of higher-level clouds has to be considered. No annual cycle in the occurrence of low-level clouds could be found but a small annual variation in the number of days having mid-level clouds while low-level clouds were absent. The latter was slightly larger during May–October capturing the dust season. As dust particles are effective INPs, the pres-

ence of more mid-level clouds during periods with strong dust occurrence proves the importance of dust for cloud formation in this region. A concrete investigation of the correlation of the observed mid-level clouds and the presence and properties of the dust layers would be beneficial and should be subject of future studies. Furthermore, the analysis of the diurnal cycle of the cloud occurrence may also be of interest especially as no clear annual cycle could be identified in this study. However, for future studies concerning the cloud occurrence over Mindelo, a more appropriate instrument than the aerosol lidar or also a synergistic approach should be used. The results of this study clearly revealed the need for a cloud radar, which has been set up in 2024 at the measurement site at the OSCM.

Plenty of new insights in the aerosol conditions over Mindelo were obtained within this study. It is the first time that a two-year time series of layer-resolved AOD, lidar ratio profiles and the dust fractions was made for Cabo Verde. The results showed a clear seasonal cycle for the extent, the AOD and the dust fraction of the lofted aerosol layers. An increase in these properties was identified during northern hemispheric spring and summer reaching a maximum in July/August (main dust period) after which a decrease was found towards a minimum in northern hemispheric winter (mixing season). Generally, in most cases at least one lofted layer existed, but sometimes it was split further into two or three sublayers. Geometrically distinctly separated lofted layers were almost absent. Furthermore, a different contribution of the lofted layers to the total AOD was revealed. While during the mixing regime, the AOD was driven by the PBL, in the dust regime, the lofted layer accounted for the largest contribution.

One major aim of this thesis was to investigate the time frame of the dust season and the mixing season. Although these main seasons generally overlap with the European summer and winter seasons (JJA and DJF, respectively), they are not well represented by only these months. According to this study, the dust season covers June–September and was extended from May to October in 2022. This dust season is characterized by a monthly mean particle linear depolarization ratio > 0.2 in the lofted aerosol layer. Furthermore, the dominating aerosol types are clearly separated between the different layers showing a prevalence of (pure) dust in the lofted aerosol layers (dust fraction $> 60\,\%$) and mainly clean marine conditions in the PBL. Dust mixed into the PBL is occasionally observed during that season. An nontypical exception was the occurrence of volcanic sulfate in the PBL in September 2021 (Gebauer et al., 2024). Aerosol layer top heights up to 7 km are typical in the dust season. Vertically homogeneous lofted aerosol layers with a depth of around 4 km and an AOD in the lofted layer of up to 0.5 at 532 nm (seasonal mean 0.23) are frequently observed. As a consequence, the columnar AOD (seasonal mean 0.41) is mainly controlled by the lofted layer (seasonal mean contribution of around 56 %).

The mixing season includes the months November–January and likely extends towards March. This season is characterized by a PBL and lofted aerosol layers with monthly mean values of the particle linear depolarization ratio in the range of 0.05–0.15 and a larger spectral dependence of the lidar ratio in the lofted layer. More inner-seasonal variablility concerning the occurrence of aerosol layers and different aerosol types is characteristic as well compared with the dust season. Lofted aerosol layers can have a depth of up to 4 km like in the dust regime but can also be only 1 km thick or completely absent. A strong variation in the PBL top height is also typical, which reaches values up to 2 km height when no lofted layer is present. Generally, the optical properties of the PBL and the lofted layers are more similar than during the dust season, often influenced by a smoke-dust-mixture with a dust fraction of around 40–50 %. However, a clean marine PBL was also observed in about 64 % of the time. The total AOD is small (seasonal mean 0.2 at 532 nm) and mainly driven by the PBL (contribution of around 75 %).

According to these newly-defined time ranges for the main seasons at Mindelo, SAMUM–2b was carried out more at the beginning of the dust season while SAMUM–2a was at the end of the mixing season. Nevertheless, the general conclusions from SAMUM–2, including a marine

influenced PBL clearly differing from vertically homogeneous lofted layers of Saharan dust during the dust regime and more complex structures and various aerosol types in the mixing regime could be confirmed. However, also many new findings compared to the ones from SAMUM–2 were made. For example, a clean marine PBL was not always present in the dust season but also mixtures of marine aerosol with dust particles and even a mix of marine aerosol and volcanic sulfate was observed. Furthermore, the particle linear depolarization ratio in the lofted layer was lower compared with existing knowledge about Saharan dust leading to a dust fraction hardly reaching 90 %. The main difference to SAMUM–2a is the wavelength dependence of the lidar ratio, which was not observed in that previous campaign.

To conclude, the results of this thesis generally confirm the existing knowledge about the aerosol conditions over Cabo Verde but provide a more detailed in-depth analysis of the different seasons based on two years of lidar observations—thus, only a starting point for inter-annual analyses. As the measurements at Mindelo are ongoing, data covering a longer time period will be available soon, allowing to study the inter-annual variability of the aerosol conditions over Mindelo. Therefore, more robust methods for the automatic analysis of the data and an automatized quality control of the retrieved vertical profiles are needed. Further possibilities for future research also exist with regard to the depolarization and extinction measurements at 1064 nm. The automatic calibration of the particle backscatter coefficient and the particle linear depolarization ratio at 1064 nm has to be improved in the Polly$^{\mathrm{NET}}$ processing chain so that these properties are retrieved more often. Extinction measurements at 1064 nm have been presented already in single case studies by Haarig et al. (2022) and Gebauer et al. (2024) but require some intense characterizations before their implementation in the Polly$^{\mathrm{NET}}$ processing chain. Furthermore, the application of the HETEAC-Flex model (Floutsi et al., 2024) to obtain an automatical layer-resolved aerosol classification is planned for future studies. Finally, the focus on Fri/Sat nights chosen for this study offers large potential to use this unique data set as a baseline for the validation of the Aeolus satellite, which is still needed, as reprocessing efforts are ongoing and new products will be released also after the end of the active mission.

Appendix A

Time series of aerosol optical properties

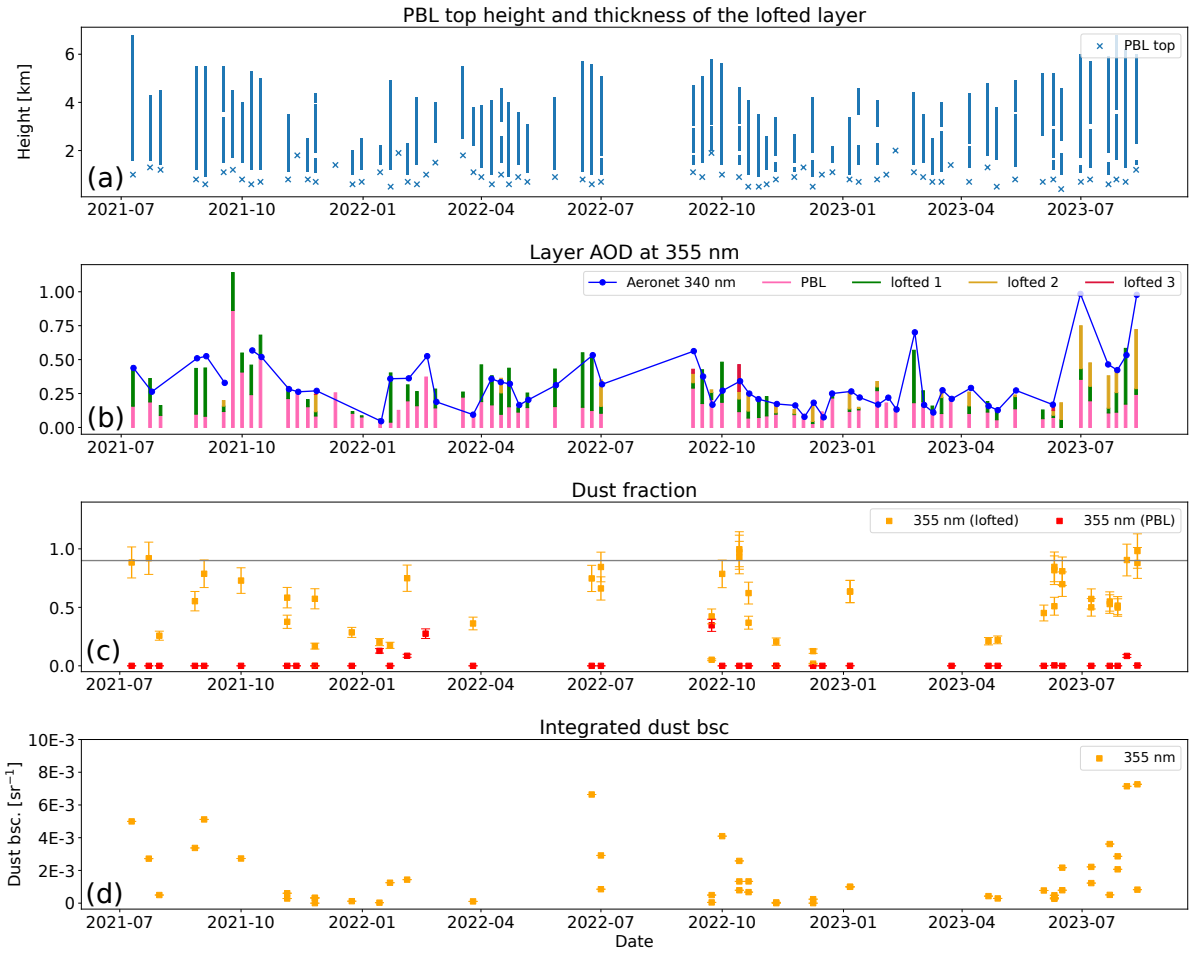

Figure A.1: Combination of Fig. 4.9 and Fig. 4.10 but for 355 nm.

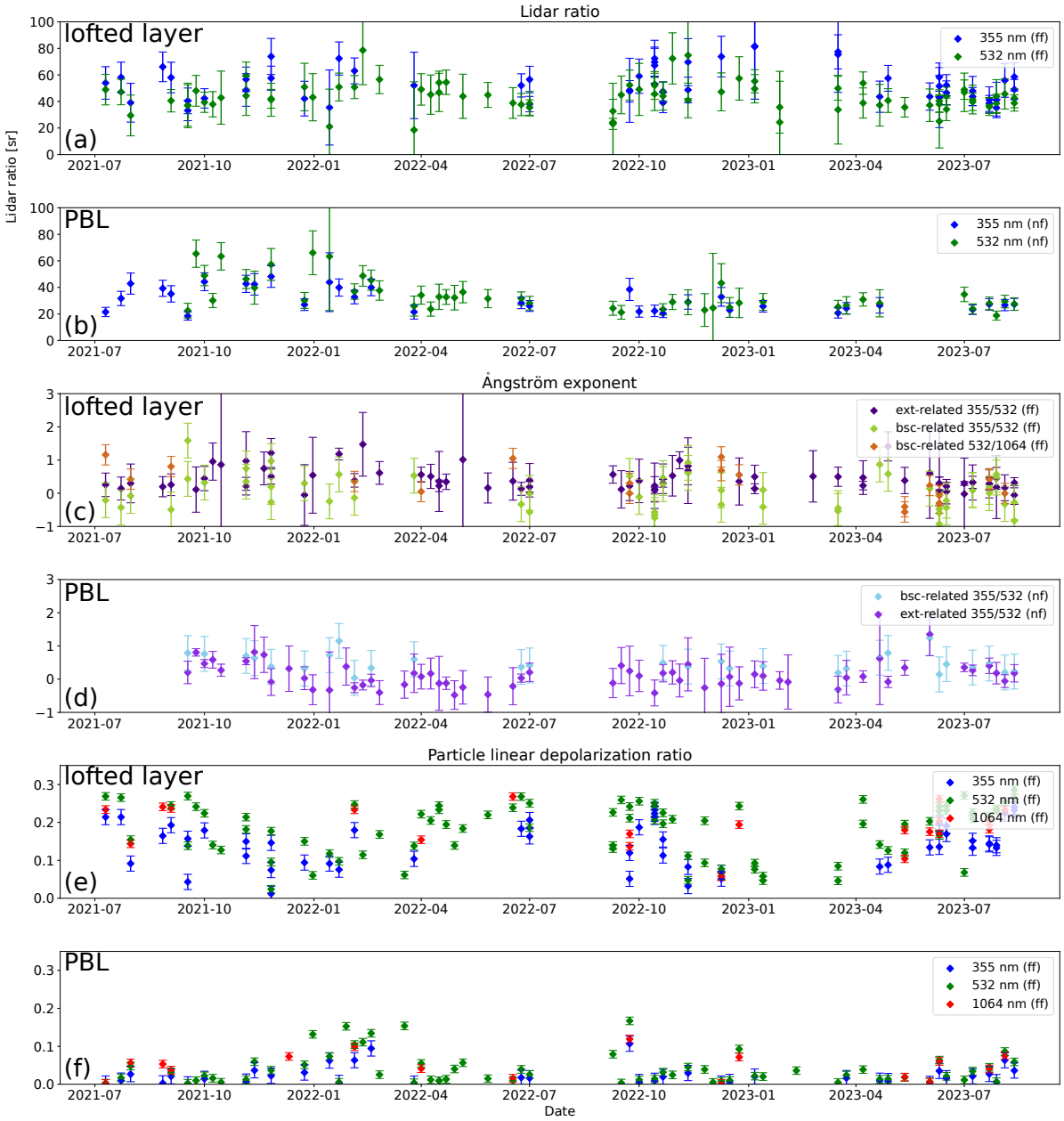

Figure A.2: Layer resolved time series of the Fri/Sat cases including (a) and (b) the lidar ratio at 355 and 532 nm, (c) and (d) the backscatter- and extinction-related Ångström exponent for the wavelength pairs 355/532 nm and 532/1064 nm and (e) and (f) the particle linear depolarization ratio at 355, 532 and 1064 nm. Near- and far-field measurements are labelled as "nf" and "ff", respectively.

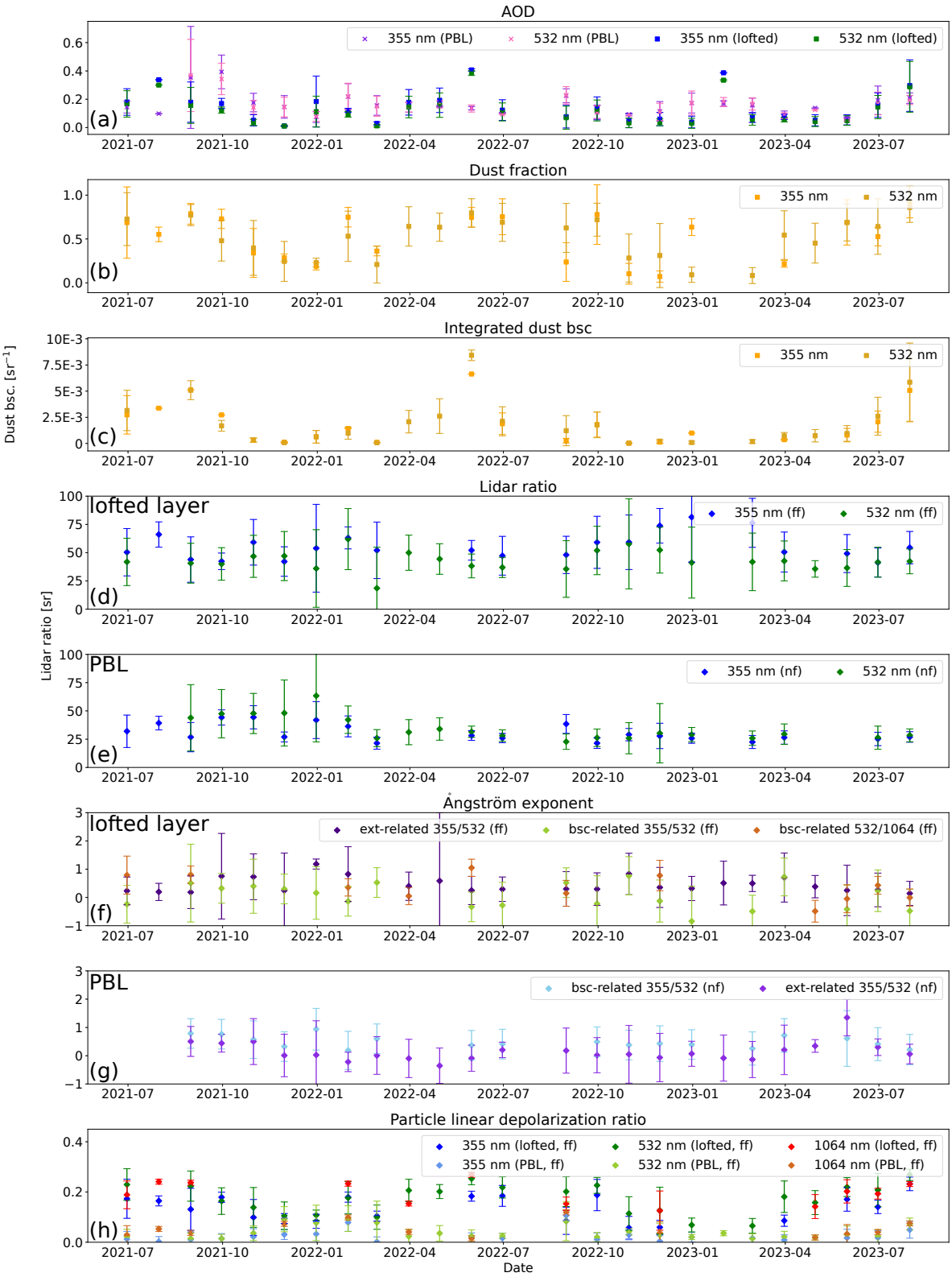

Figure A.3: Layer resolved time series of monthly means of the Fri/Sat cases including (a) and (b) the lidar ratio at 355 and 532 nm, (c) and (d) the backscatter- and extinction-related Ångström exponent for the wavelength pairs 355/532 nm and 532/1064 nm and (e) and (f) the particle linear depolarization ratio at 355, 532 and 1064 nm. Near- and far-field measurements are labelled as "nf" and "ff", respectively.

Bibliography

ACTRIS (2024). The Aerosol, Clouds and Trace Gases Research Infrastructure, available at https://www.actris.eu, last access: 11 June 2024.

Adler, G., Flores, J. M., Abo Riziq, A., Borrmann, S., & Rudich, Y. (2011). Chemical, physical, and optical evolution of biomass burning aerosols: a case study. *Atmospheric Chemistry and Physics*, 11(4), 1491–1503. https://doi.org/10.5194/acp-11-1491-2011

Alonso-Blanco, E., Calvo, A. I., Pont, V., Mallet, M., Fraile, R., & Castro, A. (2014). Impact of Biomass Burning on Aerosol Size Distribution, Aerosol Optical Properties and Associated Radiative Forcing. *Aerosol and Air Quality Research*, 14(3), 708–724. https://doi.org/10.4209/aaqr.2013.05.0163

Althausen, D., Engelmann, R., Baars, H., Heese, B., Ansmann, A., Müller, D., & Komppula, M. (2009). Portable Raman Lidar PollyXT for Automated Profiling of Aerosol Backscatter, Extinction, and Depolarization. *Journal of Atmospheric and Oceanic Technology*, 26(11), 2366 – 2378. https://doi.org/10.1175/2009JTECHA1304.1

Amiridis, V., Marinou, E., Paschou, P., Baars, H., Pirloaga, R., Engelmann, R., Tsekeri, A., Tsikoudi, I., Daskalopoulou, V., Kazadzis, S., Skupin, A., Marenco, F., Kezoudi, M., Kouklaki, D., Siomos, N., Floutsi, A. A., Metallinos, S., Spanakis-Misirlis, V., Raptis, P., Althausen, D., Seifert, P., Nemuc, A., Antonescu, B., Papetta, A., & Wandinger, U. (2023). *ASKOS Campaign Dataset*. https://doi.org/10.60621/jatac.campaign.2021.2022.caboverde. last access: 11 June 2024

Ansmann, A., Mamouri, R.-E., Hofer, J., Baars, H., Althausen, D., & Abdullaev, S. F. (2019). Dust mass, cloud condensation nuclei, and ice-nucleating particle profiling with polarization lidar: updated POLIPHON conversion factors from global AERONET analysis. *Atmospheric Measurement Techniques*, 12(9), 4849–4865. https://doi.org/10.5194/amt-12-4849-2019

Ansmann, A. & Müller, D. (2005). Lidar and Atmospheric Aerosol Particles. *Lidar: Range-Resolved Optical Remote Sensing of the Atmosphere*, volume 102 of *Springer Series in Optical Sciences*, 105–141. Springer New York, (1 ed.). https://doi.org/10.1007/0-387-25101-4_4

Ansmann, A., Petzold, A., Kandler, K., Tegen, I., Wendisch, M., Mueller, D., Weinzierl, B., Mueller, T., & Heintzenberg, J. (2011a). Saharan Mineral Dust Experiments SAMUM–1 and SAMUM–2: what have we learned? *Tellus B: Chemical and Physical Meteorology*, 63(4), 403–429. https://doi.org/10.1111/j.1600-0889.2011.00555.x

Ansmann, A., Tesche, M., Seifert, P., Groß, S., Freudenthaler, V., Apituley, A., Wilson, K. M., Serikov, I., Linné, H., Heinold, B., Hiebsch, A., Schnell, F., Schmidt, J., Mattis, I., Wandinger, U., & Wiegner, M. (2011b). Ash and fine-mode particle mass profiles from EARLINET-AERONET observations over central Europe after the eruptions of the Eyjafjallajökull volcano

in 2010. *Journal of Geophysical Research: Atmospheres*, 116(D20). https://doi.org/10.1029/2010JD015567

Ansmann, A., Wandinger, U., Riebesell, M., Weitkamp, C., & Michaelis, W. (1992). Independent measurement of extinction and backscatter profiles in cirrus clouds by using a combined Raman elastic-backscatter lidar. *Applied Optics*, 31(33), 7113–7131. https://doi.org/10.1364/AO.31.007113

Baars, H., Ansmann, A., Althausen, D., Engelmann, R., Heese, B., Müller, D., Artaxo, P., Paixao, M., Pauliquevis, T., & Souza, R. (2012). Aerosol profiling with lidar in the Amazon Basin during the wet and dry season. *Journal of Geophysical Research: Atmospheres*, 117(D21). https://doi.org/10.1029/2012JD018338

Baars, H., Ansmann, A., Engelmann, R., & Althausen, D. (2008). Continuous monitoring of the boundary-layer top with lidar. *Atmospheric Chemistry and Physics*, 8(23), 7281–7296. https://doi.org/10.5194/acp-8-7281-2008

Baars, H., Kanitz, T., Engelmann, R., Althausen, D., Heese, B., Komppula, M., Preißler, J., Tesche, M., Ansmann, A., Wandinger, U., Lim, J.-H., Ahn, J. Y., Stachlewska, I. S., Amiridis, V., Marinou, E., Seifert, P., Hofer, J., Skupin, A., Schneider, F., Bohlmann, S., Foth, A., Bley, S., Pfüller, A., Giannakaki, E., Lihavainen, H., Viisanen, Y., Hooda, R. K., Pereira, S. N., Bortoli, D., Wagner, F., Mattis, I., Janicka, L., Markowicz, K. M., Achtert, P., Artaxo, P., Pauliquevis, T., Souza, R. A. F., Sharma, V. P., van Zyl, P. G., Beukes, J. P., Sun, J., Rohwer, E. G., Deng, R., Mamouri, R.-E., & Zamorano, F. (2016). An overview of the first decade of PollyNET: an emerging network of automated Raman-polarization lidars for continuous aerosol profiling. *Atmospheric Chemistry and Physics*, 16, 5111–5137. https://doi.org/10.5194/acp-16-5111-2016

Baars, H., Seifert, P., Engelmann, R., & Wandinger, U. (2017). Target categorization of aerosol and clouds by continuous multiwavelength-polarization lidar measurements. *Atmospheric Measurement Techniques*, 10(9), 3175–3201. https://doi.org/10.5194/amt-10-3175-2017

Barnaba, F. & Gobbi, G. P. (2004). Aerosol seasonal variability over the Mediterranean region and relative impact of maritime, continental and Saharan dust particles over the basin from MODIS data in the year 2001. *Atmospheric Chemistry and Physics*, 4(9/10), 2367–2391. https://doi.org/10.5194/acp-4-2367-2004

Belegante, L., Nicolae, D., Nemuc, A., Talianu, C., & Derognat, C. (2014). Retrieval of the boundary layer height from active and passive remote sensors. Comparison with a NWP model. *Acta Geophysica*, 62, 276–289. https://doi.org/10.2478/s11600-013-0167-4

Borne, M., Knippertz, P., Weissmann, M., Witschas, B., Flamant, C., Rios-Berrios, R., & Veals, P. (2024). Validation of Aeolus L2B products over the tropical Atlantic using radiosondes. *Atmospheric Measurement Techniques*, 17(2), 561–581. https://doi.org/10.5194/amt-17-561-2024

Burton, S. P., Ferrare, R. A., Hostetler, C. A., Hair, J. W., Rogers, R. R., Obland, M. D., Butler, C. F., Cook, A. L., Harper, D. B., & Froyd, K. D. (2012). Aerosol classification using airborne High Spectral Resolution Lidar measurements – methodology and examples. *Atmospheric Measurement Techniques*, 5(1), 73–98. https://doi.org/10.5194/amt-5-73-2012

Chen, G., Ziemba, L. D., Chu, D. A., Thornhill, K. L., Schuster, G. L., Winstead, E. L., Diskin, G. S., Ferrare, R. A., Burton, S. P., Ismail, S., Kooi, S. A., Omar, A. H., Slusher, D. L., Kleb,

M. M., Reid, J. S., Twohy, C. H., Zhang, H., & Anderson, B. E. (2011). Observations of Saharan dust microphysical and optical properties from the Eastern Atlantic during NAMMA airborne field campaign. *Atmospheric Chemistry and Physics*, 11(2), 723–740. https://doi.org/10.5194/acp-11-723-2011

Choobari, O. A., Zawar-Reza, P., & Sturman, A. (2014). The global distribution of mineral dust and its impacts on the climate system: A review. *Atmospheric Research*, 138, 152–165. https://doi.org/10.1016/j.atmosres.2013.11.007

Cloud mask - documentation (2024). Polly^{NET} processing chain: cloud mask documentation available at https://pollynet.github.io/Pollynet_Processing_Chain/lib.html#module-lib.cloudmask, last access: 11 June 2024.

Davies, D. K., Ilavajhala, S., Wong, M. M., & Justice, C. O. (2009). Fire Information for Resource Management System: Archiving and Distributing MODIS Active Fire Data. *IEEE Transactions on Geoscience and Remote Sensing*, 47(1), 72–79. https://doi.org/10.1109/TGRS.2008.2002076

Deshler, T. (2008). A review of global stratospheric aerosol: Measurements, importance, life cycle, and local stratospheric aerosol. *Atmospheric Research*, 90(2), 223–232. https://doi.org/10.1016/j.atmosres.2008.03.016

Di Biagio, C., Balkanski, Y., Albani, S., Boucher, O., & Formenti, P. (2020). Direct Radiative Effect by Mineral Dust Aerosols Constrained by New Microphysical and Spectral Optical Data. *Geophysical Research Letters*, 47(2), e2019GL086186. https://doi.org/10.1029/2019GL086186

Engelmann, R., Kanitz, T., Baars, H., Heese, B., Althausen, D., Skupin, A., Wandinger, U., Komppula, M., Stachlewska, I. S., Amiridis, V., Marinou, E., Mattis, I., Linné, H., & Ansmann, A. (2016). The automated multiwavelength Raman polarization and water-vapor lidar Polly^{XT}: the neXT generation. *Atmospheric Measurement Techniques*, 9(4), 1767–1784. https://doi.org/10.5194/amt-9-1767-2016

Fehr, T., McCarthy, W., Amiridis, V., Baars, H., von Bismarck, J., Borne, M., Chen, S., Flamant, C., Marenco, F., Knipperz, P., Koopman, R., Lemmerz, C., Marinou, E., Močnik, G., Parrinello, T., Piña, A., Reitebuch, O., Skofronick-Jackson, G., Zawislak, J., & Zenk, C. (2023). The Joint Aeolus Tropical Atlantic Campaign 2021/2022 Overview–Atmospheric Science and Satellite Validation in the Tropics, EGU General Assembly 2023, Vienna, Austria, 24–28 Apr 2023, EGU23-7249. Technical report. https://doi.org/10.5194/egusphere-egu23-7249

Fernald, F. G. (1984). Analysis of atmospheric lidar observations: some comments. *Applied Optics*, 23(5), 652–653. https://doi.org/10.1364/AO.23.000652

FIRMS (2024). Fire Information for Resource Management System, available at: firms.modaps.eosdis.nasa.gov, last access: 11 June 2024.

Floutsi, A. A., Baars, H., Engelmann, R., Althausen, D., Ansmann, A., Bohlmann, S., Heese, B., Hofer, J., Kanitz, T., Haarig, M., Ohneiser, K., Radenz, M., Seifert, P., Skupin, A., Yin, Z., Abdullaev, S. F., Komppula, M., Filioglou, M., Giannakaki, E., Stachlewska, I. S., Janicka, L., Bortoli, D., Marinou, E., Amiridis, V., Gialitaki, A., Mamouri, R.-E., Barja, B., & Wandinger, U. (2023). DeLiAn – a growing collection of depolarization ratio, lidar ratio and Ångström exponent for different aerosol types and mixtures from ground-based lidar observations. *Atmospheric Measurement Techniques*, 16(9), 2353–2379. https://doi.org/10.5194/amt-16-2353-2023

Floutsi, A. A., Baars, H., & Wandinger, U. (2024). HETEAC-Flex: an optimal estimation method for aerosol typing based on lidar-derived intensive optical properties. *Atmospheric Measurement Techniques*, 17(2), 693–714. https://doi.org/10.5194/amt-17-693-2024

Formenti, P., Elbert, W., Maenhaut, W., Haywood, J., & Andreae, M. O. (2003). Chemical composition of mineral dust aerosol during the Saharan Dust Experiment (SHADE) airborne campaign in the Cape Verde region, September 2000. *Journal of Geophysical Research: Atmospheres*, 108(D18). https://doi.org/10.1029/2002JD002648

Freudenthaler, V., Esselborn, M., Wiegner, M., Heese, B., Tesche, M., Ansmann, A., Müller, D., Althausen, D., Wirth, M., Fix, A., Ehret, G., Knippertz, P., Toledano, C., Gasteiger, J., Garhammer, M., & Seefeldner, M. (2009). Depolarization ratio profiling at several wavelengths in pure Saharan dust during SAMUM 2006. *Tellus B: Chemical and Physical Meteorology*. https://doi.org/10.1111/j.1600-0889.2008.00396.x

Gebauer, H., Floutsi, A. A., Haarig, M., Radenz, M., Engelmann, R., Althausen, D., Skupin, A., Ansmann, A., Zenk, C., & Baars, H. (2024). Tropospheric sulfate from Cumbre Vieja (La Palma) observed over Cabo Verde contrasted with background conditions: a lidar case study of aerosol extinction, backscatter, depolarization and lidar ratio profiles at 355, 532 and 1064 nm. *Atmospheric Chemistry and Physics*, 24(8), 5047–5067. https://doi.org/10.5194/acp-24-5047-2024

Gong, X., Wex, H., Voigtländer, J., Fomba, K. W., Weinhold, K., van Pinxteren, M., Henning, S., Müller, T., Herrmann, H., & Stratmann, F. (2020). Characterization of aerosol particles at Cabo Verde close to sea level and at the cloud level – Part 1: Particle number size distribution, cloud condensation nuclei and their origins. *Atmospheric Chemistry and Physics*, 20(3), 1431–1449. https://doi.org/10.5194/acp-20-1431-2020

Groß, S., Freudenthaler, V., Schepanski, K., Toledano, C., Schäfler, A., Ansmann, A., & Weinzierl, B. (2015). Optical properties of long-range transported Saharan dust over Barbados as measured by dual-wavelength depolarization Raman lidar measurements. *Atmospheric Chemistry and Physics*, 15(19), 11067–11080. https://doi.org/10.5194/acp-15-11067-2015

Groß, S., Tesche, M., Freudenthaler, V., Toledano, C., Wiegner, M., Ansmann, A., Althausen, D., & Seefeldner, M. (2011). Characterization of Saharan dust, marine aerosols and mixtures of biomass-burning aerosols and dust by means of multi-wavelength depolarization and Raman lidar measurements during SAMUM 2. *Tellus B: Chemical and Physical Meteorology*, 63(4), 706–724. https://doi.org/10.1111/j.1600-0889.2011.00556.x

Haarig, M., Ansmann, A., Engelmann, R., Baars, H., Toledano, C., Torres, B., Althausen, D., Radenz, M., & Wandinger, U. (2022). First triple-wavelength lidar observations of depolarization and extinction-to-backscatter ratios of Saharan dust. *Atmospheric Chemistry and Physics*, 22(1), 355–369. https://doi.org/10.5194/acp-22-355-2022

Haarig, M., Engelmann, R., Ansmann, A., Veselovskii, I., Whiteman, D. N., & Althausen, D. (2016). 1064 nm rotational Raman lidar for particle extinction and lidar-ratio profiling: cirrus case study. *Atmospheric Measurement Techniques*, 9(9), 4269–4278. https://doi.org/10.5194/amt-9-4269-2016

Haywood, J. M., Johnson, B. T., Osborne, S. R., Baran, A. J., Brooks, M., Milton, S. F., Mulcahy, J., Walters, D., Allan, R. P., Klaver, A., Formenti, P., Brindley, H. E., Christopher, S., & Gupta, P. (2011). Motivation, rationale and key results from the GERBILS Saharan

dust measurement campaign. *Quarterly Journal of the Royal Meteorological Society*, 137(658), 1106–1116. https://doi.org/10.1002/qj.797

Heese, B., Floutsi, A. A., Baars, H., Althausen, D., Hofer, J., Herzog, A., Mewes, S., Radenz, M., & Schechner, Y. Y. (2022). The vertical aerosol type distribution above Israel – 2 years of lidar observations at the coastal city of Haifa. *Atmospheric Chemistry and Physics*, 22(3), 1633–1648. https://doi.org/10.5194/acp-22-1633-2022

Hofer, J., Ansmann, A., Althausen, D., Engelmann, R., Baars, H., Abdullaev, S. F., & Makhmudov, A. N. (2020a). Long-term profiling of aerosol light extinction, particle mass, cloud condensation nuclei, and ice-nucleating particle concentration over Dushanbe, Tajikistan, in Central Asia. *Atmospheric Chemistry and Physics*, 20(8), 4695–4711. https://doi.org/10.5194/acp-20-4695-2020

Hofer, J., Ansmann, A., Althausen, D., Engelmann, R., Baars, H., Fomba, K. W., Wandinger, U., Abdullaev, S. F., & Makhmudov, A. N. (2020b). Optical properties of Central Asian aerosol relevant for spaceborne lidar applications and aerosol typing at 355 and 532 nm. *Atmospheric Chemistry and Physics*, 20(15), 9265–9280. https://doi.org/10.5194/acp-20-9265-2020

Hogan, R. J. & O'Connor, E. J. (2004). Facilitating cloud radar and lidar algorithms: the Cloudnet Instrument Synergy/Target Categorization product. *Cloudnet documentation*, 14. http://www.met.reading.ac.uk/~swrhgnrj/publications/categorization.pdf. last access: 12 June 2024

Holben, B., Eck, T., Slutsker, I., Tanré, D., Buis, J., Setzer, A., Vermote, E., Reagan, J., Kaufman, Y., Nakajima, T., Lavenu, F., Jankowiak, I., & Smirnov, A. (1998). AERONET—A Federated Instrument Network and Data Archive for Aerosol Characterization. *Remote Sensing of Environment*, 66(1), 1–16. https://doi.org/10.1016/S0034-4257(98)00031-5

HYSPLIT (2024). HYbrid Single-Particle Lagrangian Integrated Trajectory model, backward trajectory calculation tool, available at: https://www.ready.noaa.gov/index.php, last access: 12 June 2024.

Illingworth, A. J., Hogan, R. J., O'Connor, E., Bouniol, D., Brooks, M. E., Delanoé, J., Donovan, D. P., Eastment, J. D., Gaussiat, N., Goddard, J. W. F., Haeffelin, M., Baltink, H. K., Krasnov, O. A., Pelon, J., Piriou, J.-M., Protat, A., Russchenberg, H. W. J., Seifert, A., Tompkins, A. M., van Zadelhoff, G.-J., Vinit, F., Willén, U., Wilson, D. R., & Wrench, C. L. (2007). Cloudnet: Continuous Evaluation of Cloud Profiles in Seven Operational Models Using Ground-Based Observations. *Bulletin of the American Meteorological Society*, 88(6), 883 – 898. https://doi.org/10.1175/BAMS-88-6-883

Janhäll, S., Andreae, M. O., & Pöschl, U. (2010). Biomass burning aerosol emissions from vegetation fires: particle number and mass emission factors and size distributions. *Atmospheric Chemistry and Physics*, 10(3), 1427–1439. https://doi.org/10.5194/acp-10-1427-2010

Jimenez, C., Ansmann, A., Engelmann, R., Donovan, D., Malinka, A., Schmidt, J., Seifert, P., & Wandinger, U. (2020a). The dual-field-of-view polarization lidar technique: a new concept in monitoring aerosol effects in liquid-water clouds – theoretical framework. *Atmospheric Chemistry and Physics*, 20(23), 15247–15263. https://doi.org/10.5194/acp-20-15247-2020

Jimenez, C., Ansmann, A., Engelmann, R., Donovan, D., Malinka, A., Seifert, P., Wiesen, R., Radenz, M., Yin, Z., Bühl, J., Schmidt, J., Barja, B., & Wandinger, U. (2020b). The dual-field-of-view polarization lidar technique: a new concept in monitoring aerosol effects in

liquid-water clouds – case studies. *Atmospheric Chemistry and Physics*, 20(23), 15265–15284. https://doi.org/10.5194/acp-20-15265-2020

John, W. (2011). *Size distribution characteristics of aerosols*, volume 3, 41–54. John Wiley & Sons, Inc., Hoboken, NJ, USA, (3 ed.). https://doi.org/10.1002/9781118001684.ch4

Jäger, H. (2005). Long-term record of lidar observations of the stratospheric aerosol layer at Garmisch-Partenkirchen. *Journal of Geophysical Research: Atmospheres*, 110(D8). https://doi.org/10.1029/2004JD005506

Kaufman, Y. J. & Fraser, R. S. (1997). The Effect of Smoke Particles on Clouds and Climate Forcing. *Science*, 277(5332), 1636–1639. https://doi.org/10.1126/science.277.5332.1636

Kezoudi, M., Marenco, F., Papetta, A., Keleshis, C., Ryder, C., Kandler, K., Girdwood, J., Stopford, C., Wienhold, F., Gao, R.-S., Marinou, E., Amiridis, V., Močnik, G., Baars, H., , & Sciare, J. (2023). Profiling Saharan Airborne Dust with UAV-based in-situ Instrumentation during the ASKOS Experiment in Cape Verde, EGU General Assembly 2023, Vienna, Austria, 23–28 Apr 2023, EGU23-7249. Technical report. https://doi.org/10.5194/egusphere-egu23-17090

Klett, J. D. (1985). Lidar inversion with variable backscatter/extinction ratios. *Appl. Opt.*, 24(11), 1638–1643. https://doi.org/10.1364/AO.24.001638

Knippertz, P., Tesche, M., Heinold, B., Kandler, K., Toledano, C., & Esselborn, M. (2011). Dust mobilization and aerosol transport from West Africa to Cape Verde—a meteorological overview of SAMUM–2. *Tellus B: Chemical and Physical Meteorology*, 63(4), 430–447. https://doi.org/10.1111/j.1600-0889.2011.00544.x

Kosmopoulos, P., Kaskaoutis, D., Nastos, P., & Kambezidis, H. (2008). Seasonal variation of columnar aerosol optical properties over Athens, Greece, based on MODIS data. *Remote Sensing of Environment*, 112(5), 2354–2366. https://doi.org/10.1016/j.rse.2007.11.006

Laj, P., Myhre, C. L., Riffault, V., Amiridis, V., Fuchs, H., Eleftheriadis, K., Petäjä, T., Salameh, T., Kivekäs, N., Juurola, E., Saponaro, G., Philippin, S., Cornacchia, C., Arboledas, L. A., Baars, H., Claude, A., Mazière, M. D., Dils, B., Dufresne, M., Evangeliou, N., Favez, O., Fiebig, M., Haeffelin, M., Herrmann, H., Höhler, K., Illmann, N., Kreuter, A., Ludewig, E., Marinou, E., Möhler, O., Mona, L., Murberg, L. E., Nicolae, D., Novelli, A., O'Connor, E., Ohneiser, K., Altieri, R. M. P., Picquet-Varrault, B., van Pinxteren, D., Pospichal, B., Putaud, J.-P., Reimann, S., Siomos, N., Stachlewska, I., Tillmann, R., Voudouri, K. A., Wandinger, U., Wiedensohler, A., Apituley, A., Comerón, A., Gysel-Beer, M., Mihalopoulos, N., Nikolova, N., Pietruczuk, A., Sauvage, S., Sciare, J., Skov, H., Svendby, T., Swietlicki, E., Tonev, D., Vaughan, G., Zdimal, V., Baltensperger, U., Doussin, J.-F., Kulmala, M., Pappalardo, G., Sundet, S. S., & Vana, M. (2024). Aerosol, Clouds and Trace Gases Research Infrastructure – ACTRIS, the European research infrastructure supporting atmospheric science. *Bulletin of the American Meteorological Society*. https://doi.org/10.1175/BAMS-D-23-0064.1

Langmann, B. (2013). Volcanic Ash versus Mineral Dust: Atmospheric Processing and Environmental and Climate Impacts. *ISRN Atmospheric Sciences*, 2013, 1–17. https://doi.org/10.1155/2013/245076

Lebel, T., Parker, D. J., Flamant, C., Bourlès, B., Marticorena, B., Mougin, E., Peugeot, C., Diedhiou, A., Haywood, J. M., Ngamini, J. B., Polcher, J., Redelsperger, J.-L., & Thorncroft, C. D. (2010). The AMMA field campaigns: multiscale and multidisciplinary observations in

the West African region. *Quarterly Journal of the Royal Meteorological Society*, 136(S1), 8–33. https://doi.org/10.1002/qj.486

Lesins, G., Chylek, P., & Lohmann, U. (2002). A study of internal and external mixing scenarios and its effect on aerosol optical properties and direct radiative forcing. *Journal of Geophysical Research: Atmospheres*, 107(D10). https://doi.org/10.1029/2001JD000973

Liu, Y., Jia, R., Dai, T., Xie, Y., & Shi, G. (2014). A review of aerosol optical properties and radiative effects. *Journal of Meteorological Research*, 28(6), 1003–1028. https://doi.org/10.1007/s13351-014-4045-z

Mamouri, R.-E. & Ansmann, A. (2017). Potential of polarization/Raman lidar to separate fine dust, coarse dust, maritime, and anthropogenic aerosol profiles. *Atmospheric Measurement Techniques*, 10(9), 3403–3427. https://doi.org/10.5194/amt-10-3403-2017

Marinou, E., Paschou, P., Tsikoudi, I., Tsekeri, A., Daskalopoulou, V., Kouklaki, D., Siomos, N., Spanakis-Misirlis, V., Voudouri, K. A., Georgiou, T., Drakaki, E., Kampouri, A., Papachristopoulou, K., Mavropoulou, I., Mallios, S., Proestakis, E., Gkikas, A., Koutsoupi, I., Raptis, I. P., Kazadzis, S., Baars, H., Floutsi, A., Pirloaga, R., Nemuc, A., Marenco, F., Kezoudi, M., Papetta, A., Močnik, G., Díez, J. Y., Ryder, C. L., Ratcliffe, N., Kandler, K., Sudharaj, A., & Amiridis, V. (2023). An Overview of the ASKOS Campaign in Cabo Verde. *Environmental Sciences Proceedings*, 26(1). https://doi.org/10.3390/environsciproc2023026200

Martin, E., Bekki, S., Ninin, C., & Bindeman, I. (2014). Volcanic sulfate aerosol formation in the troposphere. *Journal of Geophysical Research: Atmospheres*, 119(22), 12,660–12,673. https://doi.org/10.1002/2014JD021915

Martins, B., Lourenço, L., & Monteiro, S. (2018). Natural Hazards in Sao Vicente (Cabo Verde). *Journal of Environmental Geography*, 11(1-2), 1–8. https://doi.org/10.2478/jengeo-2018-0001

McConnell, C. L., Highwood, E. J., Coe, H., Formenti, P., Anderson, B., Osborne, S., Nava, S., Desboeufs, K., Chen, G., & Harrison, M. A. J. (2008). Seasonal variations of the physical and optical characteristics of Saharan dust: Results from the Dust Outflow and Deposition to the Ocean (DODO) experiment. *Journal of Geophysical Research: Atmospheres*, 113(D14). https://doi.org/10.1029/2007JD009606

McCormick, R. A. & Ludwig, J. H. (1967). Climate Modification by Atmospheric Aerosols. *Science*, 156(3780), 1358–1359. https://doi.org/10.1126/science.156.3780.1358

Michailidis, K., Koukouli, M.-E., Balis, D., Veefkind, J. P., de Graaf, M., Mona, L., Papagianopoulos, N., Pappalardo, G., Tsikoudi, I., Amiridis, V., Marinou, E., Gialitaki, A., Mamouri, R.-E., Nisantzi, A., Bortoli, D., João Costa, M., Salgueiro, V., Papayannis, A., Mylonaki, M., Alados-Arboledas, L., Romano, S., Perrone, M. R., & Baars, H. (2023). Validation of the TROPOMI/S5P aerosol layer height using EARLINET lidars. *Atmospheric Chemistry and Physics*, 23(3), 1919–1940. https://doi.org/10.5194/acp-23-1919-2023

Miffre, A., David, G., Thomas, B., Rairoux, P., Fjaeraa, A., Kristiansen, N., & Stohl, A. (2012). Volcanic aerosol optical properties and phase partitioning behavior after long-range advection characterized by UV-Lidar measurements. *Atmospheric Environment*, 48, 76–84. https://doi.org/10.1016/j.atmosenv.2011.03.057

Müller, D., Ansmann, A., Mattis, I., Tesche, M., Wandinger, U., Althausen, D., & Pisani, G. (2007). Aerosol-type-dependent lidar ratios observed with Raman lidar. *Journal of Geophysical Research: Atmospheres*, 112(D16). https://doi.org/https://doi.org/10.1029/2006JD008292

Navas-Guzmán, F., Müller, D., Bravo-Aranda, J. A., Guerrero-Rascado, J. L., Granados-Muñoz, M. J., Pérez-Ramírez, D., Olmo, F. J., & Alados-Arboledas, L. (2013). Eruption of the Eyjafjallajökull Volcano in spring 2010: Multiwavelength Raman lidar measurements of sulphate particles in the lower troposphere. *Journal of Geophysical Research: Atmospheres*, 118(4), 1804–1813. https://doi.org/10.1002/jgrd.50116

Nicolae, D., Vasilescu, J., Talianu, C., Binietoglou, I., Nicolae, V., Andrei, S., & Antonescu, B. (2018). A neural network aerosol-typing algorithm based on lidar data. *Atmospheric Chemistry and Physics*, 18(19), 14511–14537. https://doi.org/10.5194/acp-18-14511-2018

Papagiannopoulos, N., Mona, L., Amodeo, A., D'Amico, G., Gumà Claramunt, P., Pappalardo, G., Alados-Arboledas, L., Guerrero-Rascado, J. L., Amiridis, V., Kokkalis, P., Apituley, A., Baars, H., Schwarz, A., Wandinger, U., Binietoglou, I., Nicolae, D., Bortoli, D., Comerón, A., Rodríguez-Gómez, A., Sicard, M., Papayannis, A., & Wiegner, M. (2018). An automatic observation-based aerosol typing method for EARLINET. *Atmospheric Chemistry and Physics*, 18(21), 15879–15901. https://doi.org/10.5194/acp-18-15879-2018

Pappalardo, G., Amodeo, A., Mona, L., Pandolfi, M., Pergola, N., & Cuomo, V. (2004). Raman lidar observations of aerosol emitted during the 2002 Etna eruption. *Geophysical Research Letters*, 31(5). https://doi.org/10.1029/2003GL019073

Paschou, P., Siomos, N., Tsekeri, A., Louridas, A., Georgoussis, G., Freudenthaler, V., Binietoglou, I., Tsaknakis, G., Tavernarakis, A., Evangelatos, C., von Bismarck, J., Kanitz, T., Meleti, C., Marinou, E., & Amiridis, V. (2022). The eVe reference polarisation lidar system for the calibration and validation of the Aeolus L2A product. *Atmospheric Measurement Techniques*, 15(7), 2299–2323. https://doi.org/10.5194/amt-15-2299-2022

Pattantyus, A. K., Businger, S., & Howell, S. G. (2018). Review of sulfur dioxide to sulfate aerosol chemistry at Kīlauea Volcano, Hawai'i. *Atmospheric Environment*, 185, 262–271. https://doi.org/10.1016/j.atmosenv.2018.04.055

Pearson, G., Davies, F., & Collier, C. (2009). An Analysis of the Performance of the UFAM Pulsed Doppler Lidar for Observing the Boundary Layer. *Journal of Atmospheric and Oceanic Technology*, 26(2), 240 – 250. https://doi.org/10.1175/2008JTECHA1128.1

Prospero, J. M., Ginoux, P., Torres, O., Nicholson, S. E., & Gill, T. E. (2002). Environmental characterization of global sources of atmospheric soil dust identified with the Nimbus 7 total ozone mapping spectrometer (TOMS) absorbing aerosol product. *Reviews of Geophysics*, 40(1), 2–1–2–31. https://doi.org/10.1029/2000RG000095

Rittmeister, F., Ansmann, A., Engelmann, R., Skupin, A., Baars, H., Kanitz, T., & Kinne, S. (2017). Profiling of Saharan dust from the Caribbean to western Africa – Part 1: Layering structures and optical properties from shipborne polarization/Raman lidar observations. *Atmospheric Chemistry and Physics*, 17(21), 12963–12983. https://doi.org/10.5194/acp-17-12963-2017

Robock, A. (2000). Volcanic eruptions and climate. *Reviews of Geophysics*, 38(2), 191–219. https://doi.org/10.1029/1998RG000054

Rocha-Lima, A., Martins, J. V., Remer, L. A., Todd, M., Marsham, J. H., Engelstaedter, S., Ryder, C. L., Cavazos-Guerra, C., Artaxo, P., Colarco, P., & Washington, R. (2018). A detailed characterization of the Saharan dust collected during the Fennec campaign in 2011: in situ ground-based and laboratory measurements. *Atmospheric Chemistry and Physics*, 18(2), 1023–1043. https://doi.org/10.5194/acp-18-1023-2018

Rodríguez, S. & López-Darias, J. (2021). Dust and tropical PM_x aerosols in Cape Verde: Sources, vertical distributions and stratified transport from North Africa. *Atmospheric Research*, 263, 105793. https://doi.org/10.1016/j.atmosres.2021.105793

Rolph, G., Stein, A., & Stunder, B. (2017). Real-time Environmental Applications and Display sYstem: READY. *Environmental Modelling & Software*, 95, 210–228. https://doi.org/10.1016/j.envsoft.2017.06.025

Ryder, C. L., Highwood, E. J., Rosenberg, P. D., Trembath, J., Brooke, J. K., Bart, M., Dean, A., Crosier, J., Dorsey, J., Brindley, H., Banks, J., Marsham, J. H., McQuaid, J. B., Sodemann, H., & Washington, R. (2013). Optical properties of Saharan dust aerosol and contribution from the coarse mode as measured during the Fennec 2011 aircraft campaign. *Atmospheric Chemistry and Physics*, 13(1), 303–325. https://doi.org/10.5194/acp-13-303-2013

Sassen, K. (2005). Polarization in Lidar. *Lidar: Range-Resolved Optical Remote Sensing of the Atmosphere*, volume 102 of *Springer Series in Optical Sciences*, 19–42. Springer New York, (1 ed.). https://doi.org/10.1007/0-387-25101-4_2

Sassen, K., Zhu, J., Webley, P., Dean, K., & Cobb, P. (2007). Volcanic ash plume identification using polarization lidar: Augustine eruption, Alaska. *Geophysical Research Letters*, 34(8). https://doi.org/10.1029/2006GL027237

Satheesh, S. & Krishna Moorthy, K. (2005). Radiative effects of natural aerosols: A review. *Atmospheric Environment*, 39(11), 2089–2110. https://doi.org/10.1016/j.atmosenv.2004.12.029

Seifert, P., Ansmann, A., Groß, S., Freudenthaler, V., Heinold, B., Hiebsch, A., Mattis, I., Schmidt, J., Schnell, F., Tesche, M., Wandinger, U., & Wiegner, M. (2011). Ice formation in ash-influenced clouds after the eruption of the Eyjafjallajökull volcano in April 2010. *Journal of Geophysical Research: Atmospheres*, 116(D20). https://doi.org/10.1029/2011JD015702

Stein, A. F., Draxler, R. R., Rolph, G. D., Stunder, B. J. B., Cohen, M. D., & Ngan, F. (2015). NOAA's HYSPLIT Atmospheric Transport and Dispersion Modeling System. *Bulletin of the American Meteorological Society*, 96(12), 2059–2077. https://doi.org/10.1175/BAMS-D-14-00110.1

Straume-Lindner, A. G., Parrinello, T., Von Bismarck, J., Bley, S., Wernham, D., Kanitz, T., Alvarez, E., Fischey, P., De Laurentis, M., Fehr, T., Ehlers, F., Duc Tran, V., Krisch, I., Reitebuch, O., & Renni, M. (2021). ESA'S Wind Mission Aeolus - Overview, Status and Outlook. *2021 IEEE International Geoscience and Remote Sensing Symposium IGARSS*, 755–758. https://doi.org/10.1109/IGARSS47720.2021.9554007

Stull, R. B. (2012). *An Introduction to Boundary Layer Meteorology*, volume 13. Springer Science & Business Media. https://doi.org/10.1007/978-94-009-3027-8

Tegen, I., Hollrig, P., Chin, M., Fung, I., Jacob, D., & Penner, J. (1997). Contribution of different aerosol species to the global aerosol extinction optical thickness: Estimates from

model results. *Journal of Geophysical Research: Atmospheres*, 102(D20), 23895–23915. https://doi.org/10.1029/97JD01864

Tesche, M. (2011). *Vertical profiling of aerosol optical properties with multiwavelength aerosol lidar during the Saharan Mineral Dust Experiments*. Leipzig University. https://nbn-resolving.org/urn:nbn:de:bsz:15-qucosa-71257. Last access: 12 June 2024

Tesche, M., Ansmann, A., Müller, D., Althausen, D., Engelmann, R., Freudenthaler, V., & Groß, S. (2009). Vertically resolved separation of dust and smoke over Cape Verde using multiwavelength Raman and polarization lidars during Saharan Mineral Dust Experiment 2008. *Journal of Geophysical Research: Atmospheres*, 114(D13). https://doi.org/10.1029/2009JD011862

Tesche, M., Gross, S., Ansmann, A., Mueller, D., Althausen, D., Freudenthaler, V., & Esselborn, M. (2011a). Profiling of Saharan dust and biomass-burning smoke with multiwavelength polarization Raman lidar at Cape Verde. *Tellus B: Chemical and Physical Meteorology*, 63(4), 649–676. https://doi.org/10.1111/j.1600-0889.2011.00548.x

Tesche, M., Müller, D., Gross, S., Ansmann, A., Althausen, D., Freudenthaler, V., Weinzierl, B., Veira, A., & Petzold, A. (2011b). Optical and microphysical properties of smoke over Cape Verde inferred from multiwavelength lidar measurements. *Tellus B: Chemical and Physical Meteorology*, 63(4), 677–694. https://doi.org/10.1111/j.1600-0889.2011.00549.x

Tsekeri, A., Amiridis, V., Louridas, A., Georgoussis, G., Freudenthaler, V., Metallinos, S., Doxastakis, G., Gasteiger, J., Siomos, N., Paschou, P., Georgiou, T., Tsaknakis, G., Evangelatos, C., & Binietoglou, I. (2021). Polarization lidar for detecting dust orientation: system design and calibration. *Atmospheric Measurement Techniques*, 14(12), 7453–7474. https://doi.org/10.5194/amt-14-7453-2021

Veselovskii, I., Hu, Q., Goloub, P., Podvin, T., Korenskiy, M., Derimian, Y., Legrand, M., & Castellanos, P. (2020). Variability in lidar-derived particle properties over West Africa due to changes in absorption: towards an understanding. *Atmospheric Chemistry and Physics*, 20(11), 6563–6581. https://doi.org/10.5194/acp-20-6563-2020

Wandinger, U. (2005). Introduction to Lidar. *Lidar: Range-Resolved Optical Remote Sensing of the Atmosphere*, volume 102 of *Springer Series in Optical Sciences*, 1–18. Springer New York, (1 ed.). https://doi.org/10.1007/0-387-25101-4_1

Weinzierl, B., Ansmann, A., Prospero, J. M., Althausen, D., Benker, N., Chouza, F., Dollner, M., Farrell, D., Fomba, W. K., Freudenthaler, V., Gasteiger, J., Groß, S., Haarig, M., Heinold, B., Kandler, K., Kristensen, T. B., Mayol-Bracero, O. L., Müller, T., Reitebuch, O., Sauer, D., Schäfler, A., Schepanski, K., Spanu, A., Tegen, I., Toledano, C., & Walser, A. (2017). The Saharan Aerosol Long-Range Transport and Aerosol–Cloud-Interaction Experiment: Overview and Selected Highlights. *Bulletin of the American Meteorological Society*, 98(7), 1427 – 1451. https://doi.org/10.1175/BAMS-D-15-00142.1

Whitby, K. T. (1978). The physical characteristics of sulfur aerosols. *Atmospheric Environment (1967)*, 12(1), 135–159. https://doi.org/10.1016/0004-6981(78)90196-8

WMO cloud definitions (2024). Cloud definitions of the World Meteorological Organization, available at https://cloudatlas.wmo.int/en/clouds-definitions.html, last access: 12 June 2024.

Xiong, X. & Barnes, W. (2006). An overview of MODIS radiometric calibration and characterization. *Advances in Atmospheric Sciences*, 23, 69–79. https://doi.org/10.1007/s00376-006-0008-3

Yin, Z. & Baars, H. (2021). *Pollynet/Pollynet_Processing_Chain: Version 3.0*. https://doi.org/10.5281/zenodo.5571289

Yus Díez, J., Bervida, M., Drinovec, L., Žibert, B., Lenarčič, M., Marinou, E., Paschou, P., Siomos, N., Baars, H., Engelmann, R., Skupin, A., Zenk, C., Fehr, T., & Močnik, G. (2023). Airborne In-situ Measurements during JATAC/CAVA-AW 2021/2022 campaigns - First Climate-Relevant Results, EGU General Assembly 2023, Vienna, Austria, 23–28 Apr 2023, EGU23-7249. Technical report. https://doi.org/10.5194/egusphere-egu23-15901

Selbstständigkeitserklärung

Hiermit bestätige ich, dass ich die vorliegende Masterarbeit selbstständig verfasst und keine anderen als die angegebenen Quellen und Hilfsmittel verwendet habe. Die Abbildungen ohne Quellenangabe wurden über die durch meinen Betreuer zur Verfügung gestellten Daten erstellt. Ich versichere, dass diese Arbeit noch nicht zur Erlangung eines Mastergrades an anderer Stelle vorgelegen hat.

Ort, Datum Unterschrift des Verfassers